USING NEAR INFRARED SPECTROSCOPY TO STUDY STATIC AND DYNAMIC HEMOGLOBIN CONTRAST ASSOCIATED WITH BREAST CANCER

A dissertation submitted by

Nishanth Krishnamurthy

In partial fulfillment of the requirements

for the degree of

Doctor of Philosophy

in

BIOMEDICAL ENGINEERING

TUFTS UNIVERSITY

May 2018

Advisor:

Sergio Fantini, Ph.D., Department of Biomedical Engineering, Tufts University

Committee Members:

Irene Georgakoudi, Ph.D., Department of Biomedical Engineering, Tufts University

Shuchin Aeron, Ph.D., Department of Electrical Engineering, Tufts University

Xavier Intes, Ph.D., Department of Biomedical Engineering, Rensselaer Polytechnic Institute

Abstract

Near-infrared spectroscopy (NIRS) of the breast exploits the inherent contrast of tumors due to increased hemoglobin absorption of light relative to healthy tissue. Optical imaging has been used to identify, characterize and monitor breast cancer non-invasively. This work first describes a new instrument for diffuse optical mammography in parallel plate geometry that operates over a broad spectral range of 600 – 1000 nm, features a scan time of 1 – 2 min, and allows for dynamic measurements at a selected region of interest. Furthermore, this new instrument is capable of depth discrimination of optical inhomogeneities embedded in the examined tissue by using multiple off-axis detection fibers.

Second, we report on an optical mammography study on eight patients with breast cancer who underwent neoadjuvant chemotherapy to identify biomarkers that indicate the patient's degree of response. We found that both the total hemoglobin concentration and hemoglobin oxygen saturation (SO2) decreased by a greater amount in responders than in non-responders during therapy. This result applied to both cancerous and healthy breasts, but the discrimination of responders and non-responders was more significant with SO2 measurements in the cancerous breast. We developed a cumulative response index that achieved 100% sensitivity and 100% specificity in characterizing response half way through chemotherapy.

Lastly, induced arterial blood pressure oscillations result in peripheral hemodynamic oscillations that provide information about local changes in blood flow and blood volume. We first report on a comparison of two protocols to induce cerebral hemodynamic oscillations, paced breathing and cyclic inflation of pneumatic thigh-cuffs.

These two protocols induce systemic mean arterial pressure oscillations of similar magnitude but show varied response in the dynamics of cerebral oxy- and deoxy-hemoglobin concentrations. This variability may be due to altered physiological states under the paced breathing protocol, or anatomical differences between subjects. We then report on an initial attempt at inducing hemodynamic oscillations using pneumatic thigh-cuffs in patients undergoing neoadjuvant chemotherapy. We found that in one patient with complete data, we were unable to distinguish changes in the hemodynamics between healthy and cancerous breasts. Ultimately, a more robust measurement protocol is needed to ensure that oscillations driven by mean arterial pressure are reliably induced in the breast. To advance NIRS into clinical practice, larger studies, with standardized equipment need to be performed to establish its value for individual patients.

Acknowledgments

Throughout my work as a PhD student, I have had many successes and failures, and as I fought through them I learned to understand which of my choices were the correct ones. Choosing to work with Sergio for the last 6 years has easily been the most rewarding and inspiring experience of my career. Sergio teaches his students a scientific framework that is useful for all aspects of life. Following Sergio's example, I feel that I have improved my work ethic, efficiency and passion for the work I do every day. Outside of discussing Bill Belichick's latest coaching decision, or the merits of using en-dashes, em-dashes, and hyphens appropriately—I have learned an incredible amount working in the DOIT lab from 2012 – 2018.

Working in Sergio's lab also has the advantage of attracting some of the smartest students, post-docs and researchers whom I have had the pleasure of working with. Kristen Tgavalekos, Pami Anderson, Angelo Sassaroli, Thao Pham, Giles Blaney, Jana Kainerstorfer and Kosar Khaksari have been great friends and colleagues, and our discussions in and out of group meeting have made me a better scientist. Getting to know them and learning alongside them has been an amazing experience. I would like to especially thank Angelo Sassaroli, for his timely guidance and patience in explaining with great detail the answer to any question I felt like asking. Angelo has been invaluable as a mentor during my PhD. I would also like to give credit to Pami Anderson who started the optical mammography project. She performed all the data collection and provided an initial analysis of all the data presented in Chapter 3 here, in her dissertation. I not only had the good fortune of being able to pick up her work and develop new analyses of her data to publish it, but also learned an incredible amount working alongside her on various projects.

I would like to thank my friends for their honest advice, ample support, and encouragement. Many of my friends may not know what I actually did when I went to "work" but were nonetheless always ready to provide relief when I needed it most. To undoubtedly my fiercest supporter and most inspiring friend, Deepti, you have always pushed me to become a better person, scientist, and citizen. Your unconditional faith in my capabilities, as well as your passion for public service has made me realize what I can accomplish. As I finish my graduate degree, I am so excited to see how you choose to change the world with yours—I can only hope that I will be as useful to you as you were to me.

Lastly, I am nothing without my family. To my brother, the first Dr. Krishnamurthy, I have always competed with you and without that competition I would not be the person I am today. Being a younger brother, I have the immense advantage of always being able to follow in your footsteps and am so fortunate that you have not led me in the wrong direction (yet). To my parents, I am eternally indebted to you for the many opportunities I have been afforded. Amma, from when I was a small child you forced me to learn my multiplication tables instead of watching TV, to read books rather than play video games, while I never understood the value of painfully wasting play time then, it has not stopped paying dividends since.

I would like to dedicate my dissertation to my father. Appa, you gave up so many opportunities to relax and enjoy everything you earned so you could pass it all on to Bharath and I. When I was applying to PhD programs, your sacrifices finally took their toll. I'm so happy I got to tell you I was accepted to Tufts just minutes before you went in for heart surgery, and now I'm so proud of how you have bounced back. I've watched you go from

walking a couple miles to comfortably running almost 5 miles a day over the last 6 years, and somehow even when you are not directly supporting us, you always find ways to inspire us to do more and be better at everything.

Table of Contents

List of Tables

List of Figures

Motivation

Breast cancer is the most common cancer in women and the second leading cause of death in many countries. Early diagnosis of breast cancer is critical to favorable prognosis. As such, identifying diagnostic methods that have high sensitivity and specificity are crucial for advancing the treatment of this disease. X-ray mammography is the clinical standard for breast cancer screening despite tissue density providing poor sensitivity to breast cancer in younger women and despite the requirement for ionizing radiation which may have carcinogenic effects affording a limited measurement frequency. Furthermore, false-positive rates in X-ray mammograms can be as high as 50% requiring additional testing at a financial cost to health care institutions and an emotional cost to the patients[1,2]. Optical measurements using near-infrared light have been proposed as a cost-effective, non-ionizing, and non-invasive imaging solution to detect breast cancer over the last 20 years.[3] Optically, breast cancer measurements have typically focused on the detection of hemoglobin content in tissue. It has been consistently reported that breast cancer is associated with locally elevated levels of hemoglobin in tissue.[4–7]

Achieving the full clinical potential of near infrared spectroscopy for breast cancer detection hinges on the identification of information content from optical measurements for effective cancer detection and/or monitoring of response to therapy. However, the limited specificity of hemoglobin and the oxygen saturation of hemoglobin in breast cancer alone has prevented their adoption as robust diagnostic parameters thus far.[8,9] Accordingly, the goal of this work is to maximize the information content achievable in a non-invasive optical measurement of the breast, and to develop techniques that can extract physiologically relevant parameters that serve as biomarkers for breast cancer monitoring.

Dissertation outline

The work in this dissertation describes various approaches to applying near-infrared spectroscopy. The first chapter discusses light-tissue interactions and goes on to introduce existing clinical techniques being used to monitor breast cancer and the information gap that near-infrared spectroscopy (NIRS) can fill. Chapter 2 outlines the development and testing of an optical mammography instrument that can collect five-dimensional (three spatial, temporal, and spectral) information. Chapter 3 describes the use of static optical mammograms taken during each chemotherapy session to monitor the response of breast cancer patients. While static optical mammograms can provide information about spatial changes over time, they lack the functional information to better understand the source of these changes. In Chapter 4, we discuss the variability associated with two protocols for inducing systemic hemodynamic oscillations and measure those oscillations in the brain. In previous studies our group has shown that induced oscillations measured in the healthy breast do not provide the hemodynamic signature of interest, namely a phase difference between oxy- and deoxy-hemoglobin. As such, we chose to first understand the variability in this phase relationship in healthy subjects in the brain, where we have previously reported the importance of this measurement. We hypothesized that due to the altered vasculature function in breast cancer we could identify differences in the hemodynamics between healthy and cancerous breast, that resemble the phase relationship we see in the brain which is indicative of changes in blood flow. In Chapter 5 the initial measurements of hemodynamic oscillations in the breast on patients undergoing neoadjuvant chemotherapy are described. Finally, this dissertation concludes with a summary of the findings reported and a description of potential future directions based on this work.

Chapter 1: Background on near infrared spectroscopy and breast cancer imaging

1.1. Light-tissue interactions

Near-infrared spectroscopy (NIRS) when applied to biological tissues, is an optical technique that utilizes safe levels of radiation in the wavelength region 650 – 1000 nm. Near-infrared light experiences two physical processes when interacting with biological tissues. The first one is absorption, defined by the absorption coefficient (μ_a with units of cm^{-1}) which describes the inverse mean pathlength of photons before they are absorbed by chromophores in the tissue and translated into heat energy. Using near-infrared light allows for a larger penetration depth for optical techniques due to the relatively low absorption for this wavelength range. The absorption coefficient is defined by the sum of the individual absorption from each chromophore that exists in the optical path and ranges from $0.01 – 0.15\ cm^{-1}$ for healthy biological tissues (Figure 1.1). The major chromophores in the near-infrared window include oxy- and deoxy-hemoglobin, and in smaller proportion water and lipids. This makes NIRS particularly sensitive to hemoglobin concentrations and hemodynamics.

The second process experienced by photons inside tissues is scattering, which is defined by the reduced scattering coefficient (μ_s'), describing the inverse mean pathlength of photons before they lose information regarding their initial direction. The reduced scattering coefficient is typically one to two orders of magnitude greater than the absorption coefficient (typically between 2 and 20 cm^{-1}), such that light scattering events dominate in most biological tissues. The consequence of the much larger reduced scattering characteristics of biological tissues is that the near-infrared light injected into the tissue

rapidly becomes a diffuse photon density wave, which then traverses the tissue. This poses an intrinsic limitation to the spatial resolution (~5 mm) of NIRS for optical imaging purposes.

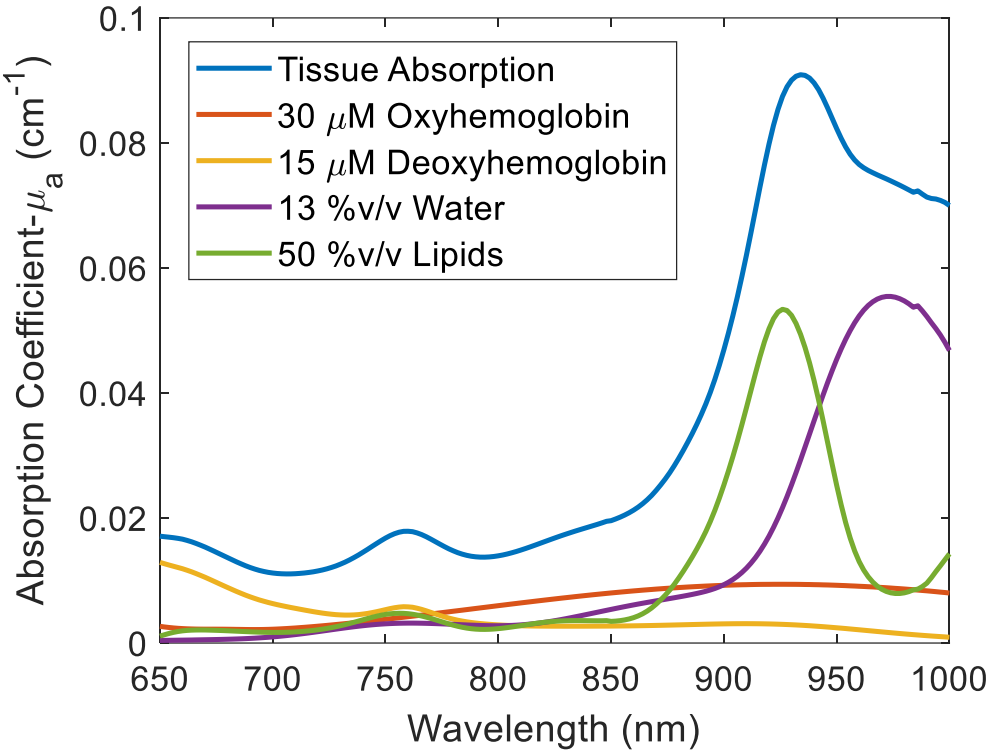

Figure 1.1: Absorption contributions from each chromophore based on typical concentrations in the human breast. Total tissue absorption is based on the sum of the four individual contributions.

Absolute hemoglobin concentrations (as well as water and lipids concentrations) can be directly derived from the absorption spectra seen in Figure 1.1. However, the strong diffusion of light in tissue and the effects of both optical coefficients (*i.e.* μ_a and μ_s') on light propagation requires a light transport model to separate them uniquely. Furthermore, different geometries, tissue layers, or arrangements of source and detector affect the accurate recovery of these optical coefficients. A more comprehensive review of the types of instruments capable of recovering optical measurements of hemoglobin, water, and lipid concentrations is presented in section 2.1.

1.2. Breast cancer anatomy, and treatment

Breast tissue extends from the collarbone, to lower ribs, sternum (breastbone) and armpit. The breast is primarily comprised of fatty and fibroglandular tissue. Each breast contains 15-20 glands called lobes, where milk is produced in women who are breastfeeding. These lobes are connected to the nipple by 6-8 tubes called ducts which carry milk to the nipple. The breast and armpit also contain lymph nodes and vessels carrying lymph fluid and white blood cells, which are part of the immune system. Much of the rest of the breast is fatty tissue.

In the case of breast cancer, there are two types: lobular carcinoma *in situ* and ductal carcinoma *in situ*. Typically *in situ* cancers are treated with a lumpectomy or mastectomy followed by radiation therapy, and generally have favorable prognoses when diagnosed early. However, the majority of breast cancer diagnoses are invasive ductal carcinoma, followed by invasive lobular carcinoma when the cancer has spread beyond the ducts or lobes respectively. Inflammatory breast cancer, which is rarer, is diagnosed when cancer cells have been identified in the lymph vessels in the skin. When breast cancer is identified, typically from X-ray images, biopsies are taken to identify the type and grade of the cancer. Typically, lymph nodes are also imaged and a biopsy may be performed to see if cancer cells have spread to the nodes. When cancer is found in the lymph nodes, chemotherapy treatment is often recommended, followed by surgery and radiation therapy as well.

1.3. Imaging and diagnosis of breast cancer

1.3.1. X-ray mammography

The current clinical methods for breast cancer screening are palpation and x-ray mammography performed on asymptomatic population. Although palpation can give a rough estimate about the existence of any suspicious masses in the breast, it is far less commonly used than x-ray

mammography. Women with average risk of breast cancer are recommended to have annual screening after age 45.[10] X-ray mammograms produce images by transmitting low dose (~0.7 mSv) ionizing radiation through compressed breast tissue. X-rays are sensitive to variations in tissue density, where dense fibroglandular tissue is more attenuating compared to adipose tissue. Full field digital mammography has recently replaced traditional film-screen mammography due to the flexibility allowed through digital manipulation of X-rays to enhance features of suspicious lesions. X-ray mammography is of greatest advantage due to its ability to detect micro-calcifications which often are the earliest signs of malignancy. However, mammograms have high false-positive rates and limited sensitivity in patients with dense breasts, typically younger women.[10] If X-rays fail to provide a conclusive diagnosis, ultrasound or MRI images may be required.

1.3.2. Ultrasound

Breast ultrasound is invaluable in characterizing masses as cystic or solid. It is the only modality employed during lactation and pregnancy and in painful conditions where mammographic compression is not possible. It is also valuable for evaluation of the post surgical and irradiated breast. Ultrasound uses sound waves (7-13 MHz) to estimate the location and shape of masses by identifying the refractive index mismatch at the interface of the lesions. Ultrasound does not use ionizing radiation and is associated with little discomfort when compared to X-ray mammography. It has, in recent years, been used as an adjunct technique to X-ray mammography to improve sensitivity especially in patients with radiographically dense breasts.[11] However, ultrasound is not sensitive to small microcalcifications that are early indicators of breast cancer making it unsuitable as a screening or diagnostic tool.

1.3.3. Magnetic resonance imaging

Magnetic resonance imaging (MRI) scans are typically performed after an early stage diagnosis (stage I or II) of breast cancer to identify any additional foci of cancer and to assist in surgery.[10] Breast MRI has had a growing popularity for the past decade due to its high sensitivities to tissue abnormality due to its high spatial resolution to reveal the detailed structures of the interior of the breast.[12] It is primarily performed to probe the areas which do not offer clear images in mammography or ultrasonography. It is typically conducted only when no confident diagnostics is reached after mammography or ultrasound, or to evaluate the efficacy of the tumor removal surgery or chemotherapy treatment. MRI provides morphological and kinetic information about suspicious breast lesions. Appropriate staging of the disease for patients diagnosed with breast cancer relies on knowledge of the size of the tumor, which can be obtained from an MRI also. However, MRIs are significantly more expensive limiting their practicality as a screening tool.

1.3.4. Optical imaging of breast cancer

Cutler[13] was the first to show how transillumination of the female breast using visible light could help defining the position of a lesion, particularly in cases of the bleeding nipple. He pointed out the limitations of the technique notably the inability of the method at that stage to distinguish benign from malignant disease. The development of mammary radiography soon after and its ability to distinguish microcalcifications appears to have limited the development of diaphanography as a means of diagnosing breast cancer at the time. By the 1970s, concern surrounding the effects of repeated X-ray exposure, as well as the minimal specificity of X-ray mammography for patients with dense breasts led to renewed interest in diaphanography since it used non-ionizing radiation.[14] A number of researchers showed promising results towards the capability of light-scanning

mammography to detect breast cancer.[15–17] Although they were able to identify regions of contrast due to the increased optical absorption of cancerous tissue, light-scanning was deemed inferior to X-ray mammography in terms of its sensitivity to breast cancer.[18,19] In the 1990s, analytical models to describe near-infrared light propagation in tissues,[20–22] combined with sophisticated instrumentation for data collection and rigorous methods of data analysis, led to the development of more advanced near-infrared spectroscopy (NIRS) and diffuse optical tomography (DOT) systems aimed at detecting, diagnosing, and monitoring breast cancer.[8,23–34]

Near-infrared spectroscopy and DOT of the breast take advantage of the intrinsic optical contrast provided by the tissue concentrations of oxyhemoglobin, deoxyhemoglobin, water, and lipids ([HbO_2], [Hb], [water], and [lipids], respectively). The ratio of oxyhemoglobin to total hemoglobin concentration ([HbT]) yields the oxygen saturation of hemoglobin, which is a measure of the balance of oxygen supply and oxygen utilization in tissue. Localized changes in the concentration and oxygen saturation of hemoglobin in breast tissue have been linked to angiogenic developments and perturbations to the tissue metabolic rate associated with the development of breast cancer.[9,24,25,27,29,31,35,36] Additionally, localized changes in [water] and [lipids] can be indicative of structural modifications in the tissue associated with changes in cellularity and fibrous tissue content. These changes have also been shown to be indicative of tumor development.[8,9,25,27,29,35,36] Optical methods of breast cancer evaluation show promise due to the opportunity to evaluate both structural and functional changes associated with breast cancer simultaneously.

Chapter 2: Imaging system design

2.1. Background

2.1.1. Differences between time-domain, frequency-domain, and continuous-wave systems.

Near-infrared spectroscopy and DOT systems can be classified as continuous-wave (CW)[8,23,24,29], time-domain (TD)[25,35], and frequency domain (FD)[23,27] based on the temporal characteristics of the light source and optical detection systems. Absolute measurements of [HbO_2], [Hb], [water], and [lipids] are dependent on the accurate recovery of the tissue absorption coefficient (μ_a), which in turn requires the determination of the tissue reduced scattering coefficient (μ_s'). Time-domain and FD systems have the capability to measure μ_a and μ_s' simultaneously, but usually feature limited spectral sampling (<10 wavelengths). Theoretically, to measure the concentrations of four chromophores ([HbO_2], [Hb], [water], and [lipids]), one only needs measurements at four wavelengths that feature sets of extinction coefficients of the four chromophores that are linearly independent. However, because of random and systematic experimental errors, accurate measurements of μ_a and μ_s' benefit from greater spectral sampling both in terms of the number of wavelengths and the wavelength range. In this regard, TD systems may take advantage of super-continuum lasers[30,31] to achieve broadband spectral collection. However, TD systems often require longer acquisition times to provide accurate measurements of the temporal point spread function, and each wavelength requires an individual photon counting system increasing the complexity and cost of achieving high spectral sampling rates.

Systems based on CW light inherently have less information content than TD or FD systems and are unable to measure the absorption and scattering properties of tissue separately.[37] However, CW systems generally provide higher spectral sampling (>100 wavelengths over the full spectral range of interest) with a standard spectrograph and CCD camera system. Spectral sampling at wavelengths longer than 900 nm can provide greater sensitivity to [lipids] and [water] as a result of their absorption peaks at 930 and 970 nm, respectively.[31] The inability of CW systems to independently measure the reduced scattering coefficient requires some kind of assumption about the scattering properties of breast tissue. For example, one may perform FD measurements at a set of wavelengths and obtain a reduced scattering spectrum by interpolation,[29] or a scattering spectrum may be assumed on the basis of measurements reported in the literature for breast tissue.[8]

2.1.2. Recovering tomographic information and temporal dynamics

The spatial information of NIRS and DOT images yields the distribution of tissue chromophores within breast tissue. Such spatial distributions relate the location of breast lesions to associated perturbations to the concentration and oxygen saturation of hemoglobin, or to perturbations in water and lipid content. Full 3D spatial information is desirable to accurately identify the location and extent of breast lesions. Approaches to 3D imaging can be grouped into tomographic reconstructions[32,38] and depth discrimination methods in planar scanning systems.[23,31,35] Diffuse optical tomography systems use a number of source-detector pairs (typically 32 – 64 pairs)[24,33] placed around the breast or in a parallel-plate geometry[32,39] to solve the inverse imaging problem in 3D.[22] While DOT systems offer full 3D spatial reconstructions, the task is complex, has high demands on

data collection and computational routines, and suffers from the ill-posed nature of the inverse imaging problem in the diffusion regime. Planar scanning systems may use a single source-detector pair that is scanned to create a 2D projection image of the breast in a transmission geometry,[8,31,35] or may employ parallel planar detection by a lens-coupled CCD camera.[32] Scanning systems typically provide a fine spatial sampling (>1 cm^{-1}) to identify detailed superficial structures, such as blood vessels, within the breast.[23,35,40] Depth discrimination can be obtained from multiple projections realized by offset detectors that are not collinear with the optical illumination.[41–43] Compared to a full tomographic reconstruction, this approach to depth discrimination is more straightforward and potentially robust. However, it is not capable of resolving multiple structures in depth, and it provides a coarser depth assessment than tomographic approaches based on a complete optical data set around the breast.

Temporal information, as collected with dynamic optical measurements of breast tissue, can broaden the scope of optical mammography to include intrinsic hemodynamic features and hemodynamic responses to external stimuli or perturbations. Recently, research groups have been exploring the possibility that induced changes of [HbO_2] and [Hb] within the breast may be used to discriminate healthy and cancerous tissue. Different methods of dynamic breast compression[34,44] or regulated respiration[33,45,46] have been shown to cause optically measurable hemodynamic fluctuations in breast tissue. Manual compression of the breast induces an increase in the interstitial fluid pressure which can cause a decrease in blood content of up to 20% in healthy subjects.[44] Similarly, regulating respiration by either paced breathing or breath-holding induces systemic changes in blood pressure that result in changes in blood content that can range from 5-10% in healthy

subjects.[33,46] It has been reported that differences in the measured magnitude of this change and in the associated washout rate are indicative of differences in the vasculature of healthy and cancerous tissue.[33,44,46,47] To measure these changes, systems with acquisition rates on the order of 1 Hz are required since the relevant frequency band of tissue hemodynamics is generally limited to frequencies below the heart rate (~1 Hz). Since the characteristic times of induced hemodynamics may be on the order of a few seconds, a sampling frequency of $0.5 - 1$ Hz is sufficient in most cases. Hand-held probes[48,49] generally provide the highest temporal resolution (>10 Hz) and have the flexibility to measure different locations on the breast. However, concurrent measurements, which are required to make comparative analyses of multiple locations on the breast, require multiple probes with unknown calibration factors related to individual probe-tissue coupling and pressure. Depending on the number of source-detector pairs, tomographic systems are limited in their temporal resolution (<1 Hz) but benefit in being able to provide detailed spatial maps of optical properties over time. However, recently, Flexman *et al.* have developed a tomographic system capable of 3D reconstructions at sampling frequencies up to 2 Hz depending on the number of wavelengths and source-detector pairs used.

2.1.3. Main features of the instrument presented here

We have previously reported an optical mammography instrument based on a CW, planar tandem scan of a collinear source-detector pair (wavelength range: $650 - 850$ nm) to generate 2D snapshots of chromophore maps in breast cancer patients.[8] We report here the development of a new CW breast scanning system (wavelength range $650 - 1000$ nm) using one source and four detector optical fibers (one collinear and three off-axis with respect to the source fiber) with high spectral (~2.5 nm^{-1}), spatial (25 cm^{-2}), and temporal

(~10 – 20 Hz) sampling rates. With respect to our previous instrument, the extended spectral range allows for a higher sensitivity to [water] and [lipids], the off-axis detection scheme allows for depth sensitivity and 3D imaging, and the temporal resolution (at a stationary location) allows for hemodynamic measurements. Here, we demonstrate the 3D capabilities of this new instrument by imaging a tissue-like optical phantom containing absorbing structures, and the dynamic measurement capabilities by assessing physiological hemodynamics in healthy volunteers. We also discuss the relevance of implementing these advanced spectral, spatial, and temporal methods in a consolidated system, and how it can enhance the detection and monitoring of breast cancer in a clinical setting.

2.2. Methods

2.2.1. System for scanning optical mammography

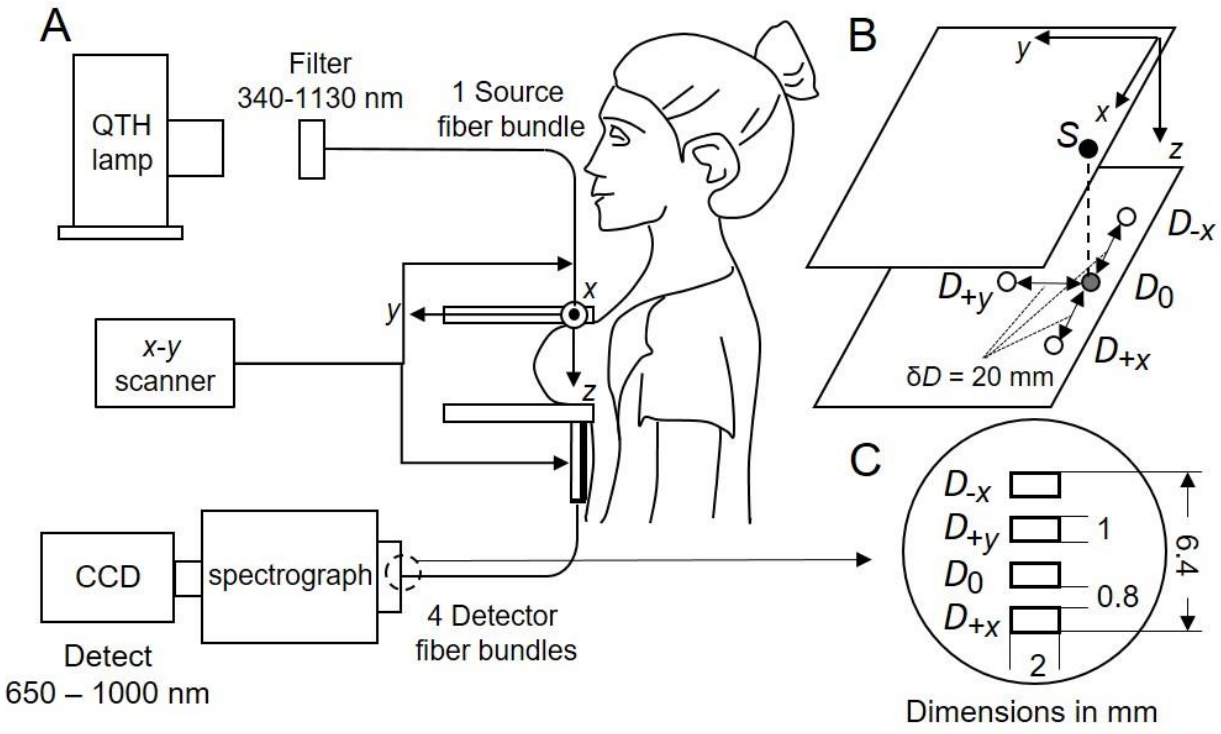

Figure 2.1: A) Block diagram of the optical mammography instrument for spectral imaging of the human breast. The emission of a quartz-tungsten-halogen (QTH) lamp is spectrally

filtered from 340 – 1130 nm and light is delivered to the breast through an optical fiber for illumination. B) A four-legged detector fiber is arranged in a transmission geometry with the fibers oriented in the *x*-*y* plane. The offset between each fiber and D_0 was set at δD = 20 mm. C) The 2×1 mm^2 rectangular arrangement of each detection fiber bundle into a single ferrule spanning 6.4 mm in height. The spectrograph spatially resolves light of different wavelengths from each fiber simultaneously onto a 26.8×8 mm^2 charge-coupled device (CCD) chip which acquires four spectra (wavelength range: 650 – 1000 nm), corresponding to the four detection fibers, at each source position.

The emission of a quartz-tungsten-halogen (QTH) lamp (Model No. 66635, Newport Instruments, Irvine, CA) was band pass filtered by a spectral filter (Model YSC1100, Asahi Spectra USA, Torrance, CA) to a 340 – 1130 nm spectral bandwidth. The illumination light was delivered to the breast or optical phantom using a 2.5 mm diameter optical fiber bundle with a maximum illumination power exiting the fiber of 350 mW. The source-fiber was mounted onto a 2D scanning slide controlled by stepper motors (Model XN10-0180-E02-71, Velmex, Bloomfield, NY). The end of the fiber was separated from the breast by a 6.5 mm thick, clear, polycarbonate plate. Although light-channeling is a concern with illumination through clear polycarbonate plates, in a transmission geometry the effects of light channeling on our measurements are minimal due to the large source-detector distance and strong attenuation of light in tissue. The source fiber numerical aperture (NA) was 0.55, which resulted in a spot diameter on the breast of about 11 mm, and a maximum radiant exposure of ~250 mJ/cm^2. With a 16 mm/s scan speed, the maximum illumination time at any given location on the breast (pixel resident time) was ~690 ms, for which the maximum permissible exposure of skin to near-infrared light is ~1 J/cm^2 while the fiber was scanned (ANSI Z136.1-2007). Typically, measurements were done using an illumination power of ~100 mW (yielding a radiant intensity at the tissue of ~75 mJ/cm^2). However, for subjects with larger breasts (requiring >6 cm plate separation) the ability to increase the power level allowed us to maintain a suitable signal to noise ratio

(SNR). For static measurements (no scanning), where the pixel resident time of the fiber could be as long as 10 min, the maximum permissible exposure was limited to a radiant intensity of 0.2 W/cm^2 (ANSI Z136.1-2007). For these measurements, we had to ensure that the power exiting the fiber was less than 190 mW. In cases where it was desirable to increase the SNR, we had the capability to increase the integration time since our temporal sampling rate (~10 – 20 Hz) was greater than the required temporal resolution of 1 Hz for physiological hemodynamics.

The breast or phantom was placed between the two polycarbonate plates attached to the scanning slide housing (Figure 2.1A). The transmitted light was collected by four 2.5 mm diameter detector optical fibers with an NA of 0.22 which were arranged in a 'T' pattern (Figure 2.1B), and mounted onto another 2D scanning slide. The smaller acceptance angle of the detector fibers provided a smaller spot diameter at the breast (~3 mm) allowing for finer spatial sampling in our images. The 'T' pattern for the detectors maximized the size of the imaged area for which depth information was collected. The source and detector fibers were scanned in tandem such that the central detector fiber (D_0) remains collinear with the source fiber during the scan. The three off-axis detector fibers were offset in the positive and negative x-direction (D_{+x} and D_{-x} respectively) and in the positive y-direction (D_{+y}). The offset distances of D_{+x} and D_{-x} in the x-direction (δD_{+x} and δD_{-x} respectively) and D_{+y} in the y-direction (δD_{+y}) were set to the same value δD = 20 mm with respect to the location of D_0 (the collinear detector). To obtain depth information for structures oriented in multiple directions, we have previously shown that two orthogonally offset detectors, are sufficient.[40] The arrangement of the detector fibers with two offset detector locations along the x-direction ensured that one of the off-axis fibers offset in the

x-direction would remain within the *x*-*y* projection of the imaged tissue, thus providing depth information at the edges of the breast. Ideally, a fifth offset detector fiber in the negative *y*-direction would maximize the depth information in both spatial dimensions. However, to maximize the imaged area, we omitted this fiber to allow D_0 to scan as close to the chest wall as possible. The four detector fibers were joined into a single ferrule with four 2×1 mm^2 rectangular areas corresponding to each of the detector fibers (Figure 2.1C). The four rectangular fiber ends were vertically distributed over 6.4 mm on the end of the ferrule with 0.8 mm spacing on either side of each fiber which resulted in a total vertical dimension of 8 mm. These 8 mm corresponded to the height of the charge-coupled device (CCD) chip within the camera (Model Pixis400, Princeton Instruments, Princeton, NJ). The ferrule was placed at the entrance slit of the spectrograph (Model SP-150, Princeton Instruments, Princeton, NJ) which contains an internal shutter with an actuation time of 8 ms. The light from the four fibers was spectrally dispersed by a 300 G/mm grating blazed at 830 nm resulting in a dispersion of 18.7 nm/mm.

The cooled, 16-bit CCD camera was attached at the exit port of the spectrograph and acquired four spectra, corresponding to the four detection fibers, simultaneously. The sensitivity of the CCD was 1 electron per analog-to-digital (A/D) count with a 2 MHz A/D conversion rate. The CCD was made up of a 1340×400 pixel^2 array with 20×20 μm^2 pixels (resulting in a 26.2×8 mm CCD chip). The lateral dimension of the CCD was used for spectral sampling whereas the longitudinal dimension was used for the spatial sampling of the four detection fibers. The resulting spectral sampling rate was ~2.5 nm^{-1}, and the measured spectral range was 580 – 1081 nm based on a center wavelength of 830 nm. The optical signal below 650 nm is strongly attenuated by the absorption of hemoglobin in

breast tissue, and the signal at wavelengths longer than 1000 nm was restricted by the lower quantum efficiency (<30%) of the CCD. Consequently, only the wavelength range 650 – 1000 nm was used in this work. The spectral resolution of the system was limited by the slit width; to achieve the highest signal-to-noise ratio we maximized the detected intensity by using a slit width of 2 mm, which resulted in a spectral resolution of ~50 nm. The broad spectral features of hemoglobin, water, and lipids limit the requirement for high spectral resolution in NIRS of the breast. Considering the limited requirement for spectral resolution, the spectral sampling provided by this camera was more than necessary. However, it was chosen because it provided a quantum efficiency above 90% for light in the wavelength range 650-900 nm and above 30% up to 1000 nm which was necessary for robust measurements of [water] and [lipids]. Additionally, we found that laterally binning the CCD chip only marginally improved our acquisition rate and SNR at the cost of reducing our dynamic range. Consequently, we maintained the full spectral sampling rate of the CCD chip in our data collection scheme.

Control of the stepper motors and CCD, as well as data collection, was done with LabVIEW (National Instruments, Austin, TX). Scanning started close to the chest wall moving continuously in the +*x*-direction at a speed of 16 mm/s. The scanner was stopped automatically by the software at the edge of the breast when the tissue thickness was reduced by approximately 20 mm and the transmitted intensity exceeded the dynamic range of our CCD and saturated it. At that point, the scanner moved 2 mm in the +*y*-direction and started scanning in the −*x*-direction. With an exposure time (including the 8 ms shutter actuation) of 100 ms and a readout rate of 28 ms, spectra were acquired every 128 ms resulting in a pixel size of ~2 mm along the *x*-direction. When the length of a

scanned line was less than 10 mm (5 pixels) the data acquisition was stopped and the fibers returned to their starting position. The typical scanning time for a 100 mm × 100 mm area was about 6 min. Our method of raster-scanning optical fiber bundles to create spectral images of the transmitted intensity requires a balance of scan speed, spatial sampling rate, and signal to noise ratio (SNR). Increasing the scan speed, while maintaining the spatial sampling rate along the scanning direction, requires a reduction of the exposure time per pixel. This would result in an inherently lower signal and SNR. A spatial map of intensity at 830 nm was updated during the scan for real-time display in the graphical user interface. Data collection on phantoms took place in a dark room to prevent leakage of room light into the optical detector, whereas in the case of breast measurements we found that the subject's body provided some shielding of room light to allow for dim illumination in the room.

2.2.2. Achieving depth sensitivity

2.2.2.1. Approach to depth discrimination

It was previously shown that an off-axis detection scheme provides information regarding the depth, z_{obj}, of an inhomogeneity embedded within a turbid slab of thickness d_0.[40,41] To obtain this information, one combines data from the on-axis detector, D_0, and a detector offset, by a distance δD, in the *x*-*y* plane. The location of a given inhomogeneity will appear shifted (along the direction of the detector offset) between the transmission intensity images of the on-axis and off-axis detectors. The magnitude of this shift, Δ, can be normalized to δD yielding $\alpha = \Delta/\delta D$,[40] where α is a dimensionless parameter that is related to the normalized depth, z_{obj}/d_0. Furthermore, to achieve depth sensitivity for linear structures along *x*, we included an off-axis detector D_{+y} (offset along the positive

y-direction). By measuring the parameter α and the thickness of the medium, d_0, the depth of an absorbing structure can be found for any pair of detectors using a calibration curve relating α to z_{obj}/d_0. For example, for the detector D_{+x}, $\alpha_{+x} = \Delta_{+x}/\delta D_{+x}$, where Δ_{+x} is the measured spatial shift along the positive *x*-direction between the structure in the image generated by D_{+x} and the one generated by D_0, and δD_{+x} is the detector offset in the +*x*-direction. Similarly, α_{-x}, and α_{+y} can be recovered using the spatial shifts measured from detectors D_{-x} and D_{+y}, respectively. It was previously shown that this calibration curve is weakly dependent on the background optical properties of the medium and on the source-detector separation.[40,41] Also, depth reconstruction using this method is not affected by the contrast between the structure and the background medium because it is based on the spatial offset of intensity minima. As a result, for our experiments, we use simple black inclusions of varying shapes to show the capabilities of our instrument and this technique.

2.2.2.2. Comparison of theoretical and experimental depth calibration curve

A first-order perturbation approach within diffusion theory in an infinite slab geometry was used to derive the depth calibration curve, henceforth called the "depth curve", which translates measured values of α into the corresponding values of z_{obj}/d_0. In the diffusion based calculations, a single highly absorbing (effectively black) perturbation with a volume of 8 mm^3 is embedded in a turbid infinite slab with optical properties $\mu_a \sim 0.04$ cm^{-1} and $\mu_s' \sim 9$ cm^{-1} and thickness $d_0 = 60$ mm. Perturbation theory was used to generate 1D line scans with two detection optical fibers separated by $\delta D = 20$ mm. The calculations were carried out for depths of the inhomogeneity, z_{obj}, in the range 4 – 56 mm.

We also acquired an experimental depth curve in order to assess the discrepancy between an experimental measurement of the depth curve in a slab geometry with finite

boundaries and the theoretical depth curve derived from diffusion theory in an infinite slab geometry. For this, we used two wedge-shaped silicone phantoms (labeled "1" and "2" in Figure 2.2A) with optical properties $\mu_a \sim 0.04\ \text{cm}^{-1}$ and $\mu_s' \sim 9\ \text{cm}^{-1}$ at 690 nm, which are combined into a rectangular block that allows for a thin inclusion to be inserted between the two phantoms. A transparency sheet with a single 7.5 mm wide black line was printed and used as an inclusion between these two pieces. For this experiment, two separate scans were performed: the first scan with a single detector collinear to the source (D_0), and the second scan with a single detector offset by $\delta D = 20$ mm (D_{+x}) (Figure 2.2B). The detector offset was chosen as a compromise between the depth sensitivity and the size of the imaged area. Increasing δD would increase our depth sensitivity, however the area imaged by both detectors would decrease. We found that, given our spatial sampling rate, a 20 mm detector offset provided good depth sensitivity. Each scanned line along the *x*-direction sampled the depth-varying inclusion at a unique depth. The spatial sampling rate of our data ($0.5\ \text{mm}^{-1}$) was increased to $2\ \text{mm}^{-1}$ by 2D spline interpolation after low-pass filtering with a 2D moving average to reduce the intensity noise-level. The inherently low spatial resolution afforded in diffuse optics allows interpolation to provide a finer spatial grid that mimics collecting data with a higher spatial sampling rate. Using this data interpolation, the shift in location of an inclusion between the images collected with the collinear and offset detectors (D_0 and D_{+x}) can be measured with greater precision. That is, if the true intensity minimum associated with a structure were to occur between two sampled points in the intensity image, interpolation provides a better measure of the shift in location. If the true minimum is sampled exactly by a pixel in the intensity image, interpolation does not affect the measured depth. The depth of the inclusion at each *x*-line was associated to a

corresponding value α_{+x} by dividing the measured shift (Δ_{+x}) by the detector offset δD_{+x} = 20 mm. By relating the measured value of α_{+x} to the known value of z_{obj}/d_0 a depth curve was created.

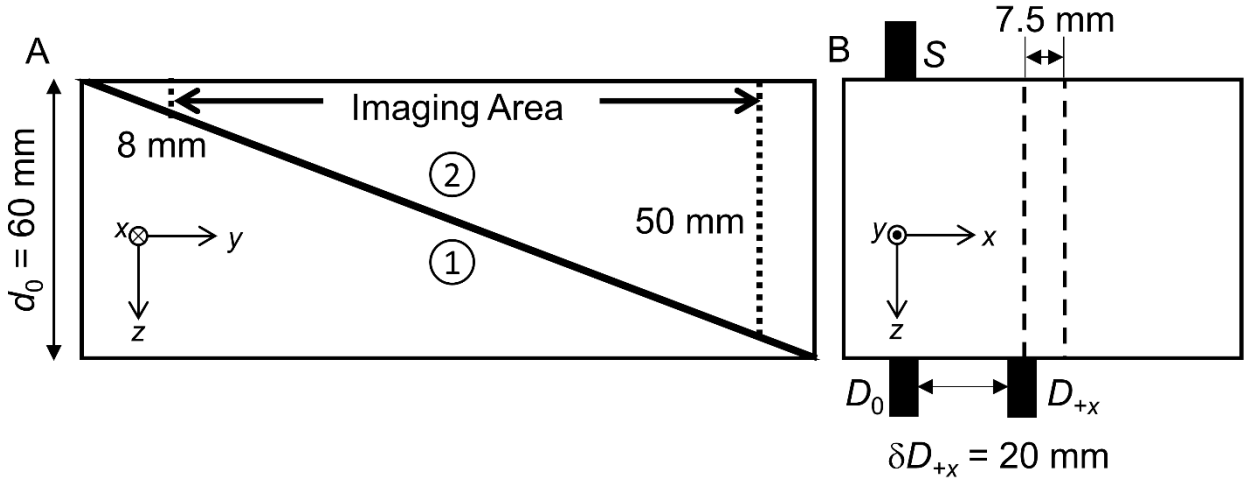

Figure 2.2: Description of the tissue-like phantom to experimentally derive the relationship between α and z_{obj}/d_0. (A) Lateral view of the combined phantom. A black strip 7.5 mm wide is printed on a transparency sheet and is used as an optical inclusion between the two halves (labeled 1 and 2) of the phantom. The inclusion is imaged from depths ranging from 8-50 mm. (B) Front view of the same phantom depicting the location of the inclusion and the source (S), collinear detector (D_0) and off-axis detector (D_{+x}), which is offset by δD_{+x} = 20 mm. The optical properties of the phantom at 690 nm are $\mu_a \sim 0.04$ cm^{-1} and $\mu_s' \sim 9$ cm^{-1}.

2.2.2.3. Performance test on a breast-shaped phantom

We have previously presented the depth recovery method in an infinite-medium geometry, where boundary effects are absent,[40] and we have presented the case of a semi-infinite slab geometry in the previous section. To address the capability of our instrument to perform depth measurements in a geometry that is more representative of a real breast, we designed a breast-shaped optical phantom made of silicone ($\mu_a \sim 0.04$ cm^{-1}, $\mu_s' \sim 9$ cm^{-1} at 690 nm) depicted in Figure 2.2.

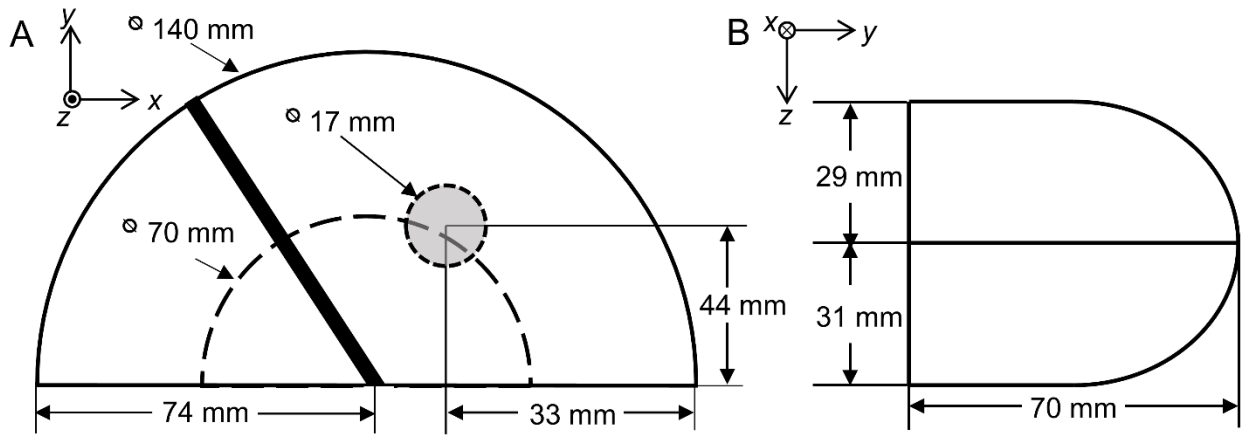

Figure 2.3: Drawing of breast shaped optical phantom. (A) Top view of two inclusions placed on the phantom. The grey circle is black tape placed between the two solid halves of the phantom (z_1 = 29 mm) and the solid black line is a 3 mm wide strip of black tape placed over the top of the phantom (z_2 = 0 mm). (B) A lateral view of the phantom depicting the two halves. The total thickness of the phantom is d_0 = 60 mm. The optical properties of the phantom at 690 nm are $\mu_a \sim 0.04$ cm^{-1}, $\mu_s' \sim 9$ cm^{-1}.

The phantom has a semi-circular projection with a diameter of 140 mm. A 70 mm diameter portion of the phantom (outlined by a dashed semi-circle in Figure 2.3A) is of uniform thickness to resemble the portion of the breast in contact with the polycarbonate plates. A 17 mm diameter circle of black tape was placed between the two halves of the phantom (z_1 = 29 mm) to mimic a deeply embedded tumor. A 3 mm wide strip of black tape was placed along the surface of the top half of the phantom (z_2 = 0 mm) to mimic a superficial blood vessel. The phantom was imaged using a detector offset of δD = 20 mm for all three directions (+*x*, −*x*, and, +*y*), recovering intensity images from D_{+x}, D_{-x}, and D_{+y} simultaneously over the wavelength range 650-1000 nm. The same low-pass filter and interpolation used in Section 2.2.2.2 were applied to the intensity images recovered simultaneously from the four detectors. Since this method is largely insensitive to the absorption and scattering properties of the background medium,[40,41] and since we used a black absorber, we maximized the contrast-to-noise ratio by using the integrated spectrum of the transmitted intensity at each pixel.

To account for the shape-based edge effects associated with the variable slab thickness, a normalization was applied using information from the intensity image at 912 nm. At 912 nm, the absorption of silicone has a peak and subsequently the background absorption from the phantom is the highest. At this wavelength, we minimize the contrast of the two black structures, and spatial variations in the intensity are dominated by fluctuations associated with the shape of the phantom. We divided the integrated intensity image by the one recovered at 912 nm, as a method of removing changes in intensity resulting from changes in thickness. The resulting image was then normalized to its maximum value creating a normalized intensity image at each detector. We represent these images taken from D_0, D_{+x}, D_{-x}, and D_{+y} with the matrices of normalized, interpolated intensity data $\mathbf{N}_0$, $\mathbf{N}_{+x}$, $\mathbf{N}_{-x}$, and $\mathbf{N}_{+y}$, respectively, where $\mathbf{N}_0(x_0,y_0)$ represents the normalized intensity value taken from D_0 at source location (x_0,y_0). We observe that we have previously presented an alternative method for tissue thickness correction for breast measurements *in vivo*, which is based on data collected at an optimal wavelength of 925 nm.[17]

The location of the circle and stripe structures in the on- and off-axis images need to be identified to measure their corresponding spatial shifts between images taken from different detectors. To do this, regions of interest (ROIs) (or submatrices) within $\mathbf{N}_0$ were first defined for the circle ($\mathbf{n}_{\text{circ},0}$) and stripe ($\mathbf{n}_{\text{stripe},0}$) as templates to identify similar regions in off-axis images. Here, the location of $\mathbf{n}_{\text{circ},0}$ was defined by the location of its first element (at the top-left of the ROI). Meaning, if $\mathbf{n}_{\text{circ},0}(1,1) = \mathbf{N}_0(x_1,y_1)$ then the location of $\mathbf{n}_{\text{circ},0}$ is (x_1,y_1) . To define $\mathbf{n}_{\text{circ},0}$, the center of the circle inhomogeneity was identified by a local minimum in $\mathbf{N}_0$, and it was used to define the center of a 17 mm (34 pixel) square region. The ROI for the stripe, $\mathbf{n}_{\text{stripe},0}$, was defined by finding minima along $\mathbf{N}_0(x, 36)$ and

$\mathbf{N}_0(x, 0)$, where 36 and 0 were the y location in mm of the top and bottom of the stripe, respectively. These two points identified the center locations of the stripe along the x-direction and were used as the top-left and bottom-right corners for the rectangular 22×36 mm^2 (44×72 pixel^2) ROI, $\mathbf{n}_{\text{stripe},0.}$

The 2D cross-correlations were calculated between $\mathbf{n}_{\text{circ},0}$ or $\mathbf{n}_{\text{stripe},0}$ and ROIs of the same size taken from $\mathbf{N}_{+x}$, $\mathbf{N}_{-x}$, and $\mathbf{N}_{+y}$ to identify the location of the inhomogeneities in each off-axis image. For $\mathbf{N}_0$ and $\mathbf{N}_{+x}$ a registered ROI for the circle, $\mathbf{n}_{\text{circ},+x}$, was identified by shifting $\mathbf{n}_{\text{circ},0}$ pixel by pixel over the offset image in the $-x$-direction up to a distance of δD_{+x}. to maximize the value of the 2D cross-correlation between $\mathbf{n}_{\text{circ},0}$ and the offset ROIs of equal size in $\mathbf{N}_{+x}$. Then the magnitude of the shift for the circle between $\mathbf{N}_0$ and $\mathbf{N}_{+x}$, $\Delta_{+x,1}$, is defined as the difference in location between $\mathbf{n}_{\text{circ},+x}$ and $\mathbf{n}_{\text{circ},0}$. Since the shift should only occur along the offset direction, only the magnitude of the difference in x locations between $\mathbf{n}_{\text{circ},+x}$ and $\mathbf{n}_{\text{circ},0}$ is considered for $\Delta_{+x,1}$. Similarly, regions in the other off-axis images for the circle $\mathbf{n}_{\text{circ},-x}$ and $\mathbf{n}_{\text{circ},+y}$, and the regions for the stripe, $\mathbf{n}_{\text{stripe},+x}$, $\mathbf{n}_{\text{stripe},-x}$, and $\mathbf{n}_{\text{stripe},+y}$ can be identified to calculate their respective shifts, $\Delta_{-x,1}$ and $\Delta_{+y,1}$ for the circle, and $\Delta_{+x,2}$, $\Delta_{-x,2}$, and $\Delta_{+y,2}$ for the stripe. The maximum of the 2D cross-correlations between template ROIs and ROIs within the off-axis images were found using the *normxcorr2* function in MATLAB (R2012a, Mathworks, Natick, MA). The recovered shifts were then normalized by δD to obtain $\alpha_{+x,1}$, $\alpha_{-x,1}$, $\alpha_{+y,1}$ as the normalized shifts for the circle in each direction ($+x$,$-x$, and $+y$, respectively), and $\alpha_{+x,2}$, $\alpha_{-x,2}$, $\alpha_{+y,2}$ for the stripe in each direction. The theoretically derived depth curve described in Section 2.2.2.2 was used as a look-up table to assign a depth to each α value. The measured depth from all three directions for the circle, $z_{1,\text{meas}}$, and the stripe, $z_{2,\text{meas}}$, are reported in Section 2.3.2.

2.2.3. Dynamic spectroscopy on the finger

To determine the capability of our imaging system to measure physiological hemodynamics, we measured the arterial pulsation at the distal phalanx of the index finger of a 24 year old, male, healthy volunteer. The Tufts University Institutional Review Board approved the experimental protocol, and the subject provided written informed consent prior to the experiment. Transmitted intensity spectra were collected at 20 Hz for 60 s resulting in 1200 spectra. Only a single source-detector pair was used to collect data through the finger with the polycarbonate plates removed. The source-detector separation was 1.5 cm. From the raw intensity data, $I(\lambda,t)$, we calculated the relative intensity changes, $\Delta I(\lambda,t)/I_0(\lambda)$, where $I_0(\lambda)$ is the average intensity at each wavelength over time, and $\Delta I(\lambda,t) = I(\lambda,t) - I_0(\lambda)$.

To test the ability of our instrument to perform physiological hemodynamic measurements over the entire spectral range, we estimated the spectral shape of the change in the tissue absorption coefficient, $\Delta\mu_a(\lambda)$, using the modified Beer-Lambert law:[50]

$$\frac{\Delta I}{I_0}(\lambda, t) = -\Delta\mu_a(\lambda, t) \cdot DPF(\lambda) \cdot d \qquad (2.1)$$

where DPF(λ) is the differential pathlength factor and d is the geometrical source-detector distance. The DPF, which is defined as the ratio between the mean path length of detected photons in the scattering media and d, was assumed to be time-independent. The average heart rate was measured by taking the Fourier transform of $\Delta I/I_0(\lambda, t)$ and identifying the peak in the Fourier spectrum around ~1 Hz. We measured the amplitude of the oscillations in $\Delta I/I_0(\lambda)$ at the heart rate, $|\Delta I/I_0|_{HR}(\lambda)$, by integrating the Fourier coefficients around the peak pulsation frequency (1.16 – 1.33 Hz) at each wavelength. Assuming that the changes in attenuation are dominated by changes in the volume of arterial blood in tissue, we can

omit the contributions of changes in blood flow, [lipids], and [water] to relate $|\Delta I/I_0|_{HR}(\lambda)$ directly to the change in tissue absorption due to arterial pulsation, $\Delta\mu_{a|HR}(\lambda)$. Since we were only interested in recovering the arterial saturation, we only needed the spectral shape of $\Delta\mu_{a|HR}(\lambda)$ to within a factor. Accordingly, we used a DPF spectrum normalized to its value at 790 nm measured by Kohl *et al*.[51] We solved for $\Delta\mu_{a|HR}(\lambda)$ from Equation (2.1) using this normalized spectrum of the DPF, the measured values of $|\Delta I/I_0|_{HR}(\lambda)$, and *d*. We then normalized $\Delta\mu_{a|HR}(\lambda)$ to its value at 790 nm and fit it with the known absorption spectra of hemoglobin also normalized to 790 nm (which depend only upon the saturation of hemoglobin) to recover the arterial saturation.

2.2.4. Dynamic spectroscopy on the breast

We tested the sensitivity of our system to physiological dynamics induced by systemic changes in blood pressure, and acquired time-resolved spectra in the breast. One healthy female subject (24 years old) participated in the study. The Tufts University Institutional Review Board approved the experimental protocol, and the subject provided written informed consent prior to the experiment. The subject's breast was placed between the scanning plates of the optical mammography system and gently compressed to keep the breast stationary. Pneumatic thigh cuffs were wrapped around both of the subject's legs and inflated using an automatic cuff inflation systemic (E-20 rapid Cuff Inflation System, D. E. Hokanson, Inc., Bellevue, WA) to induce systemic changes in arterial blood pressure. Intensity spectra from 650 – 1000 nm were recovered at 5 Hz with the fibers positioned in the center of the breast close to the chest wall to mitigate boundary effects.

Baseline measurements, during which the subject is at rest and the thigh cuffs are deflated, were recorded for two minutes. To induce cyclic changes in blood pressure at a

given frequency, the thigh cuffs were then periodically inflated (to a pressure of 200 mmHg) and deflated at a frequency of 0.05 Hz for a total time of two minutes. Slow temporal drifts in the data were removed by detrending the intensity data with a third-order polynomial. The plate separation was $d = 52$ mm. The modified Beer-Lambert law Equation (2.1)[50] was used to obtain time traces of the absorption changes, the changes in tissue concentrations of hemoglobin, $\Delta[HbO_2]$, $\Delta[Hb]$, and $\Delta[HbT]$ by the following relationship:

$$\Delta\mu_a(\lambda) = \Delta[HbO_2] \cdot \varepsilon_{HbO_2}(\lambda) + \Delta[Hb] \cdot \varepsilon_{Hb}(\lambda) \quad (2.2)$$

where, $\varepsilon_{HbO_2}(\lambda)$ and $\varepsilon_{Hb}(\lambda)$ are the molar extinction coefficients of oxy- and deoxyhemoglobin, respectively. The coefficients $\varepsilon_{HbO_2}(\lambda)$ and $\varepsilon_{Hb}(\lambda)$[52] and the wavelength dependence of the DPF[51] are known from the literature, and an absolute value of the DPF was chosen at 700 nm to be 7[5]. Using relative intensity data from 700 – 970 nm (where the wavelength dependence of the DPF was defined[51]), $\Delta\mu_a(\lambda)$ was calculated from Equation (2.1) The magnitude of $\Delta[HbO_2]$, $\Delta[Hb]$ and subsequently $\Delta[HbT]$ were obtained from Equation (2.2) in the least squares sense using the *linsolve* function in MATLAB.

2.3. Results

2.3.1. Signal-to-noise characterization on a tissue-like phantom

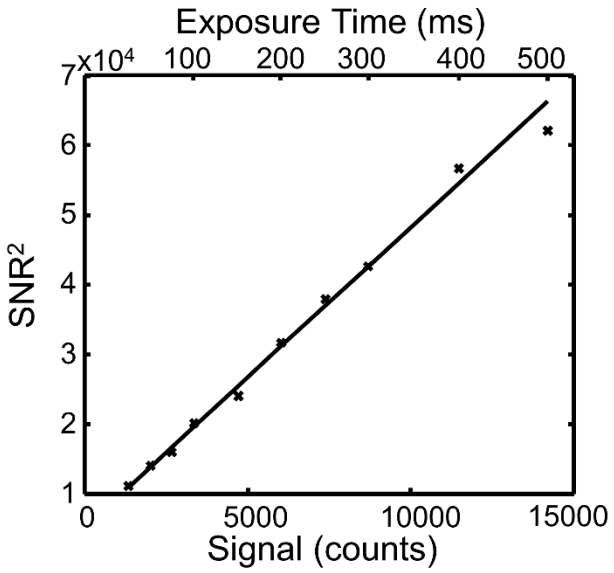

Figure 2.4: Results of SNR measurement on an optical phantom. The SNR^2 shows a linear dependence on the number of detected CCD counts. With a 2 MHz A/D rate and a gain setting of 3, the CCD sensitivity is about 1 e^-/count. The symbols refer to data taken at 830 nm over exposure times ranging from 0-500 ms. The thickness of the phantom was 60 mm while its optical properties at 690 nm were $\mu_a \sim 0.04\ cm^{-1}$, $\mu_s' \sim 9\ cm^{-1}$.

We measured the SNR of the transmitted intensity over the spectral band of interest (650 – 1000 nm) by using a rectangular optical phantom made of silicone that mimics the optical properties of breast tissue (d_0 = 60 mm, $\mu_a \sim 0.04\ cm^{-1}$, $\mu_s' \sim 9\ cm^{-1}$ at 690 nm). Using a 90 mW illumination power we measured the SNR^2 as a function of the resulting signal by adjusting the CCD exposure time (Figure 2.4). The SNR^2 as a function of optical signal detected by the CCD at 830 nm for the on-axis fiber is reported in Figure 2.4. The measured SNR^2 is linearly dependent on the optical signal detected by the CCD for all four fibers which is indicative of noise dominated by the statistical variation of photons arriving at the detector, also termed shot noise (which follows a Poisson distribution). At the

exposure time of 100 ms the SNR for the intensity measurements on the optical phantom ranged from 67 – 130 (equivalent to less than 1.5% intensity noise) over the wavelength range 650 – 1000 nm.

2.3.2. Depth Discrimination

2.3.2.1. Experimental validation of the depth curve

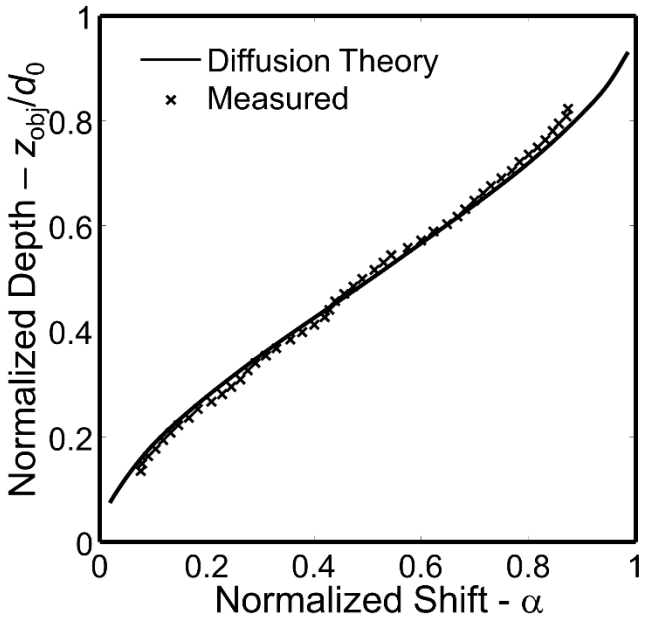

Figure 2.5: Comparison between measured (crosses) (see the experimental setup in Fig. 2) and theoretically calculated (solid line) depth curve. The theoretical depth curve is obtained by using a first order perturbation within diffusion theory using an infinite slab with experimental parameters similar to the experimental setup - d_0 = 60 mm and background optical properties at 690 nm of μ_a =0.04 cm^{-1} and μ_s' = 9.0 cm^{-1}.

We experimentally measured a depth curve and compared it to a theoretical depth curve obtained using diffusion theory (Figure 2.5). We measured the depth of an inclusion for depths ranging from z_{obj} = 8 – 50 mm (z_{obj}/d_0 = 0.13 – 0.83) resulting in Δ_{+x} = 1.5 – 18 mm (α_{+x} = 0.08 – 0.89). The measured depth curve closely approximates the theoretical curve with a discrepancy in Δ_{+x} to within 0.5 mm, which is equivalent to the size of one interpolated pixel. The average discrepancy in Δ_{+x} of 0.28 ± 0.13 mm

($\alpha_{+x} = 0.014 \pm 0.006$). The only exceptions, where the discrepancy in Δ_{+x} is greater than 0.5 mm, occur when the fibers are scanned to within 2.5 cm of the phantom's edge, where the maximum discrepancy in Δ_{+x} is 0.8 mm. We attribute this larger error to shifts in the intensity minima due to edge effects resulting from light leakage through the side of the phantom. Accordingly, we use the theoretical depth curve for the rest of this work.

The accuracy with which a depth can be assigned to a given inhomogeneity using this method is dependent on the accurate estimation of α. The measured values of α depend on the pixel width, k, and the detector offset δD, and are consequently discretized into N 'bins' where N is the nearest integer value of $\delta D/k$. For example, in the case of this experiment, $k = 0.5$ mm and $\delta D = 20$ mm, so α is discretized into 40 bins. Since the relationship between α and z_{obj}/d_0 is non-linear, the estimation of depth will inherently have an error that depends non-linearly on the depth, and each 'bin' will correspond to a different accuracy based on the z-location of the inhomogeneity. However, by dividing d_0 by N, we obtain an estimate of the average bin width in z, $d_0/N = 1.5$ mm. This value is an approximate measure of the accuracy with which a depth can be assigned to a given inhomogeneity within these experimental parameters. Note that by changing d_0, k, or δD, the accuracy of the depth measurement is altered. In a clinical setting, we do not have control over d_0, however k and δD are adjustable system parameters. Ideally, a larger value of δD would improve our measurement accuracy, but we chose $\delta D = 20$ mm to maximize the area around the edges of the breast from which depth information can be recovered. The value of k can be decreased through further interpolation, but this provides minimal improvements in accuracy due to the physical limitation of the source and detector fiber diameters and the spatial resolution afforded in diffuse imaging.

2.3.2.2. Recovery of depth on a breast shaped phantom

We tested the depth discrimination capabilities of our system using a silicone optical phantom designed to simulate the shape and optical properties of the human breast. The depth of two optical inclusions, a circle (z_1 = 29 mm) resembling a tumor and a black stripe (z_2 = 0 mm) resembling a superficial blood vessel (Figure 2.3) were recovered using information from D_0, and the three offset detectors, D_{+x}, D_{-x}, and D_{+y} (Figure 2.6).

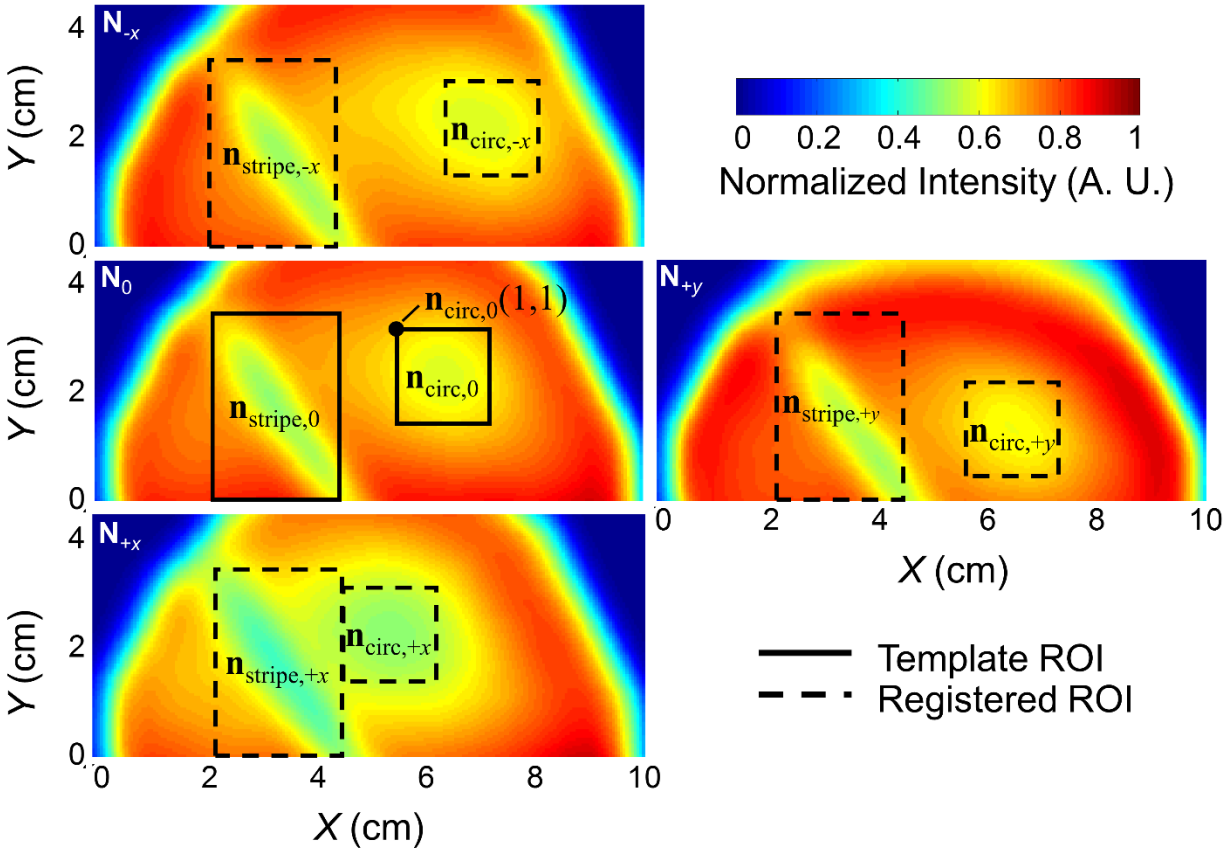

Figure 2.6: Experimental result of depth recovery for the circle and single black stripe in a breast shaped phantom. Interpolated normalized intensity images for the four detectors are shown. The solid boxes represent the template ROI ($\mathbf{n}_{circ,0}$ for the circle and $\mathbf{n}_{stripe,0}$ for the black stripe) selected from the D_0 image, and the dashed boxes represent the registered ROIs in the off-axis images where the circle and stripe structures were found. The shift in the ROI of the circle for $\mathbf{N}_{+x}$ was $\Delta_{+x,1}$ = 10 mm ± 0.5 mm associated with a recovered depth of $z_{1,meas}$ = 30 ± 1 mm where the exact depth was 29 mm. The shift in the ROI of the stripe was $\Delta_{+x,2}$ = 0 ± 0.5 mm associated with a recovered depth of $z_{2,meas}$ = 0 ± 5.6 mm where the exact depth is 0 mm.

The registered ROI, $\mathbf{n}_{\text{circ},+x}$, and the template ROI, $\mathbf{n}_{\text{circ},0}$, had a 2D cross correlation value of 0.95. The shift between the two ROIs was $\Delta_{+x,1} = 10 \pm 0.5$ mm translating to a depth of $z_{1,\text{ meas}} = 30 \pm 1$ mm where the actual depth was $z_1 = 29$ mm. The registered ROIs for both the circle and the stripe in all images were always representative of unique maxima. Meaning, in $\mathbf{N}_{+x}$ (as well as the other images), no other regions exist that had 2D cross-correlations with $\mathbf{n}_{\text{circ},0}$ equal to or greater than 0.95. For $\mathbf{N}_{-x}$ and $\mathbf{N}_{+y}$ the recovered shifts $\Delta_{-x,1}$, and $\Delta_{+y,1}$ were also 10 ± 0.5 mm. Similarly, the shift measured between $\mathbf{n}_{\text{stripe},+x}$ and $\mathbf{n}_{\text{stripe},0}$ was $\Delta_{+x,2} = 0 \pm 0.5$ mm. The same shift was measured for all three directions associated with a recovered depth of $z_{2,\text{ meas}} = 0 \pm 5.6$ mm where the actual depth was $z_2 = 0$ mm. The errors are defined by assuming a one-pixel inaccuracy in the measurement of the shifts and translating that error to the depth based on the depth curve. The 2D cross-correlations between template and registered ROIs were always at least 0.95. The discrepancy between the actual depth of each object and the measured depth of each object is within the previously defined measurement error of ~1.5 mm.

2.3.3. Dynamic spectroscopy on the finger

We tested the temporal sensitivity of our imaging system by measuring the arterial pulsation in the subject's index finger over the course of 60 s. In Figure 2.7A the relative intensity changes $\Delta I/I_0$ over time at 820 nm are observed for a time period of 10 s. At a 20 Hz acquisition rate, each individual pulse over the entire wavelength range (650 – 1000 nm) is visualized.

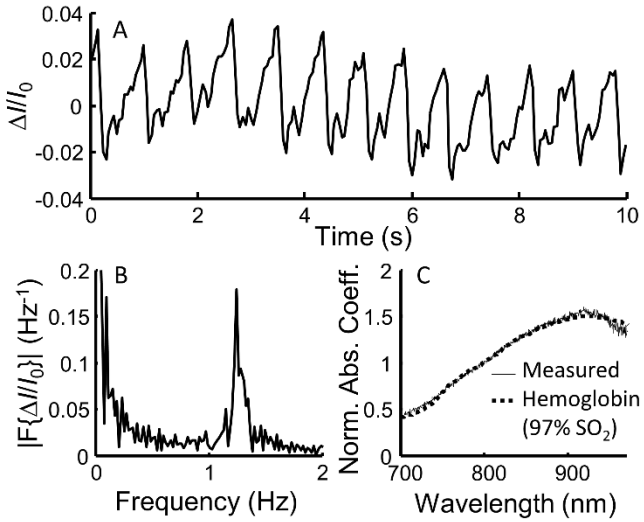

Figure 2.7: Measurement of arterial pulsation and normalized hemoglobin absorption coefficient in the index finger of a human subject. (A) Relative intensity changes over 10 s at 820 nm. (B) Magnitude of Fourier coefficients of $\Delta I/I_0$ over the 60 s acquisition at 820 nm. (C) Change in the absorption coefficient normalized to 790 nm recovered from the magnitude of the Fourier components. The dashed line represents the normalized absorption of total hemoglobin with an oxygen saturation of 97%.

The Fourier spectrum has a clear peak at 1.27 Hz corresponding to a heart rate of 76 bpm (Figure 2.7B). The FWHM of the peak is ~0.1 Hz, corresponding to a width of 6 bpm, which is comparable to the normal fluctuations in the heart rate over a period of 60 s.

We use the magnitude of the peak in the Fourier spectra surrounding the heart rate at each wavelength, $|\Delta I/I_0|_{HR}(\lambda)$, to calculate the change in the tissue absorption coefficient due to arterial pulsation, $\Delta\mu_{a|HR}(\lambda)$ (Figure 2.7C). We recovered a 97% oxygen saturation of hemoglobin by fitting $\Delta\mu_{a|HR}(\lambda)$ with the molar extinction spectrum of hemoglobin with oxygen saturation as the fitting parameter. The average discrepancy between the curves (Figure 2.7C) is 0.9% with the largest errors (~7%) observed at the extremes of the measured spectral range where the error in the measured wavelength dependence of the DPF is the largest.[51]

2.3.4. Dynamic spectroscopy in the breast.

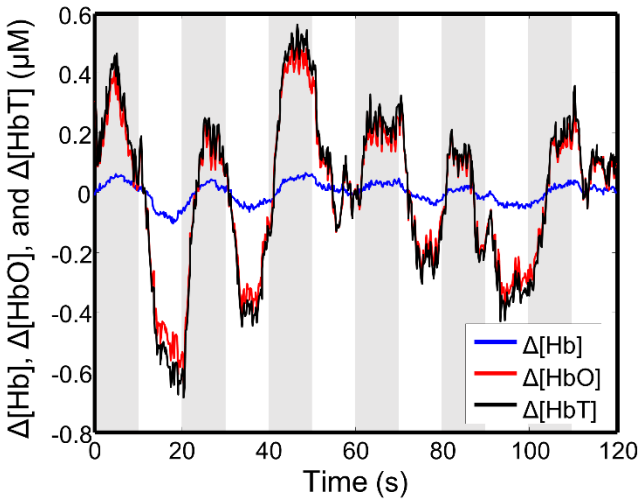

Figure 2.8: Measurement of changes in $\Delta[HbO_2]$, $\Delta[Hb]$, and $\Delta[HbT]$ in a single location of the breast as a result of induced oscillations from pneumatic thigh cuffs. Shaded areas indicate the periods when the cuffs are fully inflated to 200 mmHg, and white areas indicate the periods when the cuffs are deflated. Each inflation cycle lasts 20 s, with the cuffs inflated for ~10 s and deflated for ~10 s.

Figure 2.8 shows measurements of $\Delta[HbO_2]$, $\Delta[Hb]$, and $\Delta[HbT]$ in the breast of a healthy subject induced by the cyclic inflation of a pneumatic thigh cuff as described in Section II.D. Periods of cuff inflation are shaded in Figure 2.8. Inflation of the cuffs induced an increase by ~0.5 – 1 μM in $\Delta[HbO_2]$ and an increase by ~0.1 – 0.2 μM in $\Delta[Hb]$. Based on typical values of hemoglobin concentration in breast tissue (15 – 30 μM), this is indicative of approximately a 2 – 8% fluctuation in total hemoglobin content. The oscillations of $\Delta[HbO_2]$, $\Delta[Hb]$, and $\Delta[HbT]$ are all in phase with each other and with the cuff inflation, suggesting that the observed changes are associated with a blood volume oscillation induced by the change in blood pressure.[53]

2.4. Discussion

We have reported an instrument for optical mammography that can measure broadband spectral data (wavelength range: 650 – 1000 nm) with high spatial sampling (25 cm^{-2}) and

recover the depth of embedded absorbing structures to within 1 mm. We also showed that this system has the capability to resolve temporal dynamics with an acquisition rate as high as 20 Hz, as demonstrated by measuring induced hemodynamics in the breast. The spectral information provided by this method allows for the generation of 2D concentration maps of the major absorbing chromophores in breast tissue (deoxyhemoglobin, oxyhemoglobin, lipids, and water).[8] Furthermore, we apply this spectral information to recover the arterial saturation of a healthy volunteer from dynamic measurements taken on his finger. We observe that while the absolute value of the DPF is strongly dependent on the value of the reduced scattering coefficient (as determined by the tissue architecture, cellular density, etc.) and the absorption coefficient (as determined by vascularization, blood volume, etc.), the spectral shape of the DPF is mostly determined by the wavelength dependence of the scattering and absorption coefficients. Such wavelength dependence, being related to the cellular size distribution and hemoglobin saturation, respectively, is comparable in various soft tissues under rest conditions, and this justifies the application of the cerebral DPF wavelength dependence to finger tissue. In the remainder of this work, we focused on the depth information realized through an off-axis detection scheme, and the dynamic information obtained through measuring intensity spectra at a single location.

This instrument is capable of identifying the depth of specific inhomogeneities observed in a 2D projection with a single scan of four detection fibers simultaneously. By spatially multiplexing detection fibers into a large CCD chip, this instrument can assess depth without requiring additional scans for each offset direction, and, more importantly, this method avoids patient movement between scans and does not require calibration measurements. The accuracy of the depth assessment is mostly affected by the detector

offset δ*D*. A larger detector offset can improve the accuracy of the depth assessment, but it would also increase the source-detector distance and reduce the SNR accordingly. Furthermore, a large offset may introduce artifacts close to the edges of the breast where inhomogeneities may not appear in all detector images.

We reported here a method to apply this technique to a breast-shaped phantom using cross-correlation to validate its efficacy in a curved, slab geometry (Figure 2.6). In the simplest case, the location and size of absorbing structures are known *a priori*, and the structures of interest are separated by a distance greater than δ*D*. Here, the cross-correlation serves as an accurate measure of the spatial offset of different structures. The average reported error of 1.5 mm in depth assessment is associated with the discretization of the depth look-up table due to the physical dimensions of our source-detector setup and the experimental parameters. In the simple case of a single structure or multiple structures separated by a distance greater than δ*D*, the accurate pairing of spatial locations is a simple task, and the error associated with it is ignored. However, in a real breast, the complex network of blood vessels and the intrinsic tissue heterogeneity complicates the depth discrimination method.

The main challenge in extending this method to the real breast is eliminating the requirement for *a priori* information. Kainerstorfer *et al.*[40] have detailed a robust algorithm where a window-based registration is done by pairing ROIs that are smaller than δ*D* surrounding vessel-like structures. Additionally, this method uses a spatial second derivative to improve the contrast of absorbing structures in the case where intensity minima are ambiguous. This method does not rely on *a priori* information. However, the challenge in applying this window method to spherical objects is that if the optical footprint

of the object is larger than δD, identifying an accurate minimum could still be ambiguous. Although increasing the window size may avoid this issue, a larger window may encompass more than one structure at multiple depths where assigning Δ to the appropriate structures becomes difficult. This method can still be a valuable tool, since presumably even if only a portion of the object is encompassed by the window, the same portion would exist in the offset image. However, the error when using this registration method on a dense array of unknown structures (as is the case in the human breast) needs to be further investigated. It is likely that although we can achieve an error in our depth assessment of ~1.5 mm in ideal conditions, the additional error associated with measuring Δ in a more complex case will reduce the accuracy of these measurements. Different approaches to generate images with selective depth sensitivity from additional off-axis information are based on phased-array[43] or tomosynthesis[42] schemes. These methods generate 2D images with selective sensitivity at different depths without *a priori* knowledge of the location or shape of the detected inhomogeneities. In this way, the location of detected lesions can be assessed in 3D.

The coarse depth resolution provided by our method and alternative methods based on limited off-axis information[42,43] makes them unsuitable to generate detailed 3D spatial maps comparable to full 3D reconstructions. However, the depth information they provide is still valuable and effectively complements the 2D spatial information of projection images. The depth information can improve the instrument's sensitivity to spatial changes in chromophore concentrations by allowing for a more accurate implementation of a perturbation based diffusion model.[26] Additionally, depth information regarding detected

blood vessels can determine whether they are superficially located, or are larger feeding vessels that present high contrast near a breast tumor.

Dynamic measurements done on the breast show the sensitivity of our instrument to induced changes in hemodynamics. A challenge with inducing hemodynamic changes is to separate direct mechanical effects of the stimulus from the hemodynamic response of interest. In cases where breast compression is applied using the measurement hardware (e.g., scanning plates or a hand-held probe), careful consideration is required to ensure changes in detector contact from the applied pressure to the tissue do not affect the measurement. Additionally, when the patient is required to regulate their own respiration, such as with the Valsalva maneuver, patient compliance can become an issue. To visualize similar controllable hemodynamics in the breast, we induced systemic blood pressure changes with cuffs around the thighs. In this way, we provide a hemodynamic stimulus that requires no effort from the patient, and is completely independent of the measurement hardware. It can induce changes in total hemoglobin content of a similar magnitude to those obtained using manual compression or regulated respiration while minimizing artifacts. Furthermore, our multiplexed detection system can be easily adapted to measure multiple regions of interest (such as healthy and cancerous tissue) simultaneously. Defining an ROI for dynamic measurements is another challenge when studying breast cancer patients. For the purpose of detecting cancer signatures in the temporal data, an initial 2D spatial map can be obtained to identify suspicious locations for further hemodynamic study. This combination of measurement schemes can provide additional specificity when static optical imaging is insufficient to differentiate breast cancer. In the case of monitoring

neoadjuvant chemotherapy, the cancer location is known *a priori* and can be used to define ROIs for dynamic measurements.

This system incorporates robust methods to recover 5D (three spatial, spectral, and temporal) information in a practical fashion for application in a clinical setting. While FD and TD systems can recover spectral information with multiple light sources and detectors, achieving high spectral sampling (<10 nm) grossly increases these systems' complexity. However, CW systems lack the capability to recover unique absorption and scattering properties and an assumption about scattering must be used. This assumption affects the absolute values of [Hb], [HbO_2], [water], and [lipids], measured, but the spatial variability in the concentration of these parameters is still robust. Additionally, the parallel plate geometry is ideal for recovering spatial information without manually sampling fixed locations of the breast as would be required with hand-held probes.[27,54] While not only is this extremely time-consuming using a hand-held probe, it is also prone to motion artifacts and measurement variability due to user error. More importantly, since the entire breast is imaged, multiple images can be co-registered to measure changes in tissue properties over time allowing for studies that monitor neoadjuvant chemotherapy patients. However, parallel-plate measurements suffer when tumors are situated close to the chest wall. Tomographic systems with circular arrangements of detectors, especially those that perform measurements on the pendulous breast, provide more detailed spatial information without losing information close to the chest wall. However, the need for extensive calibration and matching fluids make implementing such techniques impractical, especially in a clinical setting.[46] Furthermore, this system has the advantage of being able to provide

spatial information from static images, and dynamic information at a targeted location, which neither hand-held probes or tomographic systems are well suited for.

2.5. Conclusions

The instrument presented here highlights the advantage of diffuse optics to non-invasively acquire both functional and structural information simultaneously to help diagnose and monitor breast cancer while limiting burden to the patient. We have demonstrated both the flexibility of this system to measure a number of relevant physiological parameters, and the simplicity with which the measurements are done. From an investigative standpoint this allows us to maximize the information we collect and use it to identify key physiological parameters that can translate to clinical diagnoses. Furthermore, the additional spatial information we collect can help improve our sensitivity to suspicious lesions.

Chapter 3: Monitoring neoadjuvant chemotherapy using near-infrared spectroscopy

3.1. Background

Neoadjuvant chemotherapy (NAC) is administered to patients prior to surgery in an effort to reduce the primary tumor size, whereas adjuvant chemotherapy is administered following surgery in an effort to reduce the risk of residual disease and cancer recurrence. A patient's response to NAC may be assessed by physical exam or breast imaging (clinical response), or by histology post-surgery (pathologic response)[55,56]. Assessing response to neoadjuvant treatment is crucial, as a pathologic complete response (pCR), defined by having no residual carcinoma in the resected breast tissue and in axillary lymph nodes, has been associated with improved survival[56–59]. Strictly defined, pCR requires the absence of invasive tumor in the resected specimen, although some clinicians use the more restrictive requirement of no residual invasive or *in situ* disease[57]. Because of the better outcome associated with pCR, finding tools that can define the individual clinical response during the course of therapy and accurately predict pathologic response would be of great benefit. This is also true in patients with poor response to treatment, as early identification of this problem may allow the physician to alter the chemotherapy regimen to avoid disease progression and to identify a more effective chemotherapy option.

3.1.1. Current imaging methods used to assess clinical response to NAC

Imaging methods sensitive to functional tissue changes are being investigated for monitoring breast cancer patients' response to neoadjuvant chemotherapy. Functional tumor changes are of particular interest due to the limitations of structural assessment of tumor response based on physical examination, ultrasound imaging, or mammography[60].

Current imaging methods used to assess clinical response are via a decrease in the standard uptake value (SUV) of 18-fluorodeoxyglucose (^{18}F-FDG) by positron emission tomography-computed tomography (PET/CT)[61,62], or a decrease in tumor size by contrast-enhanced magnetic resonance imaging (MRI)[61,62]. Both of these methods, however, are expensive and invasive, as PET/CT requires injection of a radiopharmaceutical, and MRI requires injection of gadolinium-based contrast. Furthermore, the appropriate timing and frequency for assessing clinical response have not been established, and studies thus far have typically imaged at a single time point during therapy[61,62].

3.1.2. Optical methods being investigated to monitor clinical response to NAC

Following initial case studies that first demonstrated using NIRS to study NAC[36,54,63], several groups have investigated optical methods to assess response to treatment in patients with breast cancer undergoing neoadjuvant therapy. Studies aiming to predict therapeutic response early in the treatment have shown significant differences between responders and non-responders one day[64] or one week[65–68] after the start of therapy. Other studies report the response during the course of treatment, typically using 3-8 measurement time points, to determine if and when different therapeutic response levels can be distinguished during NAC[69–79]. The primary focus of these studies has been on the chromophore concentrations measured at the tumor location over time, but some work has also focused on exploring the correlation between baseline, pre-treatment optical measurements and the level of response to NAC[71,77,80,81].

Studies that used the baseline tumor properties (before chemotherapy starts) as the reference to which all sequential measurements (during chemotherapy) are compared have found significant differences between responders and non-responders one or four weeks

after the start of chemotherapy[67,73] and after the first cycle of chemotherapy[71,74,77]. In a study on ten patients, Soliman *et al*. reported that at four weeks into chemotherapy, responders have a significantly greater decrease in deoxyhemoglobin and oxyhemoglobin ([Hb] and [HbO_2], respectively), and scattering power compared to non-responders using tomographic reconstructions[73]. Adding an additional five patients to the analysis performed by Soliman *et al*., Falou *et al*. examined a total of fifteen patients and found significant differences between the response groups at week 1 by examining the average properties taken over the entire cancerous breast (as opposed to just the tumor volume as previously done) [67]. Using the whole breast volume approach, [Hb] and [H_2O] were found to be the best predictive parameters for distinguishing response to treatment, with both [Hb] and [H_2O] increasing in responding patients and decreasing in non-responders[67]. Obtaining measurements using a handheld probe and applying tomographic reconstructions, Zhu *et al*. performed a study on thirty-two patients undergoing neoadjuvant chemotherapy and found that, after the first treatment cycle, the responding patients had a significantly larger decrease in total hemoglobin concentration ([HbT]) compared to non-responders[71]. Jiang *et al*. measured nineteen patients with a circular arrangement of optical fibers around the pendulous breast and found a significantly larger drop in [HbT] for pCR patients compared to an increase in [HbT] for incomplete responders within the first cycle of chemotherapy[77]. In another study on twenty-two patients using a parallel plate, planar geometry, Schaafsma *et al*. also found significant differences in response groups after the first cycle of chemotherapy, where responding patients showed a decrease in [HbO_2] and non-responders exhibited an increase in [HbO_2] [74]. When monitoring patients throughout the duration of therapy, hemoglobin parameters seemed to best differentiate response groups.

In particular, a consistent response to NAC is a decrease in the concentration of hemoglobin (often separated into the two components of oxy- and deoxy-hemoglobin) at the tumor location[36,54,63,65,66,68–75,77–79,82].

3.2. Methods

3.2.1. Optical imaging of patients with breast cancer

This study was approved by the Institutional Review Board of the Tufts Medical Center, and it was also compliant with the Health Insurance Portability and Accountability Act. Any woman over the age of 21 who was diagnosed with invasive breast cancer and scheduled to undergo neoadjuvant chemotherapy was eligible for this study. All patients read and signed an informed consent before participating. Ten patients undergoing neoadjuvant chemotherapy were imaged in this study. The patients will be referred to as neoadjuvant chemotherapy patients using the acronym "NACP," followed by an index number ranging from 1 to 10.

Relevant information about each patient enrolled is shown in Table 3.1. Patient recruitment took place from September 2014 to December 2015. Optical mammograms were obtained on both breasts 2-27 days before the treatment began (baseline measurement) and each time the patient underwent a chemotherapy infusion (the frequency and number of infusions are detailed in Table 3.1). For each measurement session the right breast was always imaged first. Figure 3.1 shows the chemotherapy schedule (specifying the corresponding drugs administered) for all ten patients in the study. To compare the effects of treatment across patients, each infusion time point was converted from week No. to "percentage of therapy complete" to normalize for the length of treatment (which ranged from 18 to 22 weeks). The breast cancer subtypes in our study are also reported for all

patients in Table 2: (1) positive for human epidermal growth factor receptor 2 (HER2+), (2) positive for estrogen receptors (ER) and negative for HER2 (ER+/HER2-), (3) negative for ER, progesterone receptors (PR), and HER2 (triple-negative breast cancer, TNBC) [61]. Four patients were premenopausal (NACP #1, 5, 7, 9), but chemotherapy caused a break in menstruation for all of them.

Table 3.1: Patient details and treatment regimens.

NACP #	Ref. #	Age (yr)	Pre-treatment cancer size (cm)		Cancer stage	Cancer subtype	Chemotherapy agent	Infusion frequency (number)	Treatment duration (weeks)	Post-treatment cancer size (Hist.) (cm)	NAC response
			MRI X-ray	Optical							
1	164	38	9.4	1.2	IIIC	ER+/ HER2-	Paclitaxel	Weekly (12)	31	6.0	NR (PR2)
							Capecitabine	Bi-weekly (5)			
2	163	72	3.2	2.1	IIB	TNBC	Doxorubicin, Cyclophosphamide	Bi-weekly (4)	23	-	R (pCR)
							Paclitaxel	Weekly (12)			
3	165	57	2.5	1.4	IIB	ER+/ HER2-	Doxorubicin, Cyclophosphamide	Bi-weekly (4)	22	0.9	R (PR1)
							Paclitaxel	Weekly (12)			
4	166	54	2.9	1.3	IIIA	HER2+	Carboplatin, Docetaxel, Trastuzumab, Pertuzumab	Every 3 weeks (6)	16	2.8	NR (PR2)
5	167	46	4.4	3.7	IV	HER2+	Carboplatin, Docetaxel, Trastuzumab, Pertuzumab	Every 3 weeks (6)	17	-	R (pCR)

6	168	47	6.0	4.4	IIB	TNBC	Doxorubicin, Cyclophosphamide	Bi-weekly (4)	21	0.4	R (PR1)
							Paclitaxel w/ Carboplatin (every 3rd)	Weekly (11)			
7	169	44	7.0	3.5	IIIA	ER+/ HER2-	Doxorubicin, Cyclophosphamide	Bi-weekly (4)	16	0.6	R (PR1)
							Paclitaxel	Bi-weekly (4)			
8	170	74	Inflam.	2.6	IIIB	ER+/ HER2-	Doxorubicin, Cyclophosphamide	Every 3 weeks (4)	20	1.7	R (PR1)
							Paclitaxel	Weekly (8)			
9	171	44	Inflam.	1.3	IIIB	ER+/ HER2-	Doxorubicin, Cyclophosphamide	Bi-weekly (4)	20	11.3	NR (PR2)
							Paclitaxel	Weekly (12)			
10	1730	56	4.5	1.9	IIB	HER2+	Carboplatin, Docetaxel, Trastuzumab, Pertuzumab	Every 3 weeks (6)	17	-	R (pCR)

Note - Ref #: progressive patient number; Age: age of patient at time of baseline scan; Pre-treatment cancer size: maximum tumor dimension pretreatment (one column reports the dimension from MRI or full-field digital mammography, one column reports the size of the tumor ROI from optical mammography), "Inflam" denotes inflammatory breast cancer; Cancer stage: initial clinical cancer stage; Cancer subtype: triple-negative breast cancer (TNBC), estrogen-receptor-positive/progesterone-receptor-negative (ER+/HER2-), and HER2+; Chemotherapy agent: chemotherapy drugs administered to patient; Infusion frequency (total number): how often infusions were performed (and total number of infusions); Duration of treatment: how long the patients underwent treatment (including breaks in therapy schedule); Post-treatment cancer size (Hist.): maximum tumor dimension post treatment from histology after surgical resection; Response level: individual patient's response (R: responder showing either a pathologic complete response (pCR) [no remaining tumor] or partial response 1 (PR1) [tumor decreased by more than 50% in size]; NR: non-responder showing partial response 2 (PR2) [tumor decreased by less than 50% in size]).

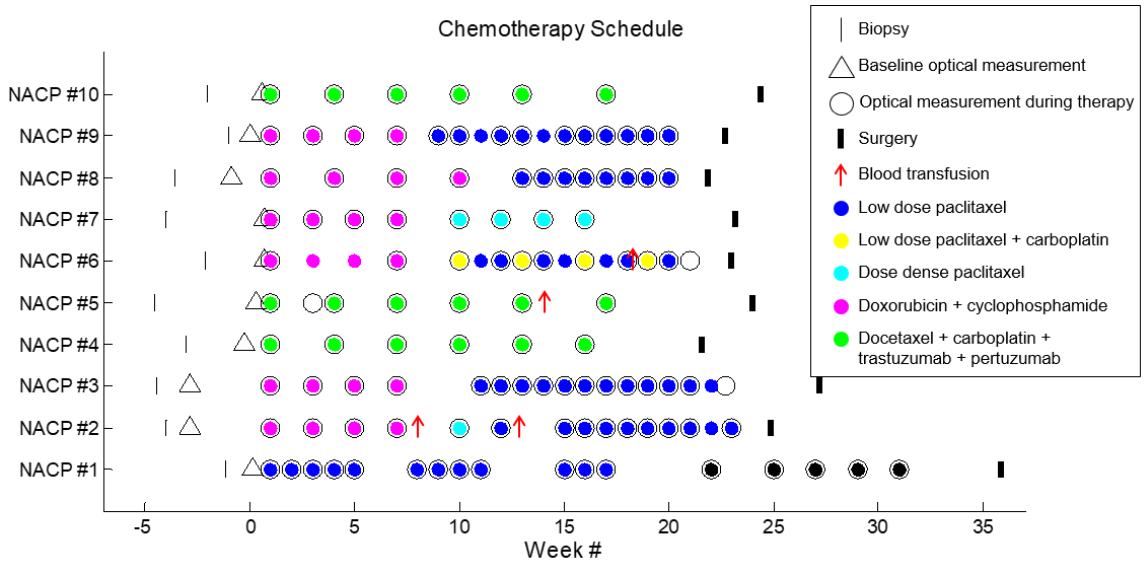

Figure 3.1: Patients chemotherapy schedules. Week one corresponds to the first infusion time point. The times of biopsy, infusions, surgery, and blood transfusions are indicated for all ten patients. The type of drug administered is also indicated by the color within the chemotherapy infusion open circles. The baseline optical mammograms (open triangles) were obtained 2–27 days before the treatment began. The overlapping baseline optical mammogram point and first infusion point for NACP # 6, 7, and 10 indicate that these occurred 2 days within one another.

A continuous-wave optical mammography instrument was used to image the patients receiving neoadjuvant chemotherapy. This instrument is described in detail in our previous work[8]. Note that this instrument is a previous generation of the instrument described in Chapter 2:. Namely, it lacks the capability to resolve depth of optical inclusions, as well as has a lower spectral bandwidth and sensitivity. The main features of this instrument are described here. Either a xenon arc lamp (Model No. 6258; Newport Corporation, Irvine, CA, for NACP ## 1–5) or a quartz tungsten halogen lamp (Model No. 66997; Newport Corporation, Irvine, CA, for NACP ## 6–10) served as the light source, with its optical emission spectrally filtered to pass the wavelength range 500 – 1,000 nm. An illumination optical fiber and a collection optical fiber scan collinearly in transmission geometry over two parallel polycarbonate plates that mildly compress the breast. The

detected light is spectrally dispersed by a spectrograph (Model No. SP-150; Princeton Instruments, Acton, MA) and measured by a cooled charge-coupled device (CCD) camera (Model No. DU420A-BR_DD; Andor Technology, South Windsor, CT). Transmission optical data through the breast were acquired spatially every 2 mm in the *x* and *y* directions and with a wavelength resolution of 8 nm over the spectral band of 650–850 nm. The time to scan one breast for each patient ranged from 3–10 min (average: 6 min) based on breast size. Each measurement session, including setup time and optical imaging of both breasts took 15–30 min.

3.2.2. Lab parameters and response categories

A complete blood count was obtained for every patient before each chemotherapy infusion and the hemoglobin concentration in blood (denoted at Hgb) was recorded. Since [HbT], the concentration of hemoglobin in tissue, is equal to the product of Hgb times the blood volume (i.e. the blood-to-tissue volume fraction), the Hgb data were used to translate [HbT] changes into blood volume changes. Specifically, the relative change in blood volume is given, to a good approximation, by the relative change in [HbT] minus the relative change in Hgb. This approach is important to separate the systemic effects of varying Hgb from the local effects of varying tissue vascularization on the measured [HbT] changes [54]. The relative blood volume change with respect to the first chemotherapy infusion was determined for each patient throughout the course of treatment.

The response categories used in this work were determined from the tumor size pre-treatment (with imaging) and post-treatment (from the pathology report based on histology following surgical excision/mastectomy). The two response categories are as follows:

1) Responders (R): Under this category, we include those patients who show a pathologic complete response (pCR) or a partial response 1 (PR1) (defined as any remaining tumor that had decreased by more than 50% in the maximum dimension, regardless of nodal status). The patients in the pCR and PR1 categories are both considered to be associated with an improved prognosis and thus were grouped together in the R category.

2) Non-responders (NR): Under this category, we include those patients who show a partial response 2 (PR2) (defined as any tumor that decreased by less than 50% in the maximum dimension, regardless of nodal status). This categorization, in agreement with Roblyer *et al*. [64], considers that patients whose tumor size decreased by less than 50% may have a less favorable prognosis.

From a clinical point of view, it is desirable to identify poorly responding tumors early in the NAC treatment period to help make changes to treatment protocols and maximize the therapeutic effects. Accordingly, we aim to identify R and NR patients during therapy based on optically measured parameters over the course of NAC.

It is worth pointing out that some ambiguity exists in the identification of responders and non-responders. First, the choice of 50% as the minimum reduction in tumor size for responders is somewhat arbitrary. Second, a classification solely based on tumor size may not properly take into account microscopic responses at the cellular level, as done by the five-point, Miller-Payne histological grading system[83]. This cellularity-based grading system of pathologic response (ranging from 1: no response, to 5: complete pathologic response) was used in some optical studies. However, even this method leads to some ambiguity, as shown by different groupings of the Miller-Payne grades. Zhu et al.

considered grades 1 – 3 for non-responders and partial responders, and grades 4 – 5 for near-complete and complete responders[71]. By contrast, Schaafsma et al. considered grade 1 for non-responder and grades 2 – 5 for (partial) responders[74]. In some cases, criteria based on residual tumor size and decrease in cellularity were combined in the categorization of complete response, good pathologic response, or minimal pathologic response. A breast response index for continuous-scale assessment of NAC response (from 0: "no response" to 1: "pCR of both breast and axilla") was also introduced on the basis of a change in T stage before and after treatment[84]. Ultimately, the goal of any assessment tool of clinical response is to identify, as early as possible in the course of NAC treatment, those patients who will have a poor clinical outcome with the ongoing treatment regimen. The classification considered by us achieves this goal because the NR patients, as defined above, are those who have a less favorable prognosis, and for which a change in treatment may be beneficial. On the other hand, although the goal of pCR is always desired, a partial response which is close to pCR is also favorable, and thus both categories were considered as R patients.

3.2.3. Data Processing

A continuous-wave optical diffusion model for a homogeneous, infinite slab geometry was used to process the optical transmission spectra in the wavelength range 650 – 850 nm[20] and further details on the model implementation can be found in prior work[8]. Briefly, the model inputs at each pixel were the measured transmittance spectrum (over the full wavelength band 650 – 850 nm) and an estimate of the tissue thickness[85]. An inversion procedure based on the Levenberg-Marquardt method[86] was applied to directly recover the concentrations of HbO_2, Hb, water, and lipids by utilizing their known extinction spectra[52].

Since only continuous-wave light was used, the scattering properties were not measured and were set in order to recover unique chromophore concentrations[37]. There have been a few studies that measured scattering properties, and mixed results have been reported on the scattering contrast featured by breast cancer[9]. Therefore, the scattering amplitude and power ($\mu_s'(\lambda_0)$ and b, which represent the magnitude and the wavelength dependence of scattering, respectively) were fixed to values derived from results in the literature ($\mu_s'(\lambda_0 = 670\ \text{nm}) = 10.5\ \text{cm}^{-1}$, $b = 1$)[87]. Two additional optical parameters being reported in this study are total hemoglobin concentration ([HbT]) and hemoglobin saturation (SO_2). Hemoglobin saturation is the ratio of [HbO_2] to [HbT], a quantity representative of the balance between oxygen supply and the oxidative metabolic rate in tissue.

The initial tumor location was identified in the cranio-caudal view X-ray mammogram, and a rectangular region including the tumor location was considered in the baseline [Hb] optical mammogram. The tumor region of interest (ROI) was defined as the collection of pixels within the rectangular region having [Hb] values greater than 75% of the maximum [Hb] value within the rectangular region[8]. We found that the specific threshold value (75% in this study) used to define the tumor ROI does not have a significant impact on the results reported in this manuscript. The placement and size of the tumor ROI was kept consistent for all sequential optical mammograms, by maintaining the distance of the ROI from the proximal and lateral edges of the breast. For each measurement session over the course of neoadjuvant chemotherapy, we compute the value of the optical parameters at the tumor ROI and the associated errors as the average and standard deviation, respectively, over all the pixels within the tumor ROI defined above.

Due to the homogenous tissue model being applied in this work, we observe that the recovered chromophore concentrations in the cancerous region represent contributions from both the tumor and healthy surrounding tissue. Since the tumors of NAC patients are typically large, the tissue being measured within the tumor ROI is mostly representative of cancerous tissue at baseline and at the start of treatment. However, if the patient responds to the treatment and the tumor shrinks, healthy tissue will contribute more and more to our optical measurements in the tumor ROI during the course of neoadjuvant chemotherapy. This is an important aspect to keep in mind for the interpretation of our results.

Two cases, NACP #1 and NACP #10, had to be discarded for technical reasons, since their tumor ROIs fell outside of the optical field of view in a number of imaging sessions as a result of the tumor proximity to the chest wall. We point out that even though the tumor sizes determined by MRI and X-ray mammography are quite large (9.4 cm for NACP #1, 4.5 cm for NACP #10), the size of the tumor ROI identified in the optical mammograms, on the basis of the optical contrast provided by [Hb], is significantly smaller (1.2 cm for NACP #1, 1.9 cm for NACP #10).

The [H_2O] and [lipid] data were found to not provide reliable longitudinal results, which is likely attributed to the spectral range of 650 – 850 nm not being highly sensitive to those chromophores. Specifically, we found that there was a lack of a consistent trend (decreasing or increasing) in the percent change of [H_2O] and [lipid] from the baseline measurement for most patients. The frequency of the optical mammograms throughout the duration of therapy allows us to assess the variance and reliability of the observed trends in the optical parameters during neoadjuvant therapy.

3.2.4. Statistical analysis

Because of the relatively small number of patients analyzed in this study (8 of the 10 enrolled patients), we used a non-parametric Wilcoxon rank-sum test (with $p<0.05$ to indicate significance) to determine when responders (R) could be discriminated from non-responders (NR) on the basis of optical parameters at the tumor ROI. The statistical analysis was performed with MATLAB (Mathworks, Natick, MA). Grouping together pCR and PR1 patients into the R category is in line with the primary goal of this work, which is to evaluate whether and when NR can be distinguished from R. However, further stratifying R into pCR and PR1 may be beneficial for better assessing those patients in need of treatment changes, and this option will be considered in future studies on larger patient populations.

3.3. Results

3.3.1. Patient Measurements

Representative breast images for a R (pCR) patient (NACP #5) are shown in Figure 3.2, which shows the full-field digital mammogram, the axial contrast-enhanced subtraction MRI image and the optical maps of [HbT] and SO_2 throughout NAC treatment. The outer 1 cm of the breast map is cut in the optical images due to the confounding contributions of edge effects in the optical data collected in the proximity of the breast edge. The rectangular region containing the tumor is shown in the X-ray image. The corresponding area is also shown in the optical mammograms at week 0 (dotted line) together with the tumor ROI (solid line) obtained from the [Hb] map as described in the methods section.

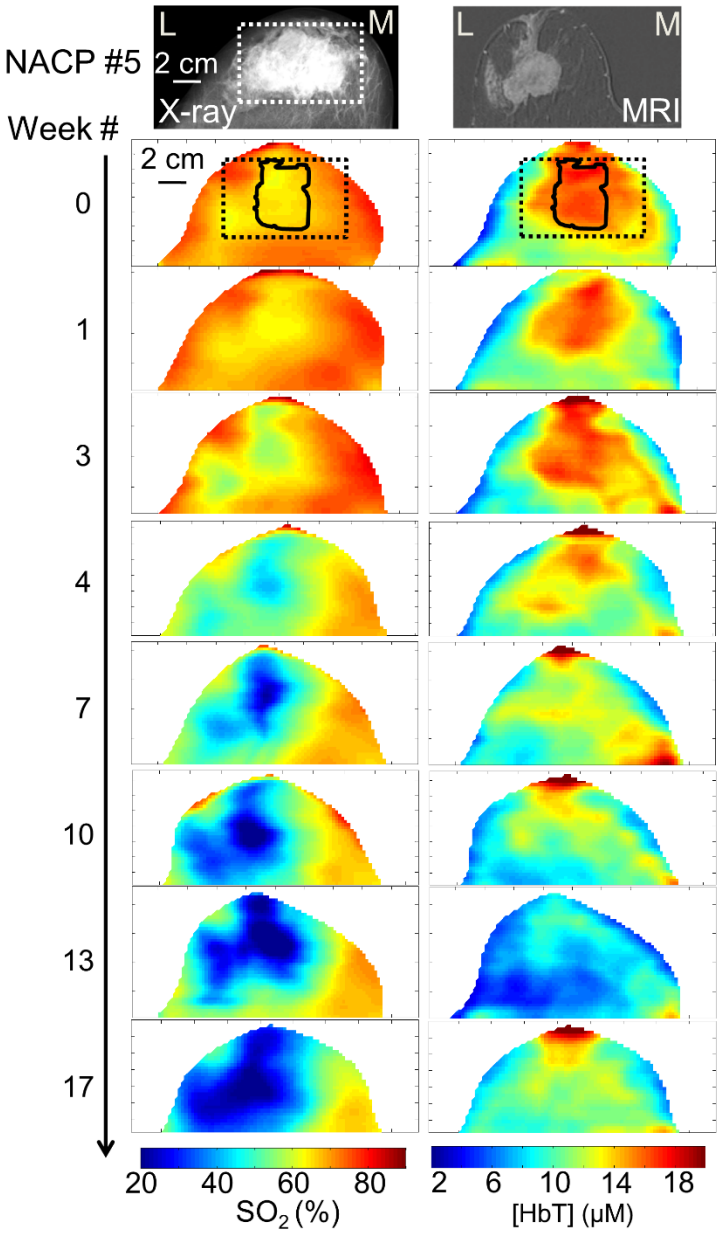

Figure 3.2: Left breast images for NACP #5, an R (pCR) patient. In all images, the left side of each image is lateral (L) and the right side of each image is medial (M). The craniocaudal full-field digital mammogram (top left) depicts an irregular, partially spiculated mass (white box) located in the left breast corresponding to the patient's biopsy-proven malignancy, prior to treatment. The MRI axial contrast-enhanced subtraction image (top right) demonstrates a 4.4 cm irregular mass with additional areas of non-mass enhancement extending to the nipple and laterally. The optical [HbT] and SO_2 maps obtained throughout NAC show the progressive decrease of [HbT] and SO_2 at the cancerous region (identified at week 0 by the solid line within the dashed rectangle corresponding to the location of the mass visible in the X-ray image). Subsequent surgical specimen (not shown) revealed a pCR.

The decrease in [HbT] and SO_2 throughout the course of chemotherapy within the tumor ROI is apparent in Figure 3.2. The decrease in [HbT] at the tumor ROI during treatment is expected for a responder, since breast cancer has a greater [HbT] than surrounding healthy tissue[9,29,88]. However, the decrease in SO_2 at the tumor ROI may be somewhat surprising, especially considering our previous report of a lower SO_2 in breast cancer compared to healthy tissue[8]. As we will further discuss in the discussion section, a longitudinal study during NAC treatment must take into proper consideration the systemic effects of therapy.

We computed the mean value and standard error of the percent change from the baseline measurement (i.e. from before the start of NAC) for [Hb], [HbO_2], [HbT], and SO_2 at the tumor region of interest for each response group. The average percent changes over five binned temporal windows in the normalized time axis (defined in the materials and methods section) are reported in Table 3.2, which shows the response category in the first column, the five binned temporal windows in the second column, and the response to therapy at the tumor ROI in the third to sixth columns. From the definitions of [HbT] ([Hb]+[HbO_2]) and SO_2 ([HbO_2]/[HbT]), it follows that the relative change in [HbT] is a weighted average of the relative changes in [HbO_2] and [Hb] with weights given by the baseline values of SO_2 and $(1-SO_2)$, respectively. Each bin is identified by the center point of its time interval (10%, 30%, 50%, 70%, or 90%) and the bounds of each bin are shown. The single parenthesis indicates the percentage therapy complete that is not included in the bin, whereas the bracket represents the percentage point that is included in the bin. Given

the duration of NAC in this study (18 – 22 weeks), the 10% bin corresponds to approximately the first 4 weeks of treatment.

Table 3.2: Summary of the means and standard errors of relative changes in [Hb], [HbO_2], [HbT], and SO_2 at the tumor region of interest from baseline over 5 binned time windows for each response category. Beneath the response category, the number of patients in each group (*n*) is also provided.

		Response to therapy at the tumor ROI (% change from baseline)			
Group	Percent therapy complete	[Hb]	[HbO_2]	[HbT]	SO_2
Responders (*n* = 6)	10 (0, 20]	−2 ± 8	−6 ± 7	−5 ± 7	−2 ± 1
	30 (20, 40]	−13 ± 7	−36 ± 6	−28 ± 6	−12 ± 3
	50 (40, 60]	−4 ± 5	−52 ± 5	−35 ± 4	−27 ± 4
	70 (60, 80]	−4 ± 6	−56 ± 5	−38 ± 4	−32 ± 4
	90 (80, 100]	4 ± 7	−52 ± 4	−36 ± 4	−26 ± 4
Non-responders (*n* = 2)	10 (0, 20]	−9 ± 7	−9 ± 7	−9 ± 7	0 ± 1
	30 (20, 40]	1 ± 4	−5 ± 4	−3 ± 4	−2 ± 0
	50 (40, 60]	1 ± 5	−3 ± 1	−2 ± 2	−1 ± 1
	70 (60, 80]	0 ± 11	−15 ± 12	−10 ± 12	−6 ± 2
	90 (80, 100]	23 ± 12	3 ± 15	10 ± 14	−8 ± 3

Group results and the individual patient data of the percent change from baseline for the [HbT] in the tumor ROI are shown in Figure 3.3. Figure 3.3 shows a decreasing [HbT] in R's compared to a relatively constant [HbT] in NR's. To translate these changes in hemoglobin concentration into changes in blood volume fraction, one needs to take into

account the fact that the hematocrit, thus the hemoglobin concentration in blood, is also affected by NAC.

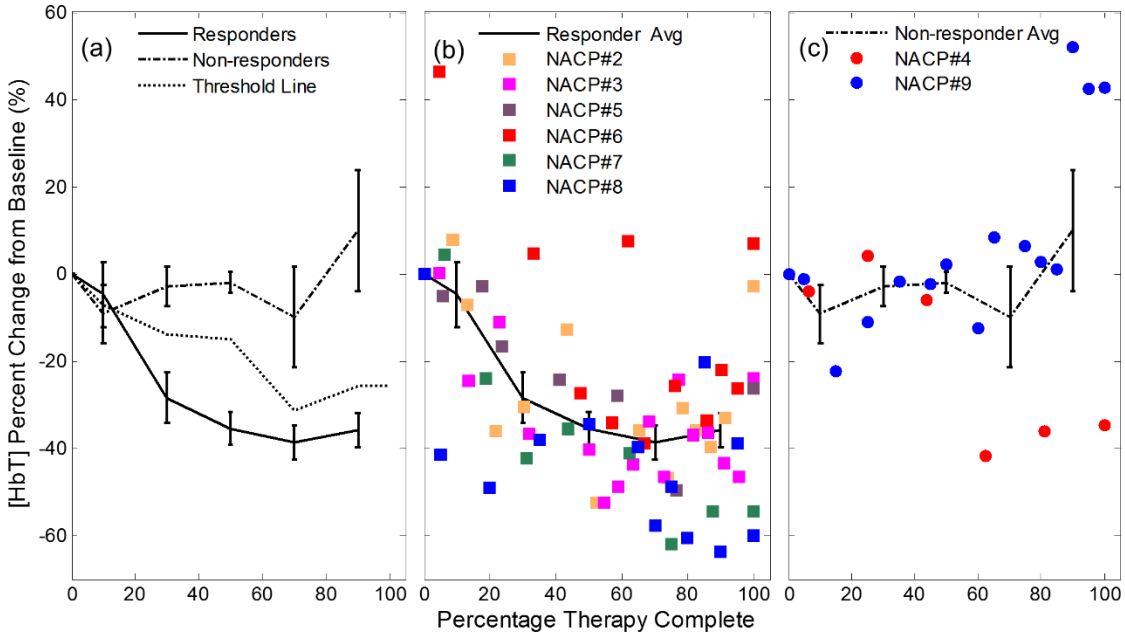

Figure 3.3: (a) Trends of [HbT] at the tumor ROI for both response categories at a group level (the error bars represent the standard error). The threshold dashed line represents the weighted average of the mean percent changes of [HbT] for the R and NR groups using the inverse of the standard error as the weights.. This line is used for assessing patient response and is discussed in relation to the cumulative response index. The individual patient data throughout therapy are shown in (b) for responders and (c) for non-responders, along with the corresponding group average line.

The average relative change throughout treatment in [HbT], hemoglobin concentration in blood, and blood volume fraction for both breasts for all eight patients is shown in Figure 3.4. It is apparent from Figure 3.4 that, during NAC, the concentration of hemoglobin in blood (Hgb) decreases in all patients, both R's and NR's suggesting a systemic response to treatment by all subjects. By calibrating the [HbT] changes by the Hgb changes, it can be seen that blood volume features an initial decrease after the start of NAC and then stays relatively constant in patients classified as R, whereas it increases in

patients classified as NR. Whereas for the healthy breast both R and NR patients respond similarly for [HbT] and BV.

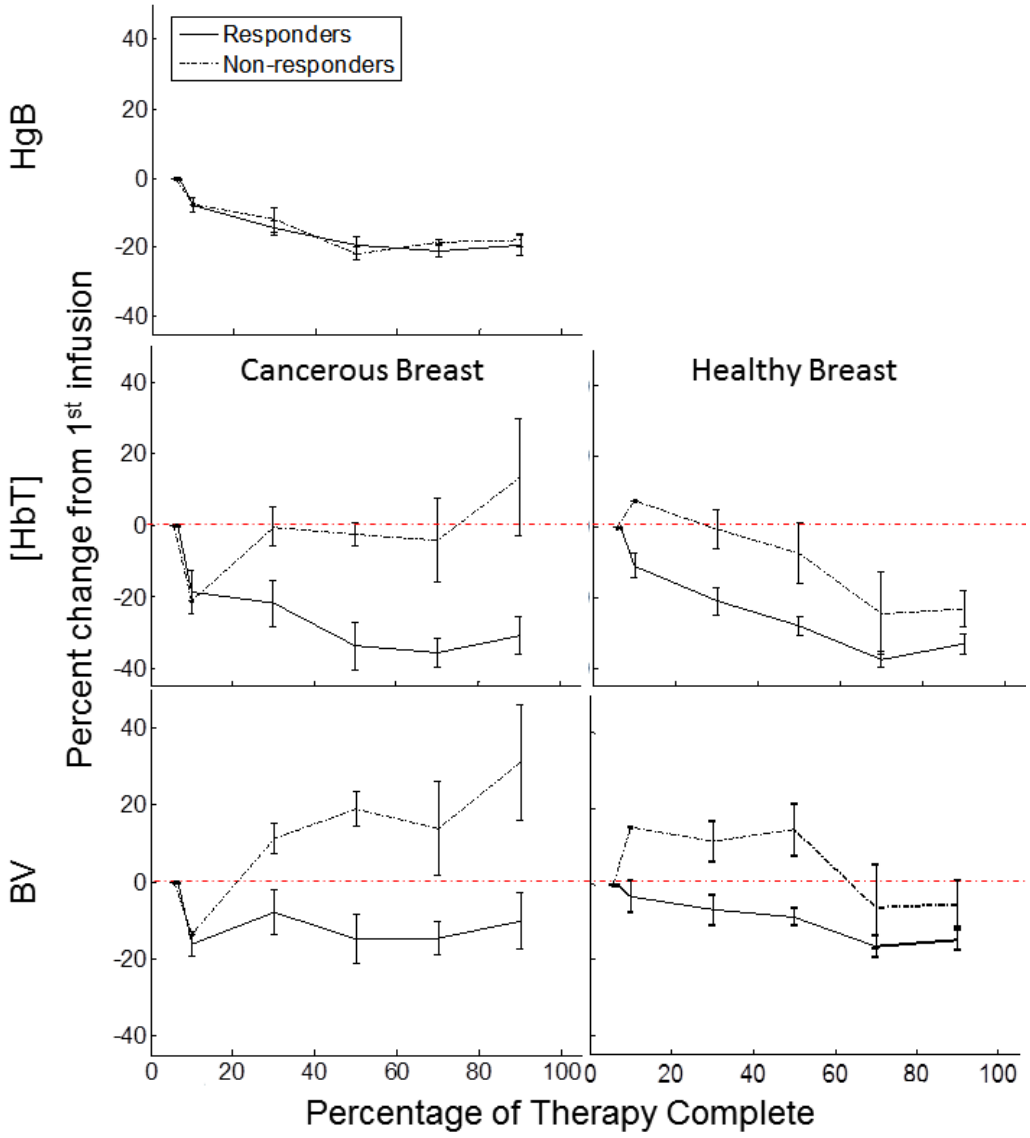

Figure 3.4: Average change in blood volume, [HbT], and hemoglobin concentration in blood (Hgb) relative to the first infusion throughout chemotherapy for responders and non-responders in the cancerous and healthy breast. All patients show a similar systemic decrease in Hgb during NAC, but blood volume fraction in breast tissue decreases in responders and increases in non-responders. In the healthy breast [HbT] decreases and BV remains constant.

To provide an indication of how perfusion and metabolic demand may be altered in cancerous breasts with varying levels of response, the tumor region SO_2 changes are shown on a group level and for each individual patient in Figure 3.5. Figure 3.5 conveys that the SO_2 decrease in the cancerous region scales with the level of response, with responding patients featuring a larger SO_2 decrease compared to the non-responding patients.

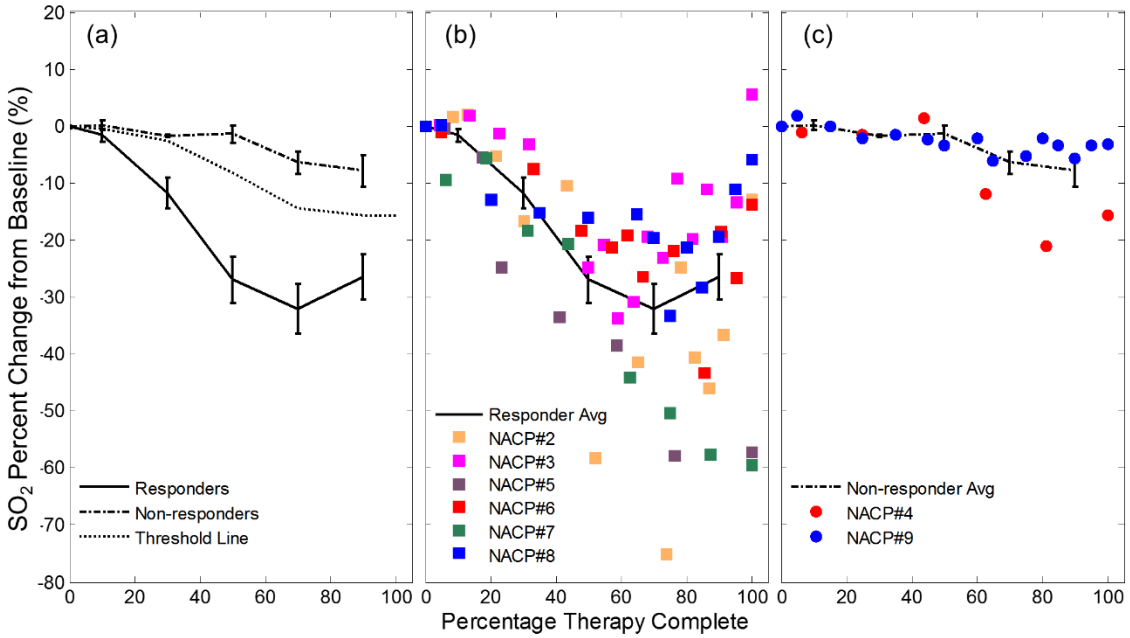

Figure 3.5: (a) Trends of SO_2 at the tumor ROI for both response categories at a group level (the error bars represent the standard error). The threshold dashed line represents the weighted average of the mean percent changes of SO_2 for the R and NR groups using the inverse of the standard error as the weights. This line is used for assessing patient response and is discussed in relation to the cumulative response index. The individual patient data throughout therapy are shown in (b) for responders and (c) for non-responders, along with the corresponding group average line.

A non-parametric Wilcoxon rank-sum test was applied at all considered therapy complete time windows to determine if there was a significant difference between the observed changes in the [Hb], [HbO_2], [HbT], and SO_2 of the tumor ROIs for responding and non-responding patients. The *p* values for this statistical test are reported in Table 3.3

and show that [HbO_2], [HbT], and SO_2 achieve a statistically significant discrimination ($p \leq 0.05$) of the R and NR groups at therapy midpoint and beyond. A p value of 0.06, marginally greater than the significance level, was observed at the 20 – 40% therapy complete window for [HbO_2], [HbT], and SO_2.

Table 3.3: Predictive values of the NAC response assessment based on changes from baseline (p values) and CRI (sensitivity and specificity) from [HbT], SO_2, [Hb], and [HbO_2] measurements at the tumor ROI for each time bin.

% Therapy Complete	% Change from Baseline				Cumulative Response Index (CRI)			
	[HbT]	SO_2	[Hb]	[HbO_2]	[HbT]	SO_2	[Hb]	[HbO_2]
	p value	p value	p value	p value	Sens/Spec	Sens/Spec	Sens/Spec	Sens/Spec
10 (0, 20]	0.9	0.8	0.6	1	0.33/1	0.5/0.5	0.33/0.5	0.5/0.5
30 (20, 40]	0.06	0.06	0.2	0.06	0.67/0.5	0.83/1	0.67/0.5	0.83/1
50 (40, 60]	0.01	0.01	0.46	0.01	0.83/1	1/1	0.67/0	0.83/1
70 (60, 80]	0.05	0.002	0.6	0.02	0.83/1	1/1	0.67/0.5	1/1
90 (80, 100]	0.01	0.01	0.14	0.004	1/0.5	1/1	0.5/0.5	1/1

3.3.2. Cumulative Response Index

In an effort to move beyond a group analysis to assess individual patient response to NAC, we introduce a cumulative response index (CRI) at a single patient level. This CRI is calculated at each therapy session on the basis of the optical mammograms recorded at that session and all previous sessions, and thus it takes advantage of the cumulative information collected with optical mammography during the course of treatment. The CRI serves as an individual indicator for how the patient is responding and can take values between -1 (no response) and +1 (complete response). The CRI can be defined for any measured parameters of the tumor ROI ([Hb], [HbO_2], [HbT], SO_2, etc.). Here, to illustrate the CRI concept, we define the CRI in terms of SO_2. To start, we compute a threshold value for

therapy response at each % therapy complete time window by taking the weighted average of the mean percent change of SO_2 for the R and NR group results, with weights given by the inverse of the standard error. In the case of SO_2, the R group and NR group results are reported in Figure 3.5 by the solid line and dashed line, respectively. Then, a linear interpolation is performed to create an SO_2 threshold line over the entire therapy period. This threshold line is taken to represent the boundary that separates SO_2 changes in responding and non-responding tumors. For each measurement session *i*, one can compute the difference d_i, as the threshold value of SO_2 minus the percent change of SO_2 at that particular time point (percentage of therapy complete). The standard deviation associated with d_i is denoted as $\sigma(d_i)$ and refers to the standard deviation across all pixels within the tumor ROI for the *i*-th imaging session. Subsequently, the CRI at the *n*-th session is defined as follows:

$$\mathrm{CRI}(n) = \frac{\sum_{i=1}^{n} \frac{d_i}{\sigma(d_i)}}{\sum_{i=1}^{n} \frac{|d_i|}{\sigma(d_i)}} \tag{3.1}$$

The normalization factor in the denominator of the right-hand-side of Eq. (3.1) limits the CRI values to the range [-1, +1]. When the SO_2 at a tumor ROI falls above the threshold line, its contribution to the CRI is negative, whereas when it falls below the threshold line its contribution to the CRI is positive. Therefore, positive CRI values are associated with responders, and negative CRI values are associated with non-responders.

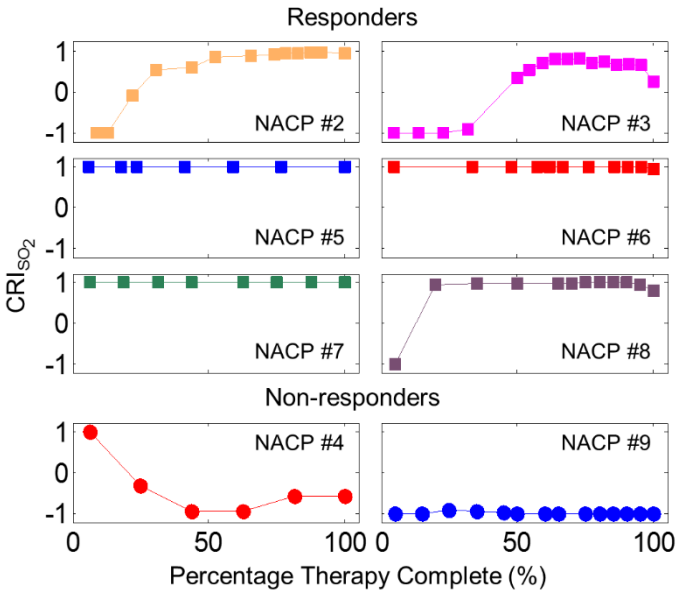

Figure 3.6: Cumulative response index (CRI), based on SO_2 at the tumor ROI, for each individual patient throughout the course of neoadjuvant chemotherapy. The CRI can take values between -1 (poor response) and +1 (good response).

The SO_2 cumulative response index was found for each patient. Figure 3.6 shows each patient's SO_2 CRI, and Table 3.3 reports the sensitivity and specificity for response classification achieved at different time points during therapy using the CRI associated with [Hb], [HbO_2], [HbT], or SO_2. The sensitivity and specificity were calculated by considering positive and negative values of the CRIs to represent R and NR, respectively (in other words, we have considered a threshold value of 0 to categorize R (positive CRI) and NR (negative CRI)). Of course, one may chose a different CRI threshold value or define a different threshold line during the course of treatment, and build a receiver operating characteristic (ROC) curve. However, given the limited patient population, the point of this study is to illustrate our proposed approach to the assessment of individual response to neoadjuvant therapy, a point that is made by the results reported in Figure 3.6 and Table 3.3.

Table 3.3 shows that the SO_2 CRI achieved the best NAC assessment results, with sensitivity/specificity of 83%/100% after 20% therapy complete, and 100%/100% after 40% therapy complete. Comparable results were achieved with [HbO_2] and [HbT], but they were marginally worse than the SO_2 results in this study.

3.4. Discussion

3.4.1. [HbT] response to neoadjuvant chemotherapy at the tumor ROI

A consistent result reported in the literature is the decrease of [HbT] at the tumor location during the course of NAC for patients who respond to therapy. In partial responders or non-responders, the tumor [HbT] was found to decrease by a smaller amount than in responders, or to remain either constant or increase slightly during NAC. Specifically, within the first four weeks of NAC, studies that included both responders and non-responders found that the [HbT] at the tumor location decreased by as much as 60%[65,71,72,74,75,77,78], whereas non-responders (or partial responders) showed a lesser decrease[73], no change[65,71,75,78], or an increase[72,74,77] in [HbT] at the tumor location. In this study, we confirmed this result, having observed a reduction in [HbT] of about 30% in the tumor ROI for responding patients as opposed to a non-significant change in non-responding patients in the course of therapy (starting at 20% of therapy, i.e. about 4 weeks into NAC) (see Table 3.2).

Changes in tissue [HbT] are the result of either or both of two factors: a change in tissue vascularization (i.e. in the blood volume ratio) or a change in the concentration of hemoglobin in blood (i.e. in hematocrit). On the basis of Figure 3.4, our results in responders are assigned to a combination of both factors - a reduction (by about 15%) in the tumor vascular density, which has been previously reported[75], and a systemic decrease (by about 20%) in the hemoglobin concentration in blood (Hgb), resulting from NAC[89].

Because a comparable systemic decrease in Hgb was observed in responders and non-responders, our [HbT] results indicate that the tumors in non-responders feature an increased vascularization during the course of NAC (see Figure 3.4).

It is important to note that, in the case of patients who respond well to treatment, the tumor ROI contains more and more non-cancerous tissue during the course of treatment. Therefore, the decrease in [HbT] observed during NAC in responding patients represents NAC-induced changes in cancerous tissue (early in NAC) as well as in healthy tissue (later in NAC). By contrast, in the case of non-responders, for whom the tumor ROI always contains a significant amount of cancerous tissue, the [HbT] evolution during NAC is mostly representative of changes in cancerous tissue.

Because of the systemic effects of NAC as a result of the systemic decrease in Hgb, one would expect a systemic decrease in [HbT] throughout the body, and in particular in the contralateral, healthy breast (as also reported in [54,64,90]). We similarly observed a reduction in [HbT] in the contralateral, healthy breast, to a different extent in responders and non-responders, suggesting that systemic effects of NAC in peripheral tissue may also be indicative of the level of therapeutic response.

3.4.2. SO_2 response to neoadjuvant chemotherapy at the tumor ROI

It is somewhat surprising that among all the published studies only a few have reported results of the evolution of tumor SO_2 during the course of NAC. For example, the two pioneering case studies reported a tumor-to-normal SO_2 ratio of about 0.9 throughout NAC with an increase to 1.4 after the end of NAC[54] and a decrease in the tumor SO_2 after the 5th NAC cycle from ~81% to ~60%[63]. Alternatively, groups have reported that elevated levels of baseline SO_2 may be a good indicator of chemotherapy response.[79,91] In part, this paucity

of SO_2 data in optical NAC studies may be due to the fact that an inconsistency in NIRS investigations remains regarding how SO_2 in breast cancer compares to SO_2 in healthy tissue. Some studies have reported that the increased metabolic demand from tumor tissue results in an observed decrease in SO_2 within tumors.[4,23] Whereas others have found no significant difference in the SO_2 of cancerous and healthy tissue.[29,87,92,93] In these cases it is possible that SO_2 may be comparable to (or even greater than) that of healthy tissue when the oxygen supply exceeds the oxidative metabolic needs of the tumor because of increased blood flow. Additionally, the selection of the reference tissue as the healthy control to which the tumor region is compared against is not consistent across studies. Depending on the tumor size and the heterogeneity of the healthy tissue, the choice of reference area may impact the level of SO_2 contrast.[8] Previously, we reported a decrease in SO_2 in the tumor region with respect to the surrounding healthy tissue, and use the same analysis methods for the data acquired for each imaging session presented here.[8]

Based on our previous results, one would expect that due to chemotherapy response when tumor tissue is replaced with healthy tissue an increase in SO_2 over time would be observed. However, as noted at the end of the previous section, the combination of systemic and local effects of NAC may introduce new physiological and metabolic processes that differentiate responders and non-responders. In fact, in this study we found that the oxygen saturation of hemoglobin at the tumor ROI was the quantity most strongly associated with the level of patient response to neoadjuvant chemotherapy. Surprisingly, at the tumor ROI, we observed a stronger *decrease* of SO_2 in responders (about −10% at 20 – 40% therapy complete, and about −30% throughout the rest of NAC) than in non-responders (a decrease of a few percent, significant only toward the end of NAC) (see Table 3.2). Furthermore,

the SO_2 CRI achieved the best sensitivity and specificity for patient response assessment (see Table 3.3).

The physiological sources of decrease in tissue SO_2 are: (1) a decrease in tissue vascularization, associated with a regression of angiogenesis, (2) a decrease in blood flow, which reflects the local gradient in blood pressure as well as the compliance, reactivity (dilation/constriction), and architecture of the vasculature, and (3) an increase in the tissue metabolic rate of oxygen which relates to cellular metabolism. While breast cancer is typically associated with angiogenesis, perturbations to cellular metabolism and tissue perfusion, the specific angiogenic, metabolic, and perfusion responses to chemotherapy are not fully understood or characterized.

From a technical point of view, optical measurements of SO_2 are typically found to be robust since they rely on assessing concentration ratios ($[HbO_2]/[HbT]$) rather than absolute concentrations. To test the qualitative accuracy of our homogeneous tissue model approach, we have generated forward data for an inhomogeneous medium using a perturbation approach in diffusion theory.[94] When we set the SO_2 of the localized perturbation to be either lower or higher than that of the background medium, the recovered SO_2 value (using the homogeneous tissue model reported here) is always qualitatively correct, i.e. it accurately reflects the direction (higher or lower) of the localized SO_2 change from the background.

Results obtained using PET/CT techniques indicate a decrease in cellular metabolism when tumors respond to treatment due to the reduction in the absolute number of cancerous cells and in their proliferative activity.[61,95] These results may appear to contradict our findings of decreasing SO_2 in responders. However, one needs to recall that

cellular metabolism is only one factor affecting the hemoglobin saturation within the tumor location. Tissue perfusion is another critical factor, as it affects the rate of oxygen delivery to tissue. Using contrast enhanced MRI or [^{15}O]-water PET imaging, responding tumors have been found to show a significantly stronger decrease in perfusion compared to poorer responding tumors[96–99]. Therefore, our finding of a greater decrease of SO_2 in the tumor ROI of responding patients is consistent with a dominant effect of the reduction in blood flow vs. the reduction in cellular metabolism.

We stress again that chemotherapy is not a localized treatment, and it will also impact the healthy tissue being measured in the optical mammograms. The direction of the response in the SO_2 of cancerous and healthy tissue depends on the relative magnitude of the changes in blood flow, oxygen consumption, and blood volume during treatment. The chemotherapy effects on the SO_2 of healthy tissue were observed in the contralateral, healthy breast, which showed stronger decreases (~45% in responders, and ~15% in non-responders, after midpoint) than the tumor ROI in the cancerous breast.

This finding provides insight into how the healthy tissue responds to chemotherapy, and it explains the apparent inconsistency between the observed decrease of SO_2 in the tumor ROI of responders, and the previously reported lower SO_2 of cancerous tissue with respect to the surrounding healthy tissue (by $-5 \pm 1\%$)[8]. In fact, one should expect responding tumors to feature an SO_2 value that approaches the SO_2 value of healthy tissue. In the absence of any systemic effects, this means that responding tumors should feature an *increase* in SO_2 during the course of NAC. However, in the presence of systemic effects that lower the SO_2 of healthy tissue to levels below the baseline SO_2 of cancerous tissue, responding tumors should indeed feature a *decrease* in SO_2. In fact, these systemic effects

are observable in the healthy breast and are also capable of discriminating responders and non-responders but are less effective than when considering changes in the cancerous breast (Figure 3.7).

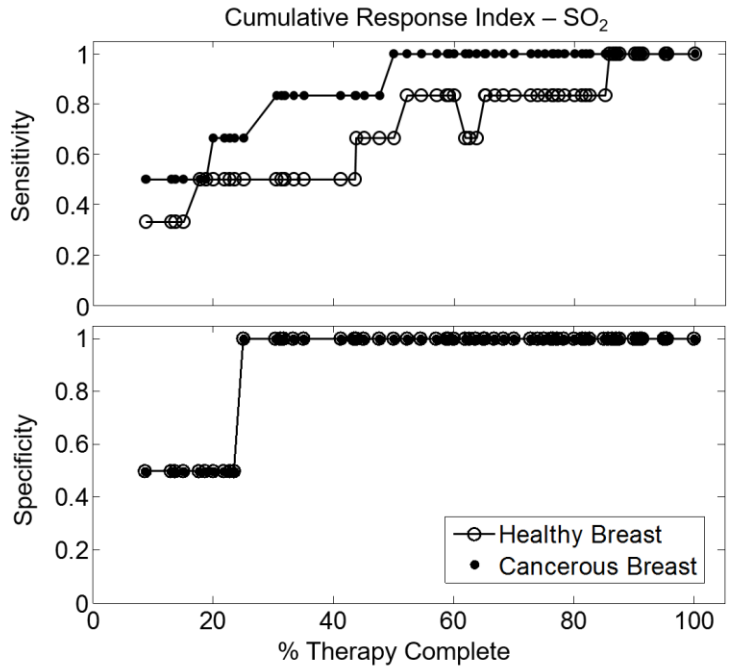

Figure 3.7: Sensitivity (top panel) and specificity (bottom panel) for identification of responders and non-responders on the basis of the SO2 CRI for the cancerous breast (filled circles) and the healthy breast (open circles).

Furthermore, such decrease should be lower than that of healthy tissue, simply because of the lower baseline value of SO_2 in cancerous vs. healthy tissue. This is what we observed in our study and shows the importance of systemic effects of NAC in the interpretation of optical mammography data. Systemic effects of neoadjuvant chemotherapy should also be taken into account when considering tumor-to-normal (T/N) ratios, and whether the choice for a reference tissue should be a tissue area in the cancerous breast or in the contralateral breast.

3.4.3. Limitations of the study and future directions

The results reported in this work are limited by the small sample size of patients that we were able to enroll in the study. Because of the small sample size, the cumulative response

index (CRI) was calculated on the basis of a threshold line computed from data collected on the same patients that were then classified with this method. In a larger study, the robustness of this method would be tested by only using a subset of the patient data to generate the criteria used to classify the rest of the patients. However, the results reported here do show the potential of optical mammography to discriminate responders and non-responders on an individual basis during the NAC regimen.

The limited statistical significance achievable with a small sample size is further exacerbated by the heterogeneous patient population, in terms of both the prescribed chemotherapy agents and the NAC duration and infusion frequency. However, we observe that optical mammography is sensitive to the end result of vascular, hemodynamic, and metabolic perturbations, regardless of the biological mechanisms that are responsible for them. Furthermore, the relatively large number of optical measurements reported in this study throughout treatment (ranging from a minimum of 7 to a maximum of 18, mean number: 12) shows their robustness as reflected by their progressive trends during NAC. Of course, optical mammograms can in principle be performed on a regular weekly or biweekly schedule, independent of the NAC infusion schedule, thus providing a more regular and temporally refined monitoring of NAC response.

A key assumption of our approach is that the optical scattering properties of tissue are kept constant. This means that any changes in tissue scattering that may occur during chemotherapy are not considered. To test how changes in the scattering properties may impact the recovered chromophore concentrations and their corresponding trends throughout treatment, NACP #5 data at baseline, midpoint and end of therapy, were used with different set values of the reduced scattering coefficient and its wavelength

dependence. There are limited tumor scattering parameters reported in neoadjuvant chemotherapy monitoring studies to guide our selection. The trend in scattering power (i.e. the wavelength dependence of scattering) considered by us was based on the percent changes at 4 weeks and pre-surgery reported by Soliman *et al.* [73]. The scattering amplitude (i.e. the absolute value of scattering) was then set to decrease by 10% at the therapy midpoint and by another 10% at the end of therapy. By fixing these decreasing scattering values, the trends in NACP #5 [Hb], [HbO_2], [HbT], and SO_2 were found to be all in the same direction, with magnitudes within one standard deviation of each point, compared to when the scattering parameters were fixed to the same value throughout therapy. Therefore, chemotherapy induced scattering property responses are unlikely to affect the chromophore concentration trends observed in this work.

The cancer-to-healthy-tissue contrast in the chromophore concentrations at baseline were examined to determine if the level of NAC response could be predicted before treatment began. This contrast measure was calculated at baseline in two different ways, as the difference between the average chromophore concentration at the tumor ROI and either the one at the healthy background tissue in the same breast or at the symmetrical region in the contralateral breast. The tumor contrast measured at baseline, however, was not able to distinguish response groups for this patient population.

With a larger sample size of patients, one may perform more refined statistical analyses, such as an ordinal logistic regression to determine which optical parameters at which time points are significantly different between R and NR groups. Additonally, a more stratified analysis of breast cancer subtypes, chemotherapy regimens, and response to therapy (i.e. partial vs. complete responders) may be performed. Since it has been

reported that pCR is a more relevant endpoint for TNBC and HER2+ cases, one could determine if there are certain optical parameters that may serve as better outcome predictors for a given subtype.

3.5. Conclusions

Ten breast cancer patients receiving neoadjuvant chemotherapy were imaged at each treatment time point using broadband, continuous-wave, optical mammography. For eight of these ten patients, the tumor ROI fell within the field of view of the optical mammograms throughout NAC and were analyzed for discrimination of responders and non-responders. The time evolutions of [HbT], [HbO_2], and SO_2 at the tumor ROI during the course of therapy have been found to correlate with pathologic response. A cumulative response index (CRI), which may be based on any tumor parameter, was developed to assess how individual patients respond throughout treatment. The best performance was obtained with the SO_2 CRI which achieved a 100% sensitivity and specificity at therapy midpoint and beyond.

To further confirm the clinical importance of early assessment of patient response to NAC, a published study reported a neoadjvuant chemotherapy trial where therapy was switched based on the initial clinical response as assessed by physical exam (palpation), ultrasound, and mammography at the end of the second NAC cycle[100]. By changing the therapy regimen for patients with a clinical poor response, the ER+/HER2− patients were found to have a significant improvement in disease free suvival[100]. A non-invasive, safe, and relatively simple imaging tool (like optical mammography) that can determine clinical response and also predict pathologic response can serve as a useful technique to assess the efficacy of NAC and allow for physicians to change treatment for non-responders.

Chapter 4: Protocols for inducing coherent hemodynamic oscillations

4.1. Background

Cerebral hemodynamics features spontaneous fluctuations over specific frequency bands associated with very-low-frequency oscillations ($0.02 – 0.05$ Hz)[101], low-frequency oscillations ($0.08 – 0.15$)[9], respiration ($0.2 – 0.3$ Hz)[102], and heart beat (~1 Hz)[103]. Furthermore, induced oscillations have been used for studying cerebral autoregulation, a physiological mechanism that regulates cerebral vascular tone to maintain near-constant cerebral blood flow in response to fluctuations in arterial blood pressure. Oscillations can be induced by a number of protocols, including paced breathing[104], pneumatic thigh cuffs[105], head-up-tilting[106], squat-stand maneuvers[107], and lower body negative pressure[108].

Cerebral autoregulation is the mechanism that maintains cerebral blood flow despite changes in blood pressure, such as those resulting from induced oscillations. Simultaneous measurements of mean arterial pressure and cerebral blood flow velocity in the middle cerebral artery (MCA) (which is proportional to cerebral blood flow if the MCA's diameter remains constant) have been done, using finger plethysmography and trans-cranial doppler (TCD) respectively, to characterize cerebral autoregulation by a number of groups.[109–112] Specifically, induced oscillations in mean arterial pressure (MAP) at targeted frequencies will cause oscillations in cerebral blood flow (CBF) where the faster recovery of CBF results in it leading MAP in phase. The magnitude of this phase difference can be tied to the effectiveness with which the brain can autoregulate blood flow.[113] Diehl et al report that in healthy subjects performing a paced breathing protocol at 0.1 Hz CBF leads MAP by 70° whereas for subjects with arteriovenous malformations CBF leads MAP

by 27° on the affected side and 40° on the unaffected side.[114] Claassen et al further characterized the relationship between CBF and MAP using a squat-stand maneuver at three frequencies (0.025, 0.5 and 0.1 Hz) and showed that the phase delay decreased as frequency increased (45° at 0.0250 Hz and 25° at 0.1 Hz).[107]

While TCD is sensitive to changes in blood flow velocity in large vessels, NIRS can measure tissue concentrations of oxyhemoglobin and deoxyhemoglobin ([HbO_2] and [Hb] respectively) resulting from microvascular perfusion. Additionally, NIRS can provide functional information regarding oxygen saturation and cerebral blood volume (CBV) which also pertain to the metabolic rate of oxygen and vessel compliance, respectively.[115] A number of NIRS studies have reported phase measurements for both spontaneous and induced oscillations in [HbO_2] and [Hb] as an alternative method to study cerebral autoregulation. For clarity, we have translated the results of these studies in to the phase difference between oscillations in [Hb] minus oscillations in [HbO_2], where a negative phase corresponds to oxyhemoglobin oscillations leading deoxyhemoglobin oscillations. Spontaneous oscillations were reported to have a phase relationship of -130° to −150° in the frequency range 0.05 – 0.08 Hz in infants[116] and −303° at 0.1 Hz in adults at rest[101] and −285° at 0.08 Hz in adults during deep sleep.[117] Recently, Watanabe et al report phase relationships of −72° to −131° at 0.1 Hz as term, early- and late-preterm infants grow providing the capability to distinguish between neurovascular development stages.[118] Alternatively, induced oscillations either with paced breathing or cyclic occlusions using thigh cuffs have also shown a similar dynamic relationship between [Hb] and [HbO_2]. Reinhard et al. reported phase differences between [Hb] and [HbO_2] oscillations at 0.10 Hz paced breathing of −200° in healthy subjects, and −240° in patients with unilateral carotid

obstruction.[104] Paced breathing at 0.07 – 0.25 Hz has been reported to have decreasing phase differences from −180° to −300° with increasing frequency.[119] Tgavalekos et al reported phase differences ranging from −150° to −250° in the frequency range 0.046 – 0.083 Hz in the healthy adult brain and phase differences close to 0° in the healthy breast over the same frequency range while using pneumatic thigh cuffs to induce oscillations.[53] Additionally, Pierro et al induced oscillations using pneumatic thigh cuffs and reported phase differences of −180° to −300° in healthy subjects and those undergoing dialysis.[120] The spectral relationship of these phase differences was translated into differences in the microvascular blood flow between the two populations using a novel hemodynamic model.[120]

Coherent hemodynamics spectroscopy (CHS), is a method for studying hemodynamic physiological processes and tissue oxygen consumption in terms of the phases and amplitudes [Hb], [HbO_2] and total-hemoglobin ([HbT]) concentrations at multiple frequencies of oscillations.[121] The amplitude and phase of [Hb](t), [HbO_2](t), [HbT](t) and MAP(t) oscillations over time, t, at angular frequency ω can be described with phasor notation: **D**(ω), **O**(ω), **T**(ω) and **MAP**(ω) respectively.[122] By means of this hemodynamic model, the relative amplitudes of these phasors and their phase relationships can be related to physiological parameters such as blood flow and cerebral autoregulation. However, to take advantage of CHS, producing reliable and coherent oscillations in oxy-, deoxy-, total-hemoglobin and mean arterial pressure are critical. Many different protocols have been used to induce oscillations assuming that the hemodynamics are driven by changes in **MAP** and the resulting phasors, **D**, **O**, and **T** are all equivalent. No controlled comparison of multiple protocols has been done to better understand their hemodynamic

response. While squat-stand and head-up tilt maneuvers have been shown to produce reliable oscillations, they are prone to motion artifacts at higher frequencies. Lower body negative pressure provides a subject independent stimulus that may be suitable for CHS, however it requires significant equipment, and pressures that produce reliable oscillations are often uncomfortable for subjects making it clinically unpractical[108]. For this paper, we focus on the paced breathing and pneumatic thigh-cuff protocols. They allow oscillations to be induced at multiple targeted frequencies and are practical in their approach. The purpose of this work is to identify 1) whether one of these protocols is more effective at inducing oscillations, and 2) whether the induced oscillations result in the same characteristic phase relationships between **D**, **O**, **T**, and **MAP**. We also translate our results into an indirect measure of cerebral blood flow, CBF, using a hemodynamic model, and discuss the importance of using spectral information to apply CHS.

4.2. Methods

Eleven healthy subjects (age range: 23 to 53 years old) participated in the study. The Tufts University Institutional Review Board approved the experimental protocol, and the subjects provided written informed consent prior to the experiment. Figure 4.1 shows the experimental setup.

4.2.1. NIRS measurements

The NIRS measurements were performed with a frequency-domain commercial NIRS instrument (OxiplexTS, ISS Inc., Champaign, Illinois). Optical probes connected to the spectrometer delivered light at two wavelengths, 690 and 830 nm, at 8 source–detector distances from 5 – 40 mm in 5 mm increments. The brain probe was placed against the

right side of the subject's forehead, to access tissue in the prefrontal cortex, and secured with a flexible headband.

4.2.2. Inducing systemic blood pressure oscillations

The experiment consisted of six two-minute periods of induced oscillations, three using the pneumatic thigh-cuffs followed by three using paced breathing. Between each two-minute period a one-minute baseline measurement was performed. Another three-minute baseline period was measured before and after the six periods of oscillations resulting in a total measurement time of 23 min.

For the pneumatic thigh-cuff protocol, the thigh cuffs were wrapped around both of the subject's thighs and connected to an automated cuff inflation system (E-20 Rapid Cuff Inflation System, D.E. Hokanson, Inc., Bellevue, Washington). The air pressure in the thigh cuffs was continuously monitored with a digital manometer (Series 626 Pressure Transmitter, Dwyer Instruments, Inc., Michigan City, Indiana). During each two-minute period the thigh-cuffs were inflated to 200 mmHg and deflated at a frequency of 0.1 Hz resulting in 12 oscillations for each period. Alternatively, for the paced breathing protocol, the subject was provided cues every 5 seconds to either inhale or exhale by the Prana Breath Android™ app resulting in a paced breathing regimen of 0.1 Hz for 12 oscillations as well. No further instructions regarding breathing depth or pace were provided. The rate and depth of breathing was recorded using a respiration belt containing a strain gauge wrapped around the subject's chest. Continuous arterial blood pressure (ABP) was recorded with a beat-to-beat blood pressure monitoring system (NIBP100D, BIOPAC Systems, Inc., Goleta, California). Analog outputs of the ABP monitor, respiration belt, and thigh cuff pressure monitor were fed to auxiliary inputs of the NIRS instrument for concurrent

recordings with the NIRS data at 12.5 Hz for subjects 1 and 2 and 9.9 Hz for subjects 3 – 11. Mean arterial pressure (MAP) was calculated from the ABP signal and translated to a percent change in MAP by taking the average MAP signal from the baseline measurements as a reference. We introduce lowercase acronyms representing relative percent changes from baseline, where the percent change in MAP with respect to baseline is denoted as $map(t) = {(MAP(t) - MAP_0)}/{MAP_0}$ with the corresponding phasor **map**(ω).

The subject was asked to remain still and refrain from speaking for the entire experiment to avoid any motion artifacts. We tested the effects of varying the subjects' position on the amplitude of map and [HbT] oscillations. The positions tested were determined based on their feasibility in a clinical setting—namely seated, lying down, and lying down with either torso raised, or the legs raised to a 30° angle respective to the bed. We found that the relative body position had no effect on the amplitude of oscillations in map and [HbT]. Subsequently, we chose to perform experiments in a seated position as it provides the most comfortable experimental setup.

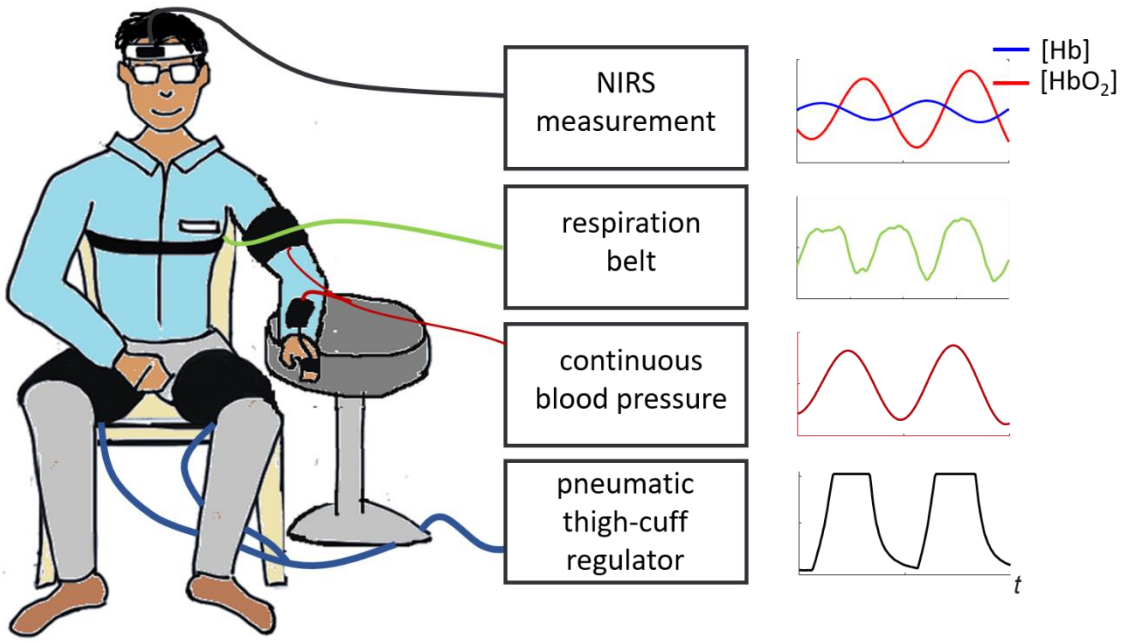

Figure 4.1: Experimental setup. Signals from the NIRS device, arterial blood pressure (ABP) monitor, thigh-cuffs, and respiration belt were recorded synchronously. Representative data for each measurement shown on the right for 0.1 Hz oscillations.

4.2.3. Data analysis

Data analysis and processing were performed with MATLAB® (Mathworks Inc., Natick, Massachusetts). We first use the initial 30 s of data to measure baseline concentrations of oxy-, deoxy-, and total hemoglobin ($[HbO_2]_0$, $[Hb]_0$, and $[HbT]_0$ respectively) using the multi-distance measurements from our optical probe, and assuming extinction coefficients for $[HbO_2]$ and $[Hb]$ from the literature.[123,124] We use $[HbO_2]_0$ and $[HbT]_0$ to calculate the baseline hemoglobin saturation, $S_0 = [HbO_2]_0/[HbT]_0$, which is used in our calculation of cbf described later. Using the modified Beer–Lambert law (Eq. (2.1)), we translate the intensity time traces at the furthest source-detector distance (which is most sensitive to changes in the brain) into changes in the concentrations of oxy-hemoglobin ($\Delta[HbO_2](t)$), deoxy-hemoglobin ($\Delta[Hb](t)$), and total-hemoglobin ($\Delta[HbT](t)$) in units of μM.[50] This time trace is used to measure the phasors **O**, **D**, and **T**.

To compare the capability of each protocol to drive cerebral hemodynamic oscillations with oscillations in MAP, we compare the magnitude of MAP oscillations to the magnitude of oscillations in cerebral blood volume (CBV) which is defined as liters of blood over liters of tissue. Since [HbT] is the measured concentration of total-hemoglobin in tissue, CBV is related to [HbT] by the concentration of hemoglobin in blood (~2300 μM), or $T = 2300\mu M \cdot \mathrm{CBV}$. In this comparison however, we wish to consider percent changes such that $cbv(t) = {(T(t) - T_0)}/{T_0}$ with its corresponding phasor **cbv**(ω) at 0.1 Hz.

Now we explain the procedure to extract phasors associated with oxy- deoxy- total hemoglobin and MAP oscillations which represent sinusoidal oscillations in each parameter at a specific frequency (in this case only 0.1 Hz). The time traces $\Delta[HbO_2](t)$, $\Delta[Hb](t)$, $\Delta[HbT](t)$, map(t) were filtered with a narrow bandwidth, linear phase, Parks-McClellan algorithm.[125] The filter had a width of 0.01 Hz that was centered at 0.1 Hz. The Hilbert transform was applied to the bandpass-filtered signals in order to translate the time traces into phasors by using the instantaneous amplitude and phase at 0.1 Hz.[126] The magnitudes of the phasors **D**(ω), **O**(ω), **T**(ω), **cbv**(ω) and **map**(ω) and the phase relationships, arg(**D**(ω))−arg(**O**(ω)) and arg(**cbv**(ω))−arg(**map**(ω)) were computed and averaged within the time ranges of the measurements for each period of induced oscillations. This method is well-suited to identify the instantaneous phase and amplitude relationship for oscillations at a single frequency. However, since we induce periods of oscillations that occur only for certain time-periods in our data, we are applying a stationary frequency domain analysis to a non-stationary signal. In this regard, the wavelet transform and short-time Fourier transform are non-stationary methods which more accurately

quantify the phase and amplitude associated only with those portions of the signal pertaining to the induced oscillations. Ultimately, when implementing such an analysis for the application of coherent hemodynamics spectroscopy, the wavelet transform is a non-stationary method that provides the necessary frequency and time resolution to determine the relative phase and amplitude information needed. However, for these experiments we are only concerned with phase relationship associated with the two induced periods at one frequency, and such an exhaustive analysis technique is unnecessary. We used circular statistics for calculating the average phase and standard deviation between pairs of phasors. Figure 4.2 shows representative time traces for the different hemoglobin species, map, cbv, and cbf as well as their corresponding phasors for subject 4 during one period of paced breathing.

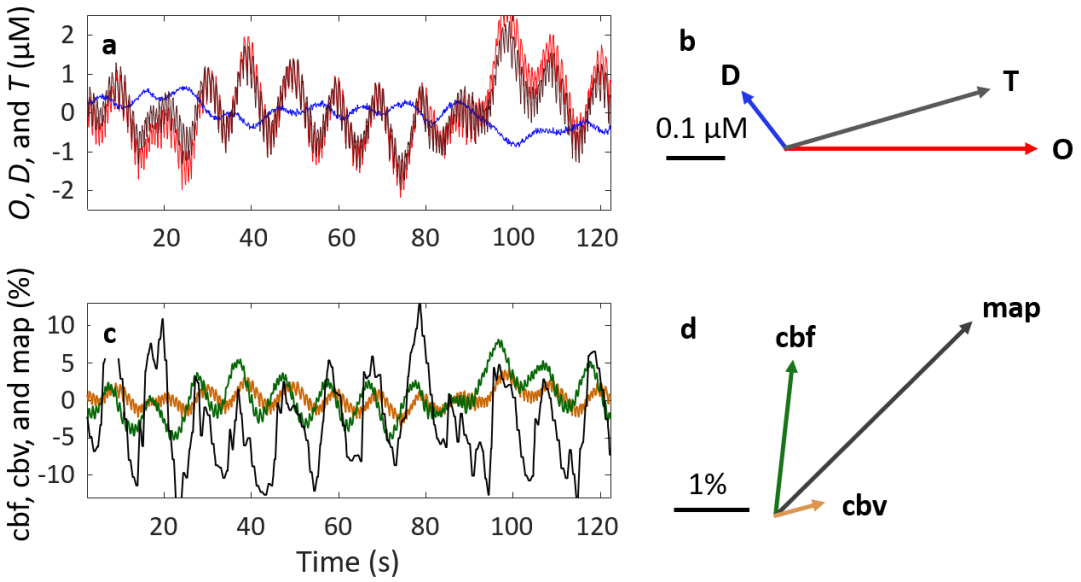

Figure 4.2: Representative measurements from one period of induced oscillations during paced breathing. a) Time traces for [HbO_2], [Hb], and [HbT] and b) their corresponding phasors calculated by using the Hilbert transform. c) Time traces for cbf, cbv, and map and d) their corresponding phasors.

We note that while the phasors **D**(ω), **O**(ω), **T**(ω), **cbv**(ω) and **map**(ω) are measured directly , the cbf phasor requires assumptions on additional physiological parameters, such as the capillary and venous transit times, and the blood volume in the arterial compartment.[127] The calculation of cbf is described in the next section.

4.2.4. Hemodynamic model to calculate cerebral blood flow

We have previously described the method of coherent hemodynamics spectroscopy (CHS)[121] and the application of this dynamic model to calculate cbf(*t*) and its corresponding phasor **cbf**(ω).[128] A representation of this calculation of **cbf** is shown by using vector math on phasors in Figure 4.3A. The dynamic model takes into account that the dynamics in the arterial, capillary, and venous compartments provide individual contributions to the overall dynamics of [HbO_2] and [Hb]. Since we measure **D**, **O**, and **T**, we can first decompose **O** into volume and flow related components under the assumption that changes in the metabolic rate of oxygen consumption are negligible.[127] As such, $\mathbf{O} = \mathbf{O_v} + \mathbf{O_f}$, where $\mathbf{O_v}$ and $\mathbf{O_f}$ are the phasors representing oscillations in oxy-hemoglobin that result from volume and flow oscillations respectively. To calculate **cbf**, we first set a value for $\mathbf{O_v}$ and determine $\mathbf{O_f}$ based on our measured value of **O**. We then use a frequency dependent complex transfer function to relate $\mathbf{O_f}$ and **cbf**.[128] The remainder of this section describes this method in further detail.

The volume dependent component of **O** is described by the dilation and constriction of vessels in the different compartments. Where $\mathbf{O_v}$ becomes the sum of the weighted dynamic contributions of the arterial, venous, and capillary compartments to **cbv**.

$$\mathbf{O_v}(\omega) = S^{(a)}\mathrm{CBV}_0^{(a)}\mathbf{cbv}^{(a)}(\omega) + \mathbb{F}^{(c)}\mathrm{CBV}_0^{(c)}\langle S^{(c)}\rangle\mathbf{cbv}^{(c)}(\omega) + S^{(v)}\mathrm{CBV}_0^{(v)}\mathbf{cbv}^{(v)}(\omega) \tag{4.1}$$

We introduce the notations (a), (v), and (c) where these superscripts refer to the partial contributions to the base term from the arterial, venous and capillary compartment respectively. Here, $\mathbf{cbv}^{(a)}$, $\mathbf{cbv}^{(v)}$, and $\mathbf{cbv}^{(c)}$ are the phasors representing the dynamic contributions to **cbv** from the arterial, venous and capillary compartments respectively, and their weights are the hemoglobin saturation of these compartments $S^{(a)}$, $S^{(v)}$, and $S^{(c)}$ and the partial volumes of each compartment $\mathrm{CBV}_0^{(a)}$, $\mathrm{CBV}_0^{(v)}$ and $\mathrm{CBV}_0^{(c)}$ where $\mathrm{CBV}_0 = \mathrm{CBV}_0^{(a)} + \mathrm{CBV}_0^{(v)} + \mathrm{CBV}_0^{(c)}$. The Fåhreus factor, $\mathcal{F}^{(c)}$, accounts for the ratio of hematocrit between the capillaries and larger vessels, however since capillary recruitment or dilation is unlikely we set $\mathbf{cbv}^{(c)} = 0$, eliminating this term.[129–131] The arterial saturation for healthy subjects is fixed for our calculations at $S^{(a)} = 0.98$. The oxygen saturation of hemoglobin decays exponentially along the capillary, and takes the following value at the end of the capillary

$$S^{(v)} = S^{(a)} e^{-\alpha_{\dot{o}} t^{(c)}} \tag{4.2}$$

where $t^{(c)}$ is the blood transit time in the capillaries and $\alpha_{\dot{o}}$ is the rate of oxygen diffusion in the capillaries and is equal to 0.8.[132] By fixing $S^{(a)}$, and $\mathrm{CBV}_0^{(a)}$ we can take advantage of our measurement of the baseline hemoglobin saturation S_0 to calculate $\mathrm{CBV}_0^{(v)}$. Since S_0 can also be broken down into its contributions from each compartment with similar weights:

$$S_0 = S^{(a)} \frac{\mathrm{CBV}_0^{(a)}}{\mathrm{CBV}_0} + \langle S^{(c)} \rangle \frac{\mathrm{CBV}_0^{(c)}}{\mathrm{CBV}_0} + S^{(v)} \frac{\mathrm{CBV}_0^{(v)}}{\mathrm{CBV}_0} \tag{4.3}$$

where $\langle S^{(c)} \rangle$ is the average saturation in the capillary compartment given by:

$$\left\langle \mathrm{S^{(c)}} \right\rangle = \mathrm{S^{(a)}} \left(\frac{1 - e^{-\alpha_{\dot{o}} t^{(c)}}}{\alpha_{\dot{o}} t^{(c)}} \right) \tag{4.4}$$

From Eqs. (4.2-4):

$$\mathrm{CBV}_0^{(v)} = \frac{S_0 - S^{(a)}\left[\frac{\mathrm{CBV}_0^{(a)}}{\mathrm{CBV}_0} + \left(1 - \frac{\mathrm{CBV}_0^{(a)}}{\mathrm{CBV}_0}\right)\left(\frac{1-e^{-\alpha_0 t^{(c)}}}{\alpha_0 t^{(c)}}\right)\right]}{S^{(a)}\left[e^{-\alpha_0 t^{(c)}} - \frac{1-e^{-\alpha_0 t^{(c)}}}{\alpha_0 t^{(c)}}\right]}\mathrm{CBV}_0 \quad (4.5)$$

For this study, we assume $t^{(c)}$ = 1 s[53], $\mathrm{CBV}_0^{(a)}$ = 0.007[133] and $\mathbf{cbv}^{(a)} = \mathbf{cbv}^{(v)}$ at which point we have fixed the value of $\mathbf{O_v}$. Once $\mathbf{O_v}$ is fixed, and $\mathbf{O_f}$ is the phasor difference of **O** and $\mathbf{O_v}$ where **O** is measured. From here **cbf** and $\mathbf{O_f}$ are related by a frequency dependent complex transfer function:

$$\mathbf{O_f} = [\mathrm{F}^{(c)} CBV_0^{(c)}\left(\langle S^{(c)}\rangle - S^{(v)}\right)H_{RC-LP}^{(c)}(\omega) + CBV_0^{(v)} S^{(v)} \alpha t^{(c)} H_{G-LP}^{(v)}(\omega)]\mathbf{cbf} \quad (4.6)$$

Where the transfer function $H_{RC-LP}^{(c)}$ describes the RC low-pass filter behavior of the blood transit time in the capillary compartment and the transfer function $H_{G-LP}^{(v)}$ represents the Gaussian low-pass filter behavior in the venous compartment. These transfer functions are defined by $t^{(c)}$ and $t^{(v)}$, the blood transit time in the venous compartment, and define the frequency dependent phase relationship between **cbf** and $\mathbf{O_f}$. By setting values for $t^{(c)}$ = 1 s, $S^{(a)}$ = 0.98, $\mathrm{CBV}_0^{(a)}$ = 0.007 and $t^{(v)}$ = 5.6 s [53], we fix this relationship. In practice, we have previously shown that by inducing oscillations at multiple frequencies we can apply the hemodynamic model using a spectroscopic approach to estimate values for $t^{(c)}$, $t^{(v)}$ and the relative blood volume contributions between the different compartments.[119] In which case we provide a direct quantitative measurement of the relationship between **cbf** and **T** which provides information about the efficacy of cerebral autoregulation. However, in this study, we only consider one frequency, 0.1 Hz, to have multiple repetitions in a single experiment to provide an intrasubject comparison of the paced breathing and thigh-cuff protocols. In Figure 4.3B–D, we describe how the phase relationship arg(**cbf**)−arg(**T**) changes as a function of the three set parameters, $t^{(c)}$, $t^{(v)}$ and $\mathrm{CBV}_0^{(a)}$ for Subject 4.

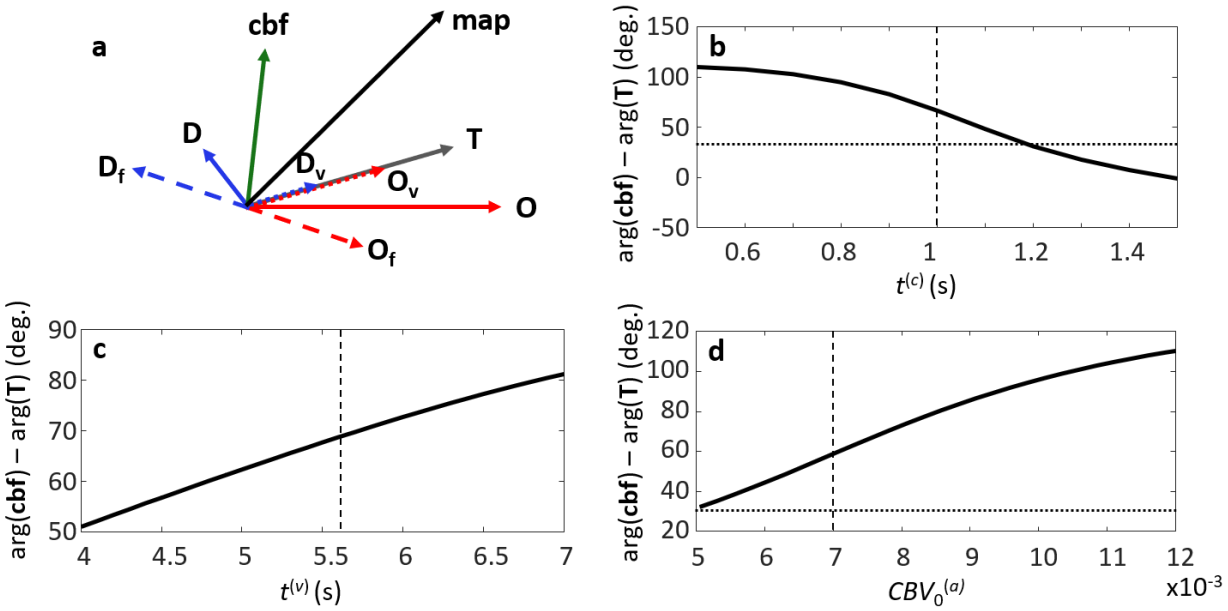

Figure 4.3: a) Phasor diagram of different hemoglobin species and their contributions from volume and flow oscillations for Subject 4. b) Phase difference between **cbf** and **T** as capillary transit time, $t^{(c)}$, changes. c) Phase difference between **cbf** and **T** as venous transit time, $t^{(v)}$, changes. d) Phase difference between **cbf** and **T** as partial contribution of the arterial compartment changes. The vertical dashed lines in (b-d) represent the values fixed for the calculations done in this study. The ranges for the values of $t^{(c)}$, $t^{(v)}$, and $CBV_0{}^{(a)}$ tested correspond to physiologically reasonable values. For reference the phase difference between **cbf** and **map** is 31 deg. represented by the horizontal dashed lines in (b) and (d).

In healthy subjects, the presence of cerebral autoregulation is dictated by **cbf** leading **map** in phase. Subsequently, values of $t^{(c)}$ beyond 1.2 s where **cbf** lags **map** would suggest that this range of values for $t^{(c)}$ may be physiologically unreasonable. An increase in $t^{(v)}$ results in a longer delay time associated with the gaussian low pass filter relationship in the venous compartment (Eq. (4.6)). Subsequently we observe a larger phase difference between **cbf** and **T**. Similarly, one would expect increasing $t^{(c)}$ to produce a larger delay time in the RC low pass filter relationship in the capillary compartment and produce a similar trend in arg(**cbf**)−arg(**T**). However, it is important to consider that $t^{(c)}$ in this case also affects the venous and capillary contributions to CBV_0 (Eq.(4.5)). The larger venous transit time (assumed 5.8 s here) is a larger component of the phase difference between **cbf** and **T**, by

increasing $t^{(c)}$ we also decrease $CBV_0^{(v)}$ and increase $CBV_0^{(v)}$ resulting in a smaller phase difference between **cbf** and **T**. Similarly, increasing $CBV_0^{(a)}$ results in larger $CBV_0^{(v)}$ and a larger phase difference between **cbf** and **T.** It is important to note that the calculation of **cbf** is an indirect measure based on assumptions for $t^{(c)}$, $t^{(v)}$, and $CBV_0^{(a)}$. In this sense the variability in our calculated **cbf** between subjects will depend entirely on the variability between **O**, **T**, and S_0, since these are the measured parameters that affect our calculation of $\mathbf{O_f}$.

4.2.5. Statistical analyses

Coherent hemodynamics spectroscopy relies on coherent oscillations between **map** and **T**. The underlying assumption is that when these oscillations exist with a high degree of coherence, the primary force driving oscillations in **T** is **map** and the dynamic model can describe the resulting relationship between **O** and **D** well. When oscillations are not coherent, the dynamic model does not completely describe **T**, and other drivers (such as localized vascular dynamics, effects of the superficial layers, or other artifacts) affect the oscillations we measure. In any practical application, it is unlikely that the dynamic model can fully describe all oscillations in T, so we have developed a methodology to test the coherence between oscillations based on their phase synchronization index (PSI).[134] Briefly, we assumed a null hypothesis that the two time traces, [HbT](t) and map(t), are completely random and have no phase synchronization. We created a distribution for our null hypothesis using random numbers. Based on an $\alpha = 0.95$, we identified a PSI threshold within this distribution for [HbT] and map, $PSI_{[HbT],map}$. We calculate the PSI for each induced 2 minute period of oscillations, and only consider those oscillations passing the PSI threshold in our analyses. Although $PSI_{[HbT],map}$ serves as a sufficient measure to

identify coherent hemodynamic oscillations, to assess differences in arg(**D**)−arg(**O**), we note that oscillations in [Hb] are typically much smaller than oscillations in [HbO_2] and [HbT]. Accordingly, we calculated the PSI threshold between oscillations of [Hb] and map, $PSI_{[Hb],map}$ as well to identify those oscillations where a comparison of arg(**D**)−arg(**O**) is relevant. In some cases, it is possible for $PSI_{[HbT],map}$ to be significant and $PSI_{[Hb],map}$ to be insignificant based on our PSI thresholds. In our comparison of the protocols capability to induce oscillations, we use the PSI threshold, $PSI_{[HbT],map}$, and the amplitude ratio, |**cbv**|/|**map**|, as metrics to qualify whether one protocol is advantageous over the other. The number of periods that pass our PSI threshold indicates how robust our protocol is in its capability to induce hemodynamic oscillations, and |**cbv**|/|**map**| relates the magnitude of our measured NIRS oscillations to the driving oscillation in map using each protocol. Additionally, to understand the dynamic phase relationships arg(**D**)−arg(**O**), arg(**cbf**)−arg(**map**), arg(**cbf**)−arg(**cbv**), and arg(**cbv**)−arg(**map**) simultaneously with their corresponding amplitude ratios |**D**|/|**O**|, |**cbf**|/|**map**|, |**cbf**|/|**cbv**|, and |**cbv**|/|**map**| between protocols we create vectors that represent the phasor ratios of each pair of phasors. For each subject and protocol, we take an average value of the amplitude and phase of each phasor describing an induced period of oscillation that passed the PSI threshold $PSI_{[HbT],map}$. We then define a vector, with an amplitude defined by the average of the amplitude ratios |**D**|/|**O**|, |**cbf**|/|**map**|, |**cbf**|/|**cbv**|, or |**cbv**|/|**map**| and an angle defined the circular average of the phase differences, arg(**D**)−arg(**O**), arg(**cbf**)−arg(**map**), arg(**cbf**)−arg(**cbv**), or arg(**cbv**)−arg(**map**) respectively. For the vector **D**/**O**, we also exclude periods that do not pass the PSI threshold $PSI_{[Hb],map}$. A vector, for example, representing the phasor ratio **D**/**O** has an amplitude described by the average of |**D**|/|**O**| during induced oscillations that meet

the PSI thresholds $PSI_{[Hb],map}$ and $PSI_{[HbT],map}$ for a specific subject and protocol. The angle of this vector is similarly described by the average of arg(**D**)−arg(**O**) for the relevant oscillations induced by each protocol for each subject.

4.3. Results

Table 4.1: # of Periods above PSI Threshold at α = 0.95

	$PSI_{[Hb], map}$		$PSI_{[HbT], map}$	
Subject #	Cuff	PB	Cuff	PB
1	1	1	2	3
2	1	2	1	1
3	2	1	3	3
4	3	3	3	3
5	2	1	3	3
6	3	1	3	3
7	1	2	3	3
8	1	0	3	3
9	1	0	3	1
10	0	3	2	3
11	1	2	1	2
Success	48%	48%	82%	85%

Cuff—thigh-cuff protocol; PB—paced breathing protocol; success - percent of total (33) periods that pass the PSI threshold

We tested the capability of each protocol to induce coherent hemodynamic oscillations driven by oscillations in mean arterial pressure. For each subject we were able to induce coherent oscillations with both protocols. The success rate of each protocol for each subject is in Table 4.1. Out of a total 33 periods for each protocol across all 11 subjects we induced coherent oscillations based on the PSI threshold in 27 periods (82%) with the thigh-cuff protocol and 28 periods (85%) with the paced breathing protocol at 0.1 Hz. However, we found that measuring coherent oscillations in [Hb] was less robust. In both protocols only 16 (48%) of the total 33 periods produced oscillations that passed the PSI threshold. In these cases, oscillations in [Hb] were likely too small such that the filtered signal had random phase. More importantly, both protocols show the same success rate for

the PSI threshold between **D** and **map** across subjects, however between subjects the efficacy of each protocol varied. For example, we were able to induce oscillations in **D** for Subject 4 in all periods, however for subject 10, the paced breathing protocol was more effective, and vice versa for subject 6. It is important to note that a small |**D**|, does not indicate that coherent oscillations were not induced but rather that the oscillations were likely dominated by the arterial compartment.

While the PSI between **cbv** and **map** provides a measure of coherence, |**cbv**|/|**map**|, indicates the relative amplitude of the oscillations. Although practically, larger oscillations in **cbv** provide more robust measurements, the relationship between **cbv** and **map** is also related to underlying physiological parameters such as vascular compliance.[135] Figure 4.4 shows the ratio of amplitudes between **cbv** and **map**. No subject showed a significant difference in |**cbv**|/|**map**| between the protocols. The group averages of |**cbv**|/|**map**| are 0.20 ± 0.09 for the thigh-cuff protocol and 0.19 ± 0.10 for the paced breathing protocol. Additionally, we note that while there is a high degree of variability across subjects the differences in |**cbv**|/|**map**| between protocols is minimal within each measurement.

The vectors shown in Figure 5, are defined by the average phasor ratios for each protocol and each relevant combination of measured or calculated parameters across all subjects.

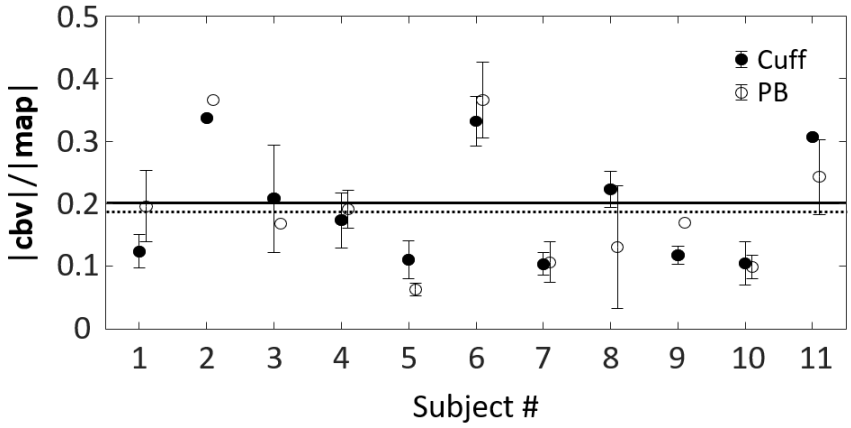

Figure 4.4: Ratio of amplitudes of **cbv** and **map**. Error bars represent one standard deviation from the mean ratio of amplitudes among the included periods. Points that have no error bars represent cases when only one period passed the PSI threshold. The solid and dashed horizontal lines represent the mean value across all subjects for the thigh-cuff (Cuff) and paced breathing (PB) protocols respectively.

We found that the group average angle of **cbv**/**map** was the same for the two protocols (−43° and −44° for cuff and paced breathing respectively) meaning the timing of how **map** is translated into **cbv** is constant (Table 4.1). Typically, we expect **map**, our physiological driver, to lead **cbv**, and for most cases we see a consistent relationship. However, for subjects 2 and 11 we found an atypical result for the angle of **cbv**/**map** which was also different between the two protocols (Figure 4.5). For subject 11 we found that the paced breathing protocol produced a similar phase delay to the rest of the subjects (−50°) with **cbv** lagging **map**, however, for the cuff protocol we found that the angle of **cbv**/**map** was closer to 0°. For subject 2, we found that the paced breathing protocol resulted in **cbv** leading **map** by 35°. This suggests that either **cbv** leads **map** by ~1 s or **map** leads **cbv** by ~9 s. We use |**cbv**|/|**map**| and the PSI threshold as measures to assess whether coherent oscillations were induced, while the relative phase and amplitude of **D** and **O** are the measured input parameters for the application of CHS.

Table 4.2: Average amplitude and phase of group averaged phasor ratios

	Cuff	Paced Breathing
D/**O**	$0.2 \pm 0.1 \angle -210 \pm 46$	$0.2 \pm 0.1 \angle -205 \pm 45$
cbf/**cbv**	$2.3 \pm 1.8 \angle 80 \pm 20$	$2.5 \pm 1.1 \angle 71 \pm 12$
cbf/**map**	$0.28 \pm 0.27 \angle 29 \pm 27$	$0.17 \pm 0.14 \angle 23 \pm 23$
cbv/**map**	$0.20 \pm 0.09 \angle -43 \pm 41$	$0.19 \pm 0.10 \angle -44 \pm 25$

For **D**/**O**, while the group averages between the two protocols is similar (−210° for cuff and −205° for paced breathing), there exists a larger variability in this parameter well described by the variability in the vectors shown in Figure 5. Additionally, we found that for subjects 5 and 6 the differences in the angle of **D**/**O** between protocols is 51° and 169° respectively while the differences for the remaining subjects are less than 30° (Figure 4.5). For subject 5 we found that the angle of **D/O** was more negative for the cuff, −209°, than for paced breathing, −159°.. For subject 6 we found that the opposite to be the case with the angle of **D**/**O** equal to −33° and −224° for the cuff and paced breathing protocols respectively. In these cases, it's possible that the different protocols induced subject dependent differences which resulted in the varied phase difference.

Finally, **cbf**/**cbv** and **cbf**/**map** the phasor ratios associated with our calculated **cbf** parameter were the same for the two protocols. However, the variability in **cbf** between the two protocols is dependent on the relationship between **O** and **T**. Since the amplitude of **D**/**O** is typically small (0.2 for both protocols) the phase relationship, arg(**O**)−arg(**T**) is also small. Subsequently the resulting angle of $\mathbf{O_f}$ varies little between subjects (Figure 4.3A). Since we assume the defining parameters of the transfer functions that relate $\mathbf{O_f}$ to **cbf** the variability we see in the angle of **cbf/cbv** is artificially small without measured values of $t^{(c)}$, $t^{(v)}$ and $CBV_0^{(a)}$ for each case. However, the assumptions of $t^{(c)}$, $t^{(v)}$ and $CBV_0^{(a)}$ represent

physiologically reasonable values, and in healthy subjects, we expect **cbf** to lead **map** and similarly **cbv** which we reproduce correctly except for Subject 3. In this case we expect our assumptions underestimate $t^{(v)}$ and $CBV_0^{(a)}$ or overestimate $t^{(c)}$ since increasing $t^{(v)}$ or $CBV_0^{(a)}$ or decreasing $t^{(c)}$ would result in **cbf** leading **map** in this calculation (Figure 4.3B-D).

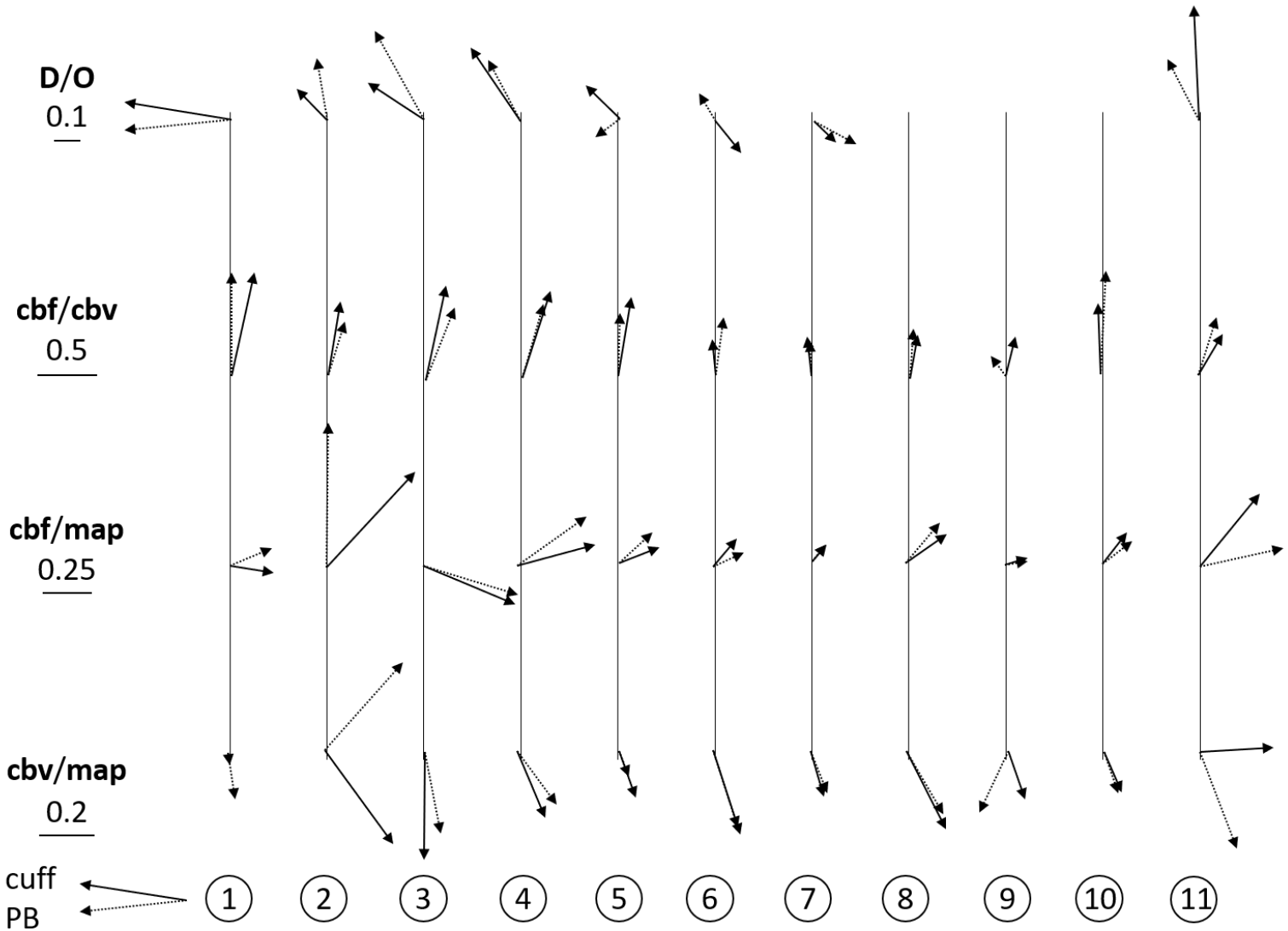
D/O
0.1
cbf/cbv
0.5
cbf/map
0.25
cbv/map
0.2
cuff
PB
1
2
3
4
5
6
7
8
9
10
11

Figure 4.5: Phasor ratio vectors for **D**/**O**, **cbf**/**cbv**, **cbf**/**map**, and **cbv**/**map** for subjects 1-11. The solid arrows represent the vectors for the cuff protocol, and the dashed arrows represent the vectors for the paced breathing protocol. The scale bars are unitless and define the magnitude of the amplitude ratio represented by the length of each vector. The angle of each vector is defined by the average phase relationship between the two phasors in each ratio. For subjects 8 and 9 no oscillations passed the PSI threshold for **D** and **O** with the paced breathing protocol, and for subject 10 no oscillations passed the PSI threshold for **D** and **O** for the cuff protocol.

4.4. Discussion

We have reported a comparison of two protocols, paced breathing and pneumatic thigh-cuffs, performed on 11 subjects to induce coherent hemodynamic oscillations. We found that both protocols provide significant coherent cerebral hemodynamic oscillations with **map** as a driving oscillation. The benefit of these two protocols lies in their capability to induce oscillations at targeted frequencies in a clinical setting. In this work we consider only a single frequency, 0.1 Hz, however we have previously reported using thigh cuffs and paced breathing for multiple frequencies for the application of CHS.[53,120] The values we measure for **D**/**O** coincide with the values reported in literature[53,101,104,120], however, using the relationship between **O** and **D** directly can be challenging due to the high variability in this dynamic relationship. Likely the variability in **D**/**O** amongst healthy subjects is associated with the underlying mechanics of the vascular architecture for each subject. Herein lies the significance of using CHS. While we found that for subjects 5 and 6 **D**/**O** was different for the two protocols, the difference may be explained by which compartment, arterial, venous, or capillary, contributes to the oscillations the most.[121] More importantly, by taking measurements at multiple frequencies and applying CHS, we can measure values of $t^{(c)}$, $t^{(v)}$ and $CBV_0{}^{(a)}$. Specifically, the model would explain a less negative phase angle by either an increase in autoregulation or an increase in $t^{(c)}$.[136] The model

describes autoregulation based on a high-pass transfer function between **map** and **cbf**. In this sense, an increase autoregulation would indicate an increase in **cbf** suggesting the subject was in a hypercapnic state due to the slower than normal respiration rate. If $t^{(c)}$ were increased this would suggest smaller **cbf** suggesting the subject was in a hypocapnic state, potentially a result of deeper breathing during paced breathing. In our study, without measuring the end-tidal CO_2 either scenario is possible, and controlling for this parameter in the future is necessary when using a paced breathing protocol. More critically, we note that the phase relationship between **D** and **O** is indicative of cerebrovascular function, but anatomical and physiological differences between subjects and protocols can limit its use as a direct biomarker for diseases. Using a model, such as CHS, allows for the interpretation of the relationship between these phasors to separate out anatomical differences between subjects, effects of different protocols, and more importantly clinically relevant parameters such as autoregulation or cerebral blood flow.

For the purpose of inducing coherent hemodynamic oscillations, we suggest using thigh-cuffs over the paced breathing protocol since it does not require patients to adhere to the protocol. In our protocol, we record the depth of breathing over time during the paced breathing protocol and found that with minimal instruction the depth and time trace of paced breathing varied widely from subject to subject which could explain the varied phase relationship between subjects. We point out that end-tidal CO_2 is a critical parameter to measure to control for changes in physiological states, however this would require additional instrumentation further complicating the paced breathing protocol. For the thigh cuffs, the only requirement is that the cuff pressure provide an arterial occlusion. For our

experiments we use a cuff pressure of ~200 mmHg which would induce arterial occlusions in any healthy subject.

In two specific cases we found that **cbv** leads **map**. The relationship between **cbv** and **map** is indicative of CBF dynamics and cerebral autoregulation, with possible contributions from the transit time of blood through the microvasculature.[135] For subject 11, we found for the cuff protocol **cbv** and **map** are in phase. This would suggest that the cuff protocol produced oscillations that were dominated by the arterial compartment, however **D**/**O** had an angle of ~90° and had a larger magnitude than the paced breathing protocol. Whereas arterial blood would be dominated by oxy-hemoglobin oscillations resulting in smaller **D**/**O** which also would oscillate in phase. Additionally, for subject 2 intuition would suggest that **cbv** cannot lead map by 1 s as the 35° phase difference suggests, since we consider **map** to be the driving oscillation in our system. Reinhard et al report **cbv** to lag **map** by $-23 \pm 35°$ suggesting that a positive phase relationship is possible. They also report phase differences as high as 60°, however no physiological explanation of these results are provided[104]. Outside of these two instances, the variability associated with the angle of **cbv**/**map** is $-57 \pm 16°$ for the cuff protocol and $-61 \pm 29°$ for the paced breathing protocol suggesting that a consistent relationship exists between **cbv** and **map.**

Understanding the relationship between **cbv** and **map** is important for the application and interpretation of CHS, however the primary concern is producing robust and repeatable measurements of **D**/**O**. In this regard, measuring **T,** and more importantly **cbv**, has proven to be robust. However, without sensitivity to **D**, measurements of the phase angle for **D**/**O** are not reliable. In our measurements we were sensitive to oscillations in **D** approximately 50% of the time. We attribute this to the fact that the oscillations are

dominated by arterial contributions where hemoglobin saturation is ~98%. While we show that both paced breathing and the thigh cuff protocols are similar in their capability to induce oscillations, the mechanism which translates oscillations in **map** to the oscillations we measure is still unclear. Paced breathing induces mechanically generated oscillations, where the respiration changes pleural pressure and ventricular loading resulting in oscillations in mean arterial pressure.[104] Alternatively, the thigh cuffs are intended to provide a sudden increase in ABP when inflated by increasing the total systemic resistance, and the opposite when the cuffs are deflated.[105] Subsequently, we would expect a larger venous contribution from the paced breathing protocol, however our results suggest the variability in **D/O** between subjects masks any discernable differences in the compartmental affects.

4.5. Conclusions

We have shown that paced breathing and cuff protocols are equally useful for inducing coherent hemodynamic oscillations. We found a consistent relationship between mean arterial pressure and cerebral blood volume, however oscillations in [Hb] and [HbO_2] show varied response. Outside of physiological differences that may result in varied responses to paced breathing and cuff protocols, spatial variability, contributions from the superficial layer, or the patient's adherence to the protocol are some factors that could contribute to this variability. Careful consideration is required when interpreting the results of **D/O** between protocols or even subjects. We believe CHS can provide more robust information that is directly related to physiological changes which could be advantageous when applying these hemodynamic protocols in a clinical setting. A larger more comprehensive

study is required to understand the factors that contribute specifically to the variability in **D**/**O**.

Chapter 5: Coherent hemodynamics in breast cancer.

5.1. Background

As was discussed in Section 4.2.4, measurements of oxyhemoglobin ([HbO_2]) and deoxyhemoglobin ([Hb]) concentrations can be translated into measurements of changes in blood flow. While the model presented in Section 4.2.4, was targeting a measurement of cerebral blood flow, the basis of coherent hemodynamics spectroscopy can be theoretically applied to any tissue that exhibits a measurable change in blood flow. For breast cancer detection, the physiological basis for using a change in blood flow as a source of contrast is derived from the different mechanical properties of cancerous tissue regions, and the functional disruption of tissue vasculature associated with cancer. Invasive breast cancers are associated with higher interstitial fluid pressure (IFP) than normal breast tissue[137]. The Young's modulus of elasticity for soft tissue can range from 1 to 100 kPa, however breast cancers can be as much as 15 times stiffer.[138] Ultrasound elastography has been shown to detect different tissue displacements in cancerous tissue as opposed to healthy tissue from externally applied pressure.[139] The compromised vasculature from rapid angiogenesis typical of tumors, can also affect the blood flow and content in tumor tissues. For non-necrotic breast cancer tissue, blood flow has been reported to be greater than in post-menopausal normal breast tissue.[140] The changes in mechanical properties, IFP, and vascular function of cancerous tissue can all affect blood flow, oxygen consumption, and blood content.[9] Changes in these hemodynamic parameters in response to a physical challenge or externally applied pressure can reveal hemodynamic characteristics of healthy and cancerous tissue.

Specifically, blood flow as a hemodynamic parameter in breast cancer has been investigated previously by both diffuse optical methods and others. The use of positron emission tomography (PET) [141–143], color and power Doppler ultrasound[144–146], MRI [96] as well as optical techniques such as diffuse correlation spectroscopy (DCS)[66,147] have been employed. However, clinically the efficacy of ultrasound as a diagnostic technique has been ambiguous due to the lack of sensitivity to smaller blood vessels and lower signal to noise contrast.[147] PET can use the speed of tracer uptake to evaluate relative tumor blood flow, and studies using PET have shown blood flow increases in malignant tumors. Similarly, dynamic contrast enhanced MRI can use the rate of contrast agent uptake to measure relative blood flow, and hemodynamic function.[148] However, as is the case with PET, MRI has limitations due to the cost associated with large instrumentation and extensive clinical procedures requiring exogenous contrast agents. Diffuse correlation spectroscopy (DCS) monitors the temporal fluctuations of scattered light to indirectly infer information about the relative blood flow within the microvasculature. Groups have shown that the tumor tissue is associated with localized increases in blood flow [66,147] and that manual compression of the breast (~20 N of surface pressure) can induce relative decreases in blood flow up to 50%[149]. The challenge in applying DCS to the breast lies in the need for usable signal to noise ratios to employ a transmission geometry which is more sensitive to deeper set tumors. This makes the clinical application of this technique more challenging, however still feasible with additional detectors and longer integration times.

Recently, diffuse optical methods have also been applied in efforts to study the dynamics of [HbO_2] and [Hb]. Different methods of controlling the physical perturbation have been employed such as dynamic compression of the breast[34,47], and paced breathing

similar to protocols in the brain.[33,45,46] Manual compression of the breast by external force increases the interstitial fluid pressure subsequently decreasing the blood content in the breasts of healthy subjects by up to 20%.[47] Regulating respiration or breath-holding can systemically alter the blood pressure to cause 5-10% fluctuation in hemoglobin content in healthy subjects.[33] Tgavalekos et al. were able to induce hemodynamic oscillations in the breast using pneumatic thigh cuffs under the same protocol used in Chapter 4:, and found that oscillations in [HbO_2] and [Hb] were in phase for healthy female subjects.[53] However, the magnitude and temporal dynamics of induced changes have been related to differences in the vasculature between cancerous and healthy tissue.[46,47,150,151]

In this pilot study, we monitor hemodynamics during neoadjuvant chemotherapy to identify coherent oscillations in [HbO_2] and [Hb]. We performed bilateral measurements in a transmission geometry on the breast, before each chemotherapy infusion using pneumatic thigh-cuffs to induce coherent oscillations at targeted frequencies. Specifically, I report the phase relationship between $\Delta[\mathrm{Hb}](t)$ and $\Delta[\mathrm{HbO_2}](t)$ over time, t, at the induced frequencies of oscillation for each chemotherapy infusion. While our original hypothesis was that stiffness in the breast tissue due to cancer would result in a measurable phase difference between $\Delta[\mathrm{Hb}](t)$ and $\Delta[\mathrm{HbO_2}](t)$ (different from the relationship found in Figure 2.8 on the healthy breast), we find that $\Delta[\mathrm{Hb}](t)$ and $\Delta[\mathrm{HbO_2}](t)$ oscillate in phase even in the cancerous breast. We also report on the challenges in performing these measurements with clinical constraints, as well as identify key information needed to further pursue this technique.

5.2. Methods

5.2.1. Patient recruitment

This study was approved by the Institutional Review Board of the Tufts Medical Center, and it was also compliant with the Health Insurance Portability and Accountability Act. Any woman over the age of 21 who was diagnosed with invasive breast cancer and scheduled to undergo neoadjuvant chemotherapy was eligible for this study. All patients read and signed an informed consent before participating. Three patients were enrolled in and followed in this study for the course of their chemotherapy. NACP#11 and #13 had incomplete data sets due to the patients' schedules. However, the data presented for NACP#12 are representative of the data for all subjects and is complete. NACP#12 was a 51 year old female and presented with a 10x7 cm invasive ductal and lobular carcinoma which had a triple negative receptor status in her left breast. The patient was treated with doxorubicin and cyclophosphamide bi-weekly for 8 weeks followed by weekly treatments of low-dose paclitaxel. Subsequently, we performed 14 optical measurements, one pre-treatment measurement, and a measurement prior to each of 13 chemotherapy treatments. For week 12, the optical data were corrupted due to instrumentation failure, resulting in a total of 13 optical measurements presented here. She is classified as a non-responder per the definition in section 3.2.2 (tumor size reduced by < 50%).

5.2.2. Dynamic, dual-breast NIRS system.

The components of the system used here are identical to those described in Section 2.2.1. However, the configuration has been altered to allow for bilateral dynamic measurements. Rather than using the multiplexed detection system for off-axis detection to allow for depth

sensitivity, we use it to allow for simultaneous measurements of hemodynamics in both breasts at a single point. Following is a brief description of this setup.

A system block-diagram is presented in Figure 5.1. Light from a quartz-tungsten-halogen (QTH) lamp (Model No. 66635, Newport Instruments, Irvine, CA) was band pass filtered by a spectral filter (Model YSC1100, Asahi Spectra USA, Torrance, CA) to a 340 – 1130 nm spectral bandwidth and delivered to each breast by way of two 2.5 mm diameter source optical fiber bundles (S_1 and S_2). Two 6.5 mm thick polycarbonate plates slightly compress and stabilize both breasts. Two 2.5 mm diameter detector optical fiber bundles, D_1 and D_2 were placed coaxially to the source fibers S_1 and S_2, respectively.

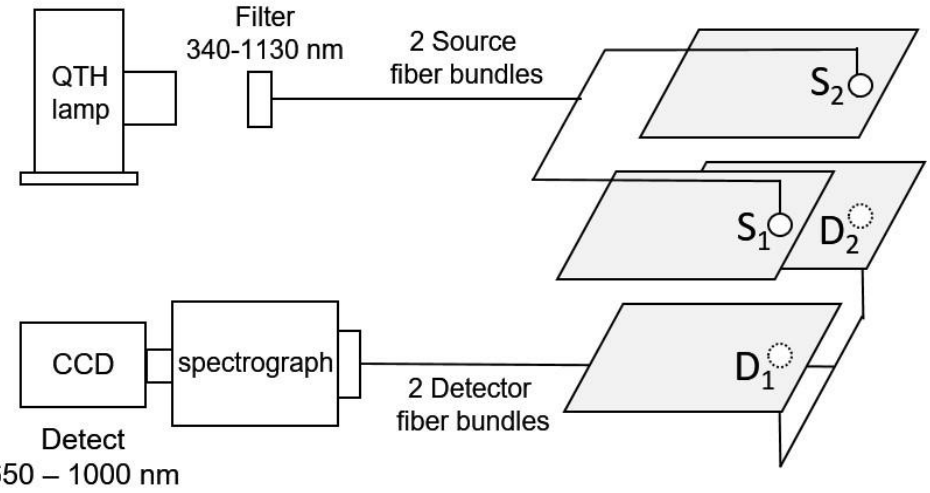

Figure 5.1: System block diagram. A quartz-tungsten-halogen (QTH) lamp is filtered to 340 – 1130 nm and delivered to two source locations (S_1 and S_2) one for each breast. Two detector fibers (D_1 and D_2) placed coaxially to the sources collect the transmitted light and deliver it to a spectrograph where a CCD recovers the transmitted intensity from 650 – 1000 nm for each fiber simultaneously. Each source-detector pair is adjustable, so they remain coaxial but can translate in the 2D measurement plane.

Patients undergoing NAC typically have large (>2 cm) tumors providing significant contrast. A spatial intensity image from the source-detector pair measuring the cancerous breast was retrieved using the protocol described in section 2.2.1. However, rather than

using four fibers to achieve depth sensitivity only a single on-axis image was acquired. The poor spatial resolution of diffuse optics limits our capability to identify the tumor location with high accuracy, however the large tumors associated with NAC still afford sensitivity to the hemodynamics with an inaccurate probe placement. To place the source-detector pair used to measure the cancerous breast as accurately as possible, we used the location of the tumor identified in X-ray mammograms *a priori*. Since cancer has higher blood content and subsequently higher absorption than the surrounding healthy tissue we use the intensity minimum in the corresponding quadrant of the intensity image as a guide to place the source-detector pair. The detector fibers were then coupled into a spectrograph and transmitted intensity data for each breast (650 – 1000 nm) were recorded at up to 5 Hz simultaneously using the same CCD camera (Model Pixis400, Princeton Instruments, Princeton, NJ).

The transmitted intensity measurements over time were translated to $\Delta[Hb](t)$ and $\Delta[HbO_2](t)$ using the modified Beer-Lambert law as described in section 2.2.4. The plate separation was adjusted to stabilize both breasts while limiting any mechanical compression resulting from the plates. To maintain the compression level between measurements the plate separation was kept constant through the course of chemotherapy for each patient. For NACP#11, due to the patients smaller breasts (plate separation = 40 mm) placing both breasts such that the detectors were sampling the same tissue region was challenging. Some measurements were contaminated with motion artifacts due to the plates not being able to stabilize the breast without significant compression.

5.2.3. Protocol for inducing coherent hemodynamics

Similar to the protocol described in section 4.2.2, we induce systemic oscillations in mean arterial pressure using pneumatic thigh-cuffs on both legs. NACP#12 previously had a stent placed in her right calf, and only one thigh-cuff on the left leg was used as a precaution. In previous studies, we have found that single cuffs are sufficient to induce systemic oscillations, however the magnitude of oscillations in mean arterial pressure were smaller than with two cuffs. NACP#13 had previously been diagnosed with polio. While polio, primarily affects nerve function, the inability of the patient to bend her right leg led to, in some cases, motion of the cuff during inflation causing inconsistent pressure. In this study to limit the time of the measurement and to test the hypothesis that we can see a phase difference between oscillations in [HbO_2] and [Hb] we induce oscillations at a single frequency 0.059 Hz. This frequency was chosen because it was slow enough that the pump used in the clinical setting could refill and provide consistent pressure. Note that in a realistic application, a direct line of air pressure would eliminate this issue, but this was not available for these measurements.

5.2.4. Data analysis

The methods used for data analysis are described in section 4.2.3. Specifically, we use the Hilbert transform to derive the analytical signal at the induced frequency and extract the amplitude and phase of oscillations in Δ[HbO_2] and Δ[Hb], as well as their phasors **D** and **O**. Additionally, since we do not have access to mean arterial pressure data during these measurements, we use the PSI based on **D** and **O**, $PSI_{\mathbf{D},\mathbf{O}}$, to identify those induced oscillations that are coherent (as described in section 4.2.5). For each infusion time point we collect an optical measurement of arg(**D**)−arg(**O**) as well as |**D**|/|**O**|.

5.3. Results and Discussion

The purpose of this study was to identify differences in the hemodynamics measured with NIRS associated with cancerous tissue versus healthy tissue. Ultimately, we found that no phase difference between [Hb] and [HbO_2] was measured in the cancerous tissue, resembling the same hemodynamic features as the healthy tissue (Figure 5.2). Namely, no consistent trends were produced by using induced oscillations to measure hemodynamics.

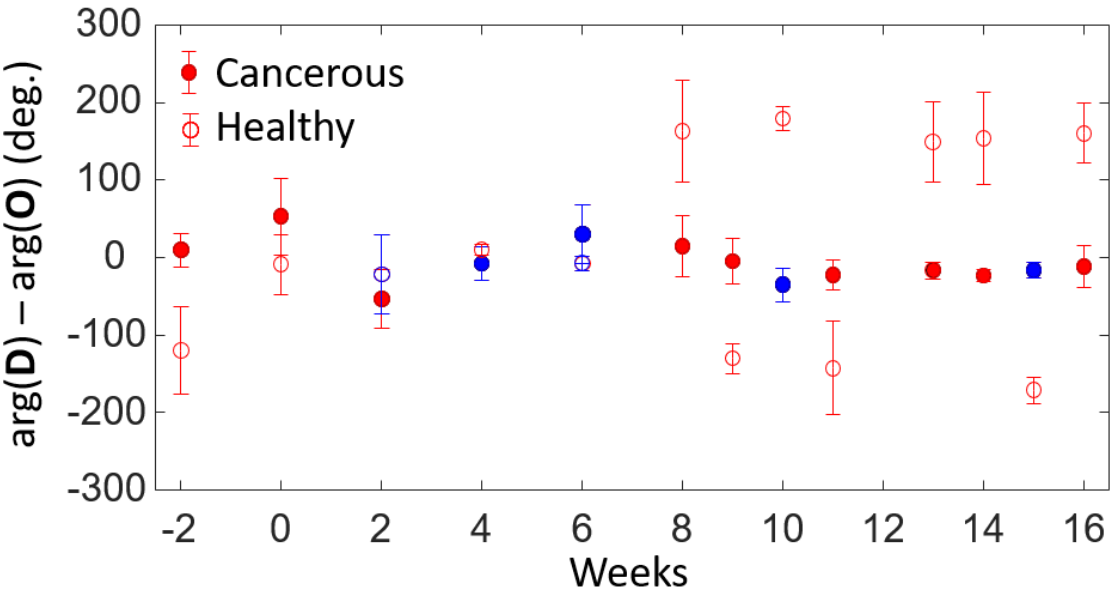

Figure 5.2: Phase relationship between **D** and **O** for NACP#12 at 0.059 Hz for the cancerous (closed circles) and healthy (open circles) breasts. The blue points represent those measurements that passed the PSI threshold. A total of 4 measurements for the cancerous breast and only 2 measurements for the healthy breast passed the PSI threshold during these experiments.

The initial challenge in this study, as was reported also in Chapter 4:, is that the pneumatic thigh cuffs did not always produce robust oscillations. We found that only 4 out of 13 measurements produced coherent oscillations that passed the PSI threshold for the cancerous breast and only 2 out of 13 oscillations passed the PSI threshold for the healthy breast. For this NACP#12 it is possible that using only one thigh cuff caused poor results, but the results from the other two subjects (even with incomplete data sets) were not

significantly better. Which points to the need for understanding the propagation of the mean arterial pressure signal that results from the thigh cuff oscillations. It is possible that the particularly low incidence of significant oscillations in the case of patients undergoing chemotherapy is a result of chemotherapy disrupting the vascular function to attack tumor growth. While one would think this would only affect the cancerous breast, we have previously shown (in Chapter 3) the significance of measurements done on the contralateral breast as chemotherapy has broad systemic effects.

In Chapter 4: we point to the fact that inherent variability in our measurements of arg(**D**)−arg(**O**) between subjects can depend on varied physiological states and anatomical differences, but in the breast measurements we see little variability in that when arg(**D**)−arg(**O**) is synchronous there is no phase difference. Our interpretation of in phase oscillations between **D** and **O**, as reported in the healthy breast also, is that these oscillations result primarily due to blood volume changes.[53] Our initial hypothesis was that the stiffer breast tissue resulting from breast cancer would result in limiting blood volume changes and result in measurable changes in blood flow. It is possible that when using the modified Beer-Lambert law, since we treat the measured tissue as a homogenous medium, we include large portions of both healthy and cancerous tissue. In this sense, while we could be sensitive to smaller oscillations in blood flow, they are still dominated by the surrounding oscillations in blood volume.

5.4. Conclusions

In this study we monitored NACPs using a dynamic breast imaging system adapted from the system designed in Chapter 2. The results show that in a transmission geometry using a single source-detector pair we were unable to measure a phase difference between [Hb]

and [HbO_2] oscillations in the cancerous or healthy breast. More importantly, we realize that the measurements as done here were not particularly robust. We ran into clinical challenges that affected our protocol's efficacy and need to be rectified if this question is to be better investigated. It is possible that using multiple source detector distances for each measurement could provide some depth information to separate out oscillations from healthy versus cancerous tissue.

Chapter 6: Summary and future directions

6.1. Optical characteristics of breast cancer.

Over the past 20 years, optical measurements of patients with breast cancer, and those undergoing neoadjuvant chemotherapy have been widely reported. Namely, a consistent increase in the concentration of total hemoglobin [HbT] has been reported by many groups irrespective of the imaging modalities, geometries, and instrument designs.[3] The basis for an increase in total hemoglobin concentration in the presence of cancer is a result of accelerated angiogenesis—total blood volume in the cancer region increases from the growth of new vessels. Hemoglobin saturation (SO2), however, relates to the balance between tissue demand for oxygen dictated by metabolic rate, and the supply of oxygen determined by the blood flow.

While [HbT] has been consistently reported to increase, hemoglobin saturation has been reported by numerous groups to increase, decrease, or stay the same. Some studies have reported decreased SO2 within tumors[4,8], whereas others have found no significant difference in the SO2 of cancerous and healthy tissue.[6,29,92,93] These discrepancies may rule out SO2 as a robust NIRS cancer biomarker. It is possible that different cancer types, stages, and locations may result in different SO2 contrasts measured with NIRS. Each of these factors, which differ across studies, may contribute to an inconsistent trend in how SO2 in all cancers compares to healthy tissue.

Additionally, groups have reported on the capability to of NIRS measurements to identify biomarkers associated with chemotherapy response. A consistently reported result is that the total concentration of hemoglobin in cancerous breast tissue, [HbT], decreases by a large amount (as much as 60%) in patients who respond to therapy, whereas it

decreases by a smaller amount, stays constant, or increases in patients who do not respond to therapy. It was also reported that systemic effects of neoadjuvant chemotherapy account for [HbT] changes in the healthy breast as well as in the cancerous breast. The application of NIRS in monitoring patients undergoing chemotherapy takes full advantage of the safe, non-invasive, and cost-effective nature of optical mammography. While, static changes in the absolute blood volume provide information about the structural changes associated with breast cancer, the dynamics of how these tissues function may provide more specific optical measurements.

6.2. Developing NIRS as a clinical tool for breast cancer.

Although groups have reproduced similar results showing that NIRS measurements can distinguish specific physiologically relevant changes associated with breast cancer, the clinical implementation of optical measurements is still not within reach. Changes in [HbT] and SO2 show that NIRS is capable of distinguishing changes on a group level, however the specificity required to either diagnose or characterize patients on an individual level has yet to be reported. We show an initial attempt at using NIRS to classify patients as responders or non-responders to chemotherapy using our CRI, however this is merely a proof-of-concept. In a real classification scheme a much larger data set is needed to have a training set and a test set for classification.

The challenge moving forward is collecting robust data on a large enough population to begin providing clinically useful conclusions. Tromberg et al. report the first multi-center clinical trail using NIRS to monitor patient response to neoadjuvant chemotherapy. Tromberg et al. collected data on 60 subjects of which 34 were analyzed, and show that while their tumor optical index (TOI), a combination of the different optical

parameters measured, was sensitive to the changes associated with chemotherapy.[79] This was the first study, where a standardized optical breast imaging platform was evaluated to characterize chemotherapy. While Tromberg et al. were successful in showing that NIRS is capable of characterizing the changes associated with chemotherapy treatment, they were unable to develop a diagnostic endpoint to determine if patients were complete responders. Similarly, Sajjadi et al recruit 30 patients undergoing neoadjuvant chemotherapy and show in 13 patients that the dynamic response to manual compression of the breast can distinguish responding and non-responding patients.[151] While, Sajjadi et al show they are sensitive to differences in tumor function based on their dynamics measured using NIRS. However, they were unable to individually characterize the response of each patient.

Although NIRS has the capability to measure changes associated with cancer or even treatment with chemotherapy, the common issue associated with developing a robust clinical endpoint using NIRS is the practicality of its application. In each of the large studies reported above, nearly half of the subjects were discarded due to technical reasons. These reasons may be due to instrument malfunction, measurement time, patient compliance or poor quality of data.[79,151] Since the number of patients undergoing neoadjuvant chemotherapy is small, completing large population based study is highly dependent on robust methods of data collection. Developing a high-fidelity system, that is well tested, and collects the relevant optical information with minimal intrusion to the clinical workflow of doctors, nurses, and the patient is critical to moving forward. Teng et al have recently developed a wearable optical probe that can conform to the tissue it measures and provide robust measurements of [Hb] or [HbO_2] with minimal disruption to the patient.[152] While this instrument has yet to be tested on the breast, instruments such as

this, address the more pressing issue of acquiring fast, reliable, and robust measurements which will improve patient and physician compliance with research studies. The combination of being able to implement robust measurement schemes and avoid disrupting clinical workflow provides the basis to collect the large sample sizes needed to build a classification scheme based on optical parameters for chemotherapy response, or even for breast cancer diagnosis.

6.3. Applying machine learning to optical data.

As the capability to collect large data sets improve it is only logical to take into account the capabilities of machine learning and its advantages for understanding optical data in medicine. Machine learning is the study of computer algorithms which can learn complex relationships or patterns from empirical data and make accurate decisions.[153] Machine learning algorithms identify complex patterns automatically and has been researched in applications on radiology data such as conventional radiographs, CT, MRI, and PET images.[154] For optical data, while the relationship between hemoglobin changes and cancer changes are well understood in their functional relationship, differences in cancer subtype, treatment type, and patient history are not well understood. While we can be sure that changes in the concentration of hemoglobin in the breast is linked to changes in cancer, with large data sets a machine learning algorithm may provide more insight into specific trends associated with the many other variables we have access to.

References

1. C. L. Christiansen and F. Wang, “Predicting the Cumulative Risk of False-Positive Mammograms,” J. Natl. Cancer Inst. **92**(20), 1657–1666 (2000) [doi:10.1093/jnci/92.20.1657].

2. J. G. Elmore et al., “Ten-year risk of false positive screening mammograms and clinical breast examinations,” N. Engl. J. Med. **338**(16), 1089–1096 (1998).

3. D. Grosenick et al., “Review of optical breast imaging and spectroscopy,” J. Biomed. Opt. **21**(9), 91311, International Society for Optics and Photonics (2016) [doi:10.1117/1.JBO.21.9.091311].

4. V. Ntziachristos et al., “MRI-guided diffuse optical spectroscopy of malignant and benign breast lesions,” Neoplasia. **4**(1522–8002), 347–354 (2002).

5. B. Chance et al., “Breast cancer detection based on incremental biochemical and physiological properties of breast cancers: A six-year, two-site Study1,” Acad. Radiol. **12**(8), 925–933 (2005).

6. D. Grosenick et al., “Time-domain scanning optical mammography: I. Recording and assessment of mammograms of 154 patients.,” Phys. Med. Biol. **50**(11), 2429–2449 (2005).

7. J. Wang et al., “Near-infrared tomography of breast cancer hemoglobin, water, lipid, and scattering using combined frequency domain and cw measurement.,” Opt. Lett. **35**(1), 82–84 (2010).

8. P. G. Anderson et al., “Broadband optical mammography: chromophore concentration and hemoglobin saturation contrast in breast cancer.,” PLoS One **10**(3), e0117322 (2015) [doi:10.1371/journal.pone.0117322].

9. S. Fantini and A. Sassaroli, “Near-infrared optical mammography for breast cancer detection with intrinsic contrast.,” Ann. Biomed. Eng. **40**(2), 398–407 (2012) [doi:10.1007/s10439-011-0404-4].

10. K. C. Oeffinger et al., “Breast Cancer Screening for Women at Average Risk,” JAMA **314**(15), 1599, American Medical Association (2015) [doi:10.1001/jama.2015.12783].

11. C. H. Lee et al., “Breast Cancer Screening With Imaging: Recommendations From the Society of Breast Imaging and the ACR on the Use of Mammography, Breast MRI, Breast Ultrasound, and Other Technologies for the Detection of Clinically Occult Breast Cancer,” JACR **7**, 18–27 (2010) [doi:10.1016/j.jacr.2009.09.022].

12. C. Lehman, R. S.-J. of the N. C. Cancer, and undefined 2009, “The role of MRI in breast cancer screening,” jnccn.org.

13. M. Cutler, “Transillumination as an aid in the diagnosis of breast lesions,” Surgery, Gynecol. Obstet. **48**(6), 721–729 (1929).

14. R. H. Mole, “The sensitivity of the human breast to cancer induction by ionizing radiation,” Br. J. Radiol. **51**(606), 401–405, The British Institute of Radiology (1978) [doi:10.1259/0007-1285-51-606-401].

15. V. Marshall, D. C. Williams, and K. D. Smith, “Diaphanography as a means of detecting breast cancer.,” Radiology **150**(2), 339–343 (1984) [doi:10.1148/radiology.150.2.6691086].

16. B. Drexler, J. L. Davis, and G. Schofield, “Diaphanography in the diagnosis of breast cancer.,” Radiology **157**(1), 41–44 (1985) [doi:10.1148/radiology.157.1.4034975].

17. D. Watmough, “Diaphanography: mechanism responsible for the images,” Acta. Radiol. Oncol. **21**(1), 11–15 (1982).

18. B. Monsees, J. M. Destouet, and W. G. Totty, “Light scanning versus mammography in breast cancer detection.,” Radiology **163**(2), 463–465 (1987) [doi:10.1148/radiology.163.2.3562828].

19. G. A. Navarro, “Contrast in diaphanography of the breast,” Med. Phys. **15**(2), 181, American Association of Physicists in Medicine (1988) [doi:10.1118/1.596249].

20. D. Contini et al., “Photon migration through a turbid slab described by a model based on diffusion approximation. I. Theory,” Appl. Opt. **36**(19), 4587–4599, Optical Society of America (1997) [doi:10.1364/AO.36.004587].

21. B. Chance et al., “Breast cancer detection based on incremental biochemical and physiological properties of breast cancers: A six-year, two-site Study1,” Acad. Radiol. **12**(8), 925–933 (2005).

22. S. Arridge, “Optical tomography in medical imaging,” Inverse Probl. **15**, R41-93 (1999).

23. Y. Yu et al., “Near-infrared spectral imaging of the female breast for quantitative oximetry in optical mammography,” Appl. Opt. **48**(10), D225, OSA (2009) [doi:10.1364/AO.48.00D225].

24. B. W. Pogue et al., “Quantitative hemoglobin tomography with diffuse near-infrared spectroscopy: pilot results in the breast.,” Radiology **218**(1), 261–266, Radiological Society of North America (2001) [doi:10.1148/radiology.218.1.r01ja51261].

25. A. Torricelli et al., “Use of a nonlinear perturbation approach for in vivo breast lesion characterization by multiwavelength time-resolved optical mammography,” Opt. Express **11**(8), 853, OSA (2003) [doi:10.1364/OE.11.000853].

26. D. Grosenick, A. Kummrow, and R. Macdonald, “Evaluation of higher-order time-domain perturbation theory of photon diffusion on breast-equivalent phantoms and optical mammograms,” Phys. Rev. E **76**(6), 61908 (2007).

27. A. E. Cerussi et al., “Spectroscopy enhances the information content of optical mammography.,” J. Biomed. Opt. **7**(1), 60–71, International Society for Optics and Photonics (2002) [doi:10.1117/1.1427050].

28. A. E. Cerussi et al., “Sources of absorption and scattering contrast for near-infrared optical mammography.,” Acad. Radiol. **8**(3), 211–218 (2001) [doi:10.1016/S1076-6332(03)80529-9].

29. A. Cerussi et al., “In vivo absorption, scattering, and physiologic properties of 58 malignant breast tumors determined by broadband diffuse optical spectroscopy.,” J. Biomed. Opt. **11**(4), 44005, International Society for Optics and Photonics (2006) [doi:10.1117/1.2337546].

30. A. Bassi, A. Farina, and C. D’Andrea, “Portable, large-bandwidth time-resolved system for diffuse optical spectroscopy,” Opt. Express **15**(22), 14482–14487 (2007).

31. P. Taroni et al., “Seven-wavelength time-resolved optical mammography extending beyond 1000 nm for breast collagen quantification.,” Opt. Express **17**(18), 15932–15946, Optical Society of America (2009) [doi:10.1364/OE.17.015932].

32. J. P. Culver et al., “Three-dimensional diffuse optical tomography in the parallel plane transmission geometry: Evaluation of a hybrid frequency domain/continuous wave clinical system for breast imaging,” Med. Phys. **30**(2), 235, American Association of Physicists in Medicine (2003) [doi:10.1118/1.1534109].

33. M. L. Flexman et al., “Digital optical tomography system for dynamic breast imaging,” J. Biomed. Opt. **16**(7), 76014 (2011).

34. Q. Fang, S. Carp, and J. Selb, “Combined optical imaging and mammography of the healthy breast: optical contrast derived from breast structure and compression,” IEEE Trans. Med. Imaging **28**(1), 30–42 (2009).

35. D. Grosenick et al., “Time-Domain Optical Mammography: Initial Clinical Results on Detection and Characterization of Breast Tumors,” Appl. Opt. **42**(16), 3170, OSA (2003) [doi:10.1364/AO.42.003170].

36. B. J. Tromberg et al., “Imaging in breast cancer: diffuse optics in breast cancer: detecting tumors in pre-menopausal women and monitoring neoadjuvant

chemotherapy.," Breast Cancer Res. **7**(6), 279–285 (2005) [doi:10.1186/bcr1358].

37. S. R. Arridge and W. R. B. Lionheart, "Nonuniqueness in diffusion-based optical tomography," Opt. Lett. **23**(11), 882–884, OSA (1998) [doi:10.1364/OL.23.000882].

38. B. Pogue et al., "Instrumentation and design of a frequency-domain diffuse optical tomography imager for breast cancer detection," Opt. Express **1**(13), 391, OSA (1997) [doi:10.1364/OE.1.000391].

39. T. Durduran et al., "Bulk optical properties of healthy female breast tissue.," Phys. Med. Biol. **47**(16), 2847–2861 (2002).

40. J. M. Kainerstorfer et al., "Depth discrimination in diffuse optical transmission imaging by planar scanning off-axis fibers: initial applications to optical mammography.," PLoS One **8**(3), e58510 (2013) [doi:10.1371/journal.pone.0058510].

41. D. Grosenick et al., "Concentration and oxygen saturation of haemoglobin of 50 breast tumours determined by time-domain optical mammography," Phys. Med. Biol. **49**(7), 1165–1181 (2004) [doi:10.1088/0031-9155/49/7/006].

42. D. Grosenick et al., "A multichannel time-domain scanning fluorescence mammograph: performance assessment and first in vivo results.," Rev. Sci. Instrum. **82**(2), 24302, AIP Publishing (2011) [doi:10.1063/1.3543820].

43. N. Liu, A. Sassaroli, and S. Fantini, "Two-dimensional phased arrays of sources and detectors for depth discrimination in diffuse optical imaging.," J. Biomed. Opt. **10**(5), 51801, International Society for Optics and Photonics (2005) [doi:10.1117/1.2085172].

44. S. A. Carp et al., "Dynamic functional and mechanical response of breast tissue to compression.," Opt. Express **16**(20), 16064–16078 (2008).

45. C. Schmitz et al., "Design and implementation of dynamic near-infrared optical tomographic imaging instrumentation for simultaneous dual-breast measurements," Appl. Opt. **44**(11), 2140–2153 (2005).

46. M. L. Flexman et al., "Optical biomarkers for breast cancer derived from dynamic diffuse optical tomography," J. Biomed. Opt. **18**(9), 96012 (2013) [doi:10.1117/1.JBO.18.9.096012].

47. S. Carp et al., "Hemodynamic signature of breast cancer under fractional mammographic compression using a dynamic diffuse optical tomography system," Biomed. Opt. Express **4**(12), 2911–2924 (2013).

48. N. Shah et al., “Noninvasive functional optical spectroscopy of human breast tissue,” Proc. Natl. Acad. Sci. U. S. A. **98**(8), 4420–4425 (2001).

49. Q. Zhu, N. Chen, and S. H. Kurtzman, “Imaging tumor angiogenesis by use of combined near-infrared diffusive light and ultrasound,” Opt. Lett. **28**(5), 337, OSA (2003) [doi:10.1364/OL.28.000337].

50. D. T. Delpy et al., “Estimation of optical pathlength through tissue from direct time of flight measurement.,” Phys. Med. Biol. **33**(12), 1433–1442 (1988) [doi:10.1088/0031-9155/33/12/008].

51. M. Kohl et al., “Determination of the wavelength dependence of the differential pathlength factor from near-infrared pulse signals,” Phys. Med. Biol. **43**(6), 1771–1782 (1998).

52. S. Prahl, “Optical absorption of hemoglobin,” Oregon Medical Laser Center, Portland, OR, 2002, <http://omlc.org/spectra/hemoglobin/summary.html> (accessed 10 October 2015).

53. K. T. Tgavalekos et al., “Blood-pressure-induced oscillations of deoxy- and oxyhemoglobin concentrations are in-phase in the healthy breast and out-of-phase in the healthy brain,” J. Biomed. Opt. **21**(10), 101410, International Society for Optics and Photonics (2016) [doi:10.1117/1.JBO.21.10.101410].

54. D. B. Jakubowski et al., “Monitoring neoadjuvant chemotherapy in breast cancer using quantitative diffuse optical spectroscopy: a case study.,” J. Biomed. Opt. **9**(1), 230–238 (2004) [doi:10.1117/1.1629681].

55. D. Mauri, N. Pavlidis, and J. P. A. Ioannidis, “Neoadjuvant versus adjuvant systemic treatment in breast cancer: A meta-analysis,” J. Natl. Cancer Inst. **97**(3), 188–194 (2005) [doi:10.1093/jnci/dji021].

56. P. Rastogi et al., “Preoperative chemotherapy: Updates of national surgical adjuvant breast and bowel project protocols B-18 and B-27,” J. Clin. Oncol. **26**(5), 778–785 (2008) [doi:10.1200/JCO.2007.15.0235].

57. G. Von Minckwitz et al., “Definition and impact of pathologic complete response on prognosis after neoadjuvant chemotherapy in various intrinsic breast cancer subtypes,” J. Clin. Oncol. **30**(15), 1796–1804 (2012) [doi:10.1200/JCO.2011.38.8595].

58. V. Guarneri et al., “Prognostic value of pathologic complete response after primary chemotherapy in relation to hormone receptor status and other factors.,” J. Clin. Oncol. **24**(7), 1037–1044 (2006) [doi:10.1200/JCO.2005.02.6914].

59. S. P. Gampenrieder, G. Rinnerthaler, and R. Greil, “Neoadjuvant chemotherapy and

targeted therapy in breast cancer: Past, present, and future," in Journal of Oncology (2013) [doi:10.1155/2013/732047].

60. A. B. Chagpar et al., "Accuracy of physical examination, ultrasonography, and mammography in predicting residual pathologic tumor size in patients treated with neoadjuvant chemotherapy.," Ann. Surg. **243**(2), 257–264 (2006) [doi:10.1097/01.sla.0000197714.14318.6f].

61. D. Groheux et al., "Early Metabolic Response to Neoadjuvant Treatment: FDG PET/CT Criteria according to Breast Cancer Subtype.," Radiology **277**(2), 358–371 (2015) [doi:10.1148/radiol.2015141638].

62. C. E. Loo et al., "Magnetic resonance imaging response monitoring of breast cancer during neoadjuvant chemotherapy: Relevance of Breast Cancer Subtype," J. Clin. Oncol. **29**(6), 660–666 (2011) [doi:10.1200/JCO.2010.31.1258].

63. R. Choe et al., "Diffuse optical tomography of breast cancer during neoadjuvant chemotherapy: a case study with comparison to MRI.," Med. Phys. **32**(4), 1128–1139 (2005) [doi:10.1118/1.1869612].

64. D. Roblyer et al., "Optical imaging of breast cancer oxyhemoglobin flare correlates with neoadjuvant chemotherapy response one day after starting treatment.," Proc. Natl. Acad. Sci. U. S. A. **108**(35), 14626–14631 (2011) [doi:10.1073/pnas.1013103108].

65. A. Cerussi et al., "Predicting response to breast cancer neoadjuvant chemotherapy using diffuse optical spectroscopy," Proc. Natl. Acad. Sci. U. S. A. **104**(10), 4014–4019 (2007) [doi:10.1073/pnas.0611058104].

66. C. Zhou et al., "Diffuse optical monitoring of blood flow and oxygenation in human breast cancer during early stages of neoadjuvant chemotherapy," J. Biomed. Opt. **12**(5), 51903 (2007) [doi:10.1117/1.2798595].

67. O. Falou et al., "Diffuse optical spectroscopy evaluation of treatment response in women with locally advanced breast cancer receiving neoadjuvant chemotherapy.," Transl. Oncol. **5**(4), 238–246 (2012) [doi:10.1593/tlo.11346].

68. W. T. Tran et al., "Multiparametric monitoring of chemotherapy treatment response in locally advanced breast cancer using quantitative ultrasound and diffuse optical spectroscopy," Oncotarget **7**(15), 19762–19780 (2016) [doi:10.18632/oncotarget.7844].

69. Q. Zhu et al., "Noninvasive monitoring of breast cancer during neoadjuvant chemotherapy using optical tomography with ultrasound localization," Neoplasia **10**(10), 1028–1040 (2008) [doi:10.1593/neo.08602].

70. A. E. Cerussi et al., “Diffuse optical spectroscopic imaging correlates with final pathological response in breast cancer neoadjuvant chemotherapy.,” Philos. Trans. A. Math. Phys. Eng. Sci. **369**(1955), 4512–4530 (2011) [doi:10.1098/rsta.2011.0279].

71. Q. Zhu et al., “Breast cancer: assessing response to neoadjuvant chemotherapy by using US-guided near-infrared tomography.,” Radiology **266**(2), 433–442 (2013) [doi:10.1148/radiol.12112415].

72. S. Jiang et al., “Evaluation of breast tumor response to neoadjuvant chemotherapy with tomographic diffuse optical spectroscopy: case studies of tumor region-of-interest changes.,” Radiology **252**(2), 551–560 (2009) [doi:10.1148/radiol.2522081202].

73. H. Soliman et al., “Functional imaging using diffuse optical spectroscopy of neoadjuvant chemotherapy response in women with locally advanced breast cancer,” Clin. Cancer Res. **16**(9), 2605–2614 (2010) [doi:10.1158/1078-0432.CCR-09-1510].

74. B. E. Schaafsma et al., “Optical mammography using diffuse optical spectroscopy for monitoring tumor response to neoadjuvant chemotherapy in women with locally advanced breast cancer.,” Clin. Cancer Res. **21**(3), 577–584 (2015) [doi:10.1158/1078-0432.CCR-14-0736].

75. M. G. Pakalniskis et al., “Tumor angiogenesis change estimated by using diffuse optical spectroscopic tomography: demonstrated correlation in women undergoing neoadjuvant chemotherapy for invasive breast cancer?,” Radiology **259**(2), 365–374 (2011) [doi:10.1148/radiol.11100699].

76. D. R. Busch et al., “Optical malignancy parameters for monitoring progression of breast cancer neoadjuvant chemotherapy.,” Biomed. Opt. Express **4**(1), 105–121 (2013) [doi:10.1364/BOE.4.000105].

77. S. Jiang et al., “Predicting Breast Tumor Response to Neoadjuvant Chemotherapy with Diffuse Optical Spectroscopic Tomography prior to Treatment,” Clin. Cancer Res. **20**(23), 6006–6015 (2014) [doi:10.1158/1078-0432.CCR-14-1415].

78. J. E. Gunther et al., “Combined dynamic and static optical tomography for prediction of treatment outcome in breast cancer patients,” in SPIE Proceedings, p. 953811 (2015).

79. B. J. Tromberg et al., “Predicting Responses to Neoadjuvant Chemotherapy in Breast Cancer: ACRIN 6691 Trial of Diffuse Optical Spectroscopic Imaging.,” Cancer Res. **76**(20), 5933–5944, American Association for Cancer Research (2016) [doi:10.1158/0008-5472.CAN-16-0346].

80. S. Ueda et al., “Baseline tumor oxygen saturation correlates with a pathologic complete response in breast cancer patients undergoing neoadjuvant chemotherapy,” Cancer Res. **72**(17), 4318–4328 (2012) [doi:10.1158/0008-5472.CAN-12-0056].

81. Q. Zhu et al., “Pathologic response prediction to neoadjuvant chemotherapy utilizing pretreatment near-infrared imaging parameters and tumor pathologic criteria.,” Breast Cancer Res. **16**(5), 456 (2014) [doi:10.1186/s13058-014-0456-0].

82. A. E. Cerussi et al., “Frequent Optical Imaging during Breast Cancer Neoadjuvant Chemotherapy Reveals Dynamic Tumor Physiology in an Individual Patient,” Acad. Radiol. **17**(8), 1031–1039 (2010) [doi:10.1016/j.acra.2010.05.002].

83. K. N. Ogston et al., “A new histological grading system to assess response of breast cancers to primary chemotherapy: Prognostic significance and survival,” Breast **12**(5), 320–327 (2003) [doi:10.1016/S0960-9776(03)00106-1].

84. S. Rodenhuis et al., “A simple system for grading the response of breast cancer to neoadjuvant chemotherapy,” Ann Oncol **21**(3), 481–487 (2010) [doi:10.1093/annonc/mdp348].

85. P. G. P. G. Anderson et al., “Broadband optical mammography: Breast tissue thickness compensation algorithm.,” in International Society for Optics and Photonics **9319**, p. 93190L (2015) [doi:10.1117/12.2079200].

86. K. Madsen, H. Nielsen, and O. Tingleff, “Methods for Non-Linear Least Squares Problems.” (2004).

87. D. Grosenick et al., “Time-domain scanning optical mammography: II. Optical properties and tissue parameters of 87 carcinomas.,” Phys. Med. Biol. **50**(11), 2451–2468 (2005) [doi:10.1088/0031-9155/50/11/002].

88. Q. Zhu et al., “Utilizing optical tomography with ultrasound localization to image heterogeneous hemoglobin distribution in large breast cancers,” Neoplasia **7**(3), 263–270 (2005) [doi:10.1593/neo.04526].

89. J. E. Groopman and L. M. Itri, “Chemotherapy-induced anemia in adults: incidence and treatment.,” J. Natl. Cancer Inst. **91**(19), 1616–1634 (1999) [doi:10.1093/jnci/91.19.1616].

90. T. D. O’Sullivan et al., “Optical imaging correlates with magnetic resonance imaging breast density and reveals composition changes during neoadjuvant chemotherapy.,” Breast Cancer Res. **15**(1), R14 (2013) [doi:10.1186/bcr3389].

91. J. M. Cochran et al., “Tissue Oxygen Saturation Predicts Response to Breast Cancer Neoadjuvant Chemotherapy within 10 Days,” in Biophotonics Congress:

Biomedical Optics Congress 2018 (Microscopy/Translational/Brain/OTS), p. OTh4D.3, OSA, Washington, D.C. (2018) [doi:10.1364/OTS.2018.OTh4D.3].

92. R. Choe et al., "Differentiation of benign and malignant breast tumors by in-vivo three-dimensional parallel-plate diffuse optical tomography.," J Biomed Opt **14**(2), 24020 (2009) [doi:10.1117/1.3103325].

93. L. Spinelli, A. Torricelli, and A. Pifferi, "Characterization of female breast lesions from multi-wavelength time-resolved optical mammography," Phys. Med. Biol. **50**(11), 2489–2502 (2005).

94. S. Carraresi et al., "Accuracy of a perturbation model to predict the effect of scattering and absorbing inhomogeneities on photon migration.," Appl. Opt. **40**(25), 4622–4632 (2001) [doi:10.1364/AO.40.004622].

95. J. Duch et al., "18F-FDG PET/CT for early prediction of response to neoadjuvant chemotherapy in breast cancer," Eur. J. Nucl. Med. Mol. Imaging **36**(10), 1551–1557 (2009) [doi:10.1007/s00259-009-1116-y].

96. J. Delille et al., "Invasive Ductal Breast Carcinoma Response to Neoadjuvant Chemotherapy: Noninvasive Monitoring with Functional MR Imaging—Pilot Study 1," Radiology **228**(1), 63–69 (2003).

97. M. D. Pickles et al., "Role of dynamic contrast enhanced MRI in monitoring early response of locally advanced breast cancer to neoadjuvant chemotherapy," Breast Cancer Res. Treat. **91**(1), 1–10 (2005) [doi:10.1007/s10549-004-5819-2].

98. C. Hayes, A. R. Padhani, and M. O. Leach, "Assessing changes in tumour vascular function using dynamic contrast-enhanced magnetic resonance imaging," NMR Biomed. **15**(2), 154–163 (2002) [doi:10.1002/nbm.756].

99. D. A. Mankoff et al., "Changes in blood flow and metabolism in locally advanced breast cancer treated with neoadjuvant chemotherapy.," J. Nucl. Med. **44**(11), 1806–1814 (2003).

100. G. von Minckwitz et al., "Response-guided neoadjuvant chemotherapy for breast cancer.," J. Clin. Oncol. **31**(29), 3623–3630 (2013) [doi:10.1200/JCO.2012.45.0940].

101. H. Obrig et al., "Spontaneous Low Frequency Oscillations of Cerebral Hemodynamics and Metabolism in Human Adults," Neuroimage **12**(6), 623–639, Academic Press (2000) [doi:10.1006/NIMG.2000.0657].

102. R. Zhang et al., "Transfer function analysis of dynamic cerebral autoregulation in humans," Am. J. Physiol. Circ. Physiol. **274**(1), H233–H241, American Physiological SocietyBethesda, MD (1998)

[doi:10.1152/ajpheart.1998.274.1.H233].

103. G. Themelis et al., “Near-infrared spectroscopy measurement of the pulsatile component of cerebral blood flow and volume from arterial oscillations,” J. Biomed. Opt. **12**(1), 14033, International Society for Optics and Photonics (2007) [doi:10.1117/1.2710250].

104. M. Reinhard et al., “Oscillatory cerebral hemodynamics—the macro-vs. microvascular level” (2006) [doi:10.1016/j.jns.2006.07.011].

105. R. Aaslid et al., “Asymmetric dynamic cerebral autoregulatory response to cyclic stimuli,” Stroke **38**(5), 1465–1469 (2007) [doi:10.1161/STROKEAHA.106.473462].

106. R. Cheng et al., “Noninvasive optical evaluation of spontaneous low frequency oscillations in cerebral hemodynamics,” Neuroimage **62**(3), 1445–1454, Academic Press (2012) [doi:10.1016/J.NEUROIMAGE.2012.05.069].

107. J. A. H. R. Claassen, B. D. Levine, and R. Zhang, “Dynamic cerebral autoregulation during repeated squat-stand maneuvers,” J Appl Physiol **106**, 153–160 (2009) [doi:10.1152/japplphysiol.90822.2008].

108. A. A. Birch, G. Neil-Dwyer, and A. J. Murrills, “The repeatability of cerebral autoregulation assessment using sinusoidal lower body negative pressure,” Physiol. Meas **23**(2), 73–83 (2002).

109. M. Czosnyka et al., “An Assessment of Dynamic Autoregulation from Spontaneous Fluctuations of Cerebral Blood Flow Velocity: A Comparison of Two Models, Index of Autoregulation and Mean Flow Index,” Anesth. Analg. **106**(1), 234–239 (2008) [doi:10.1213/01.ane.0000295802.89962.13].

110. M. Jaeger et al., “Continuous assessment of cerebrovascular autoregulation after traumatic brain injury using brain tissue oxygen pressure reactivity*,” Crit. Care Med. **34**(6), 1783–1788 (2006) [doi:10.1097/01.CCM.0000218413.51546.9E].

111. S. K. Piechnik et al., “The Continuous Assessment of Cerebrovascular Reactivity: A Validation of the Method in Healthy Volunteers,” Anesth. Analg. **89**(4), 944 (1999) [doi:10.1213/00000539-199910000-00023].

112. E. W. Lang et al., “Continuous monitoring of cerebrovascular autoregulation: a validation study.,” J. Neurol. Neurosurg. Psychiatry **72**(5), 583–586, BMJ Publishing Group Ltd (2002) [doi:10.1136/JNNP.72.5.583].

113. S. Fantini et al., “Cerebral blood flow and autoregulation: current measurement techniques and prospects for noninvasive optical methods,” Neurophotonics **3**(3), 31411, International Society for Optics and Photonics (2016)

[doi:10.1117/1.NPh.3.3.031411].

114. R. R. Diehl et al., “Phase relationship between cerebral blood flow velocity and blood pressure. A clinical test of autoregulation.,” Stroke **26**(10), 1801–1804, American Heart Association, Inc. (1995) [doi:10.1161/01.STR.26.10.1801].

115. V. E. Pera et al., “Spatial second-derivative image processing: an application to optical mammography to enhance the detection of breast tumors,” J. Biomed. Opt. **8**(3), 517–524 (2003).

116. G. Taga et al., “Spontaneous oscillation of oxy- and deoxy- hemoglobin changes with a phase difference throughout the occipital cortex of newborn infants observed using non-invasive optical topography,” Neurosci. Lett. **282**(1–2), 101–104, Elsevier (2000) [doi:10.1016/S0304-3940(00)00874-0].

117. M. L. M. Pierro et al., “Phase-amplitude investigation of spontaneous low-frequency oscillations of cerebral hemodynamics with near-infrared spectroscopy: a sleep study in human subjects,” Neuroimage **63**(3), 1571–1584, Academic Press (2012) [doi:10.1016/J.NEUROIMAGE.2012.07.015].

118. H. Watanabe et al., “Hemoglobin phase of oxygenation and deoxygenation in early brain development measured using fNIRS.,” Proc. Natl. Acad. Sci. U. S. A. **114**(9), E1737–E1744, National Academy of Sciences (2017) [doi:10.1073/pnas.1616866114].

119. M. L. Pierro et al., “Validation of a novel hemodynamic model for coherent hemodynamics spectroscopy (CHS) and functional brain studies with fNIRS and fMRI.,” Neuroimage **85 Pt 1**, 222–233, Elsevier Inc. (2014) [doi:10.1016/j.neuroimage.2013.03.037].

120. M. L. Pierro et al., “Reduced speed of microvascular blood flow in hemodialysis patients versus healthy controls: a coherent hemodynamics spectroscopy study,” J. Biomed. Opt. **19**(2), 26005, International Society for Optics and Photonics (2014) [doi:10.1117/1.JBO.19.2.026005].

121. S. Fantini, “Dynamic model for the tissue concentration and oxygen saturation of hemoglobin in relation to blood volume, flow velocity, and oxygen consumption: Implications for functional neuroimaging and coherent hemodynamics spectroscopy (CHS),” Neuroimage **85**, 202–221, Academic Press (2014) [doi:10.1016/j.neuroimage.2013.03.065].

122. F. Zheng, A. Sassaroli, and S. Fantini, “Phasor representation of oxy-and deoxyhemoglobin concentrations: what is the meaning of out-of-phase oscillations as measured by near-infrared spectroscopy?,” J. Biomed. Opt. **15**(4), 40512 (2010).

123. M. Patterson et al., “Frequency-domain reflectance for the determination of the

scattering and absorption properties of tissue," osapublishing.org.

124. S. J. Matcher et al., "Performance Comparison of Several Published Tissue Near-Infrared Spectroscopy Algorithms," Anal. Biochem. **227**(1), 54–68, Academic Press (1995) [doi:10.1006/ABIO.1995.1252].

125. T. Parks and J. McClellan, "Chebyshev approximation for nonrecursive digital filters with linear phase," Circuit Theory, IEEE Trans. **19**(2), 189–194 (1972) [doi:10.1109/TCT.1972.1083419].

126. B. Boashash, "Estimating and interpreting the instantaneous frequency of a signal. II. Algorithms and applications," Proc. IEEE **80**(4), 540–568 (1992) [doi:10.1109/5.135378].

127. S. Fantini, "Dynamic model for the tissue concentration and oxygen saturation of hemoglobin in relation to blood volume, flow velocity, and oxygen consumption: Implications for," Neuroimage (2014).

128. J. M. Kainerstorfer et al., "Practical Steps for Applying a New Dynamic Model to Near-Infrared Spectroscopy Measurements of Hemodynamic Oscillations and Transient Changes. Implications for Cerebrovascular and Functional Brain Studies.," Acad. Radiol. **21**(2), 185–196 (2014) [doi:10.1016/j.acra.2013.10.012].

129. U. Göbel et al., "Lack of Capillary Recruitment in the Brains of Awake Rats during Hypercapnia," J. Cereb. Blood Flow Metab. **9**(4), 491–499, SAGE PublicationsSage UK: London, England (1989) [doi:10.1038/jcbfm.1989.72].

130. G. Zoccoli et al., "Brain Capillary Perfusion during Sleep," J. Cereb. Blood Flow Metab. **16**(6), 1312–1318, SAGE PublicationsSage UK: London, England (1996) [doi:10.1097/00004647-199611000-00028].

131. W. Kuschinsky and O. B. Paulson, "Capillary circulation in the brain.," pp. 261–286 (1992).

132. K. Masamoto et al., "Apparent diffusion time of oxygen from blood to tissue in rat cerebral cortex: implication for tissue oxygen dynamics during brain functions," J. Appl. Physiol. **103**(4), 1352–1358, American Physiological Society (2007) [doi:10.1152/japplphysiol.01433.2006].

133. H. Ito et al., "Arterial fraction of cerebral blood volume in humans measured by positron emission tomography," Ann. Nucl. Med. **15**(2), 111–116, Springer-Verlag (2001) [doi:10.1007/BF02988600].

134. A. Sassaroli, K. T. Tgavalekos, and S. Fantini, "The meaning of 'coherent' and its quantification in Coherent Hemodynamics Spectroscopy."

135. K. T. Tgavalekos et al., “The dynamic relationship between local cerebral blood volume and systemic mean arterial blood pressure.”

136. J. M. KAINERSTORFER et al., “COHERENT HEMODYNAMICS SPECTROSCOPY BASED ON A PACED BREATHING PARADIGM — REVISITED,” J. Innov. Opt. Health Sci. **7**(1), 1450013 (2014) [doi:10.1142/S1793545814500138].

137. S. Nathanson and L. Nelson, “Interstitial fluid pressure in breast cancer, benign breast conditions, and breast parenchyma,” Ann. Surg. Oncol. **1**(4), 333–338 (1994).

138. C. M. Sehgal et al., “A review of breast ultrasound,” J. Mammary Gland Biol. Neoplasia **11**(2), 113–123 (2006).

139. K. Hiltawsky, M. Krüger, and C. Starke, “Freehand ultrasound elastography of breast lesions: clinical results,” Ultrasound Med. Biol. **27**(11), 1461–1469 (2001).

140. J. Specht and B. Kurland, “Tumor metabolism and blood flow as assessed by positron emission tomography varies by tumor subtype in locally advanced breast cancer,” Clin. Cancer Res. **16**(10), 2803–2810 (2010).

141. R. P. Beaney et al., “Positron emission tomography for in-vivo measurement of regional blood flow, oxygen utilisation, and blood volume in patients with breast carcinoma.,” Lancet **1**(8369), 131–134 (1984).

142. C. Wilson and A. Lammertsma, “Measurements of blood flow and exchanging water space in breast tumors using positron emission tomography: a rapid and noninvasive dynamic method,” Cancer Res. **52**(6), 1592–1597 (1992).

143. C. Wilson and D. Snook, “Quantitative measurement of monoclonal antibody distribution and blood flow using positron emission tomography and 124iodine in patients with breast cancer,” Int. J. Cancer **47**(3), 344–347 (1991).

144. T. Chao et al., “Color Doppler ultrasound in benign and malignant breast tumors,” Breast Cancer Res. Treat. **57**(2), 193–199 (1999).

145. S. Huber et al., “Effects of a microbubble contrast agent on breast tumors: computer-assisted quantitative assessment with color Doppler US--early experience.,” Radiology **208**(2), 485–489 (1998).

146. H. Madjar and H. Prömpeler, “Color Doppler flow criteria of breast lesions,” Ultrasound Med. Biol. **20**(9), 849–858 (1994).

147. T. Durduran et al., “Diffuse optical measurement of blood flow in breast tumors,” Opt. Lett. **30**(21), 2915–2917 (2005).

148. K. Nikolaou and S. Schoenberg, “Quantification of pulmonary blood flow and volume in healthy volunteers by dynamic contrast-enhanced magnetic resonance imaging using a parallel imaging,” Invest. Radiol. **39**(9), 537–545 (2004).

149. D. Busch, R. Choe, and T. Durduran, “Blood flow reduction in breast tissue due to mammographic compression,” Acad. Radiol. **21**(2), 151–161 (2014).

150. A. Athanasiou et al., “Optical mammography: A new technique for visualizing breast lesions in women presenting non palpable BIRADS 4-5 imaging findings: Preliminary results with radiologic-pathologic correlation,” Cancer Imaging **7**(1), 34–40 (2007) [doi:10.1102/1470-7330.2007.0006].

151. A. Y. Sajjadi et al., “Normalization of compression-induced hemodynamics in patients responding to neoadjuvant chemotherapy monitored by dynamic tomographic optical breast imaging (DTOBI),” Biomed. Opt. Express **8**(2), 555–569 (2017).

152. F. Teng et al., “Wearable near-infrared optical probe for continuous monitoring during breast cancer neoadjuvant chemotherapy infusions,” J. Biomed. Opt. **22**(1), 14001, International Society for Optics and Photonics (2017) [doi:10.1117/1.JBO.22.1.014001].

153. N. M. Nasrabadi, “Pattern Recognition and Machine Learning,” J. Electron. Imaging **16**(4), 49901, International Society for Optics and Photonics (2007) [doi:10.1117/1.2819119].

154. S. Wang and R. M. Summers, “Machine learning and radiology.,” Med. Image Anal. **16**(5), 933–951, Elsevier (2012) [doi:10.1016/j.media.2012.02.005].